eXPRESS Polymer Letters Vol.2, No.2 (2008) 77
Available online at www.expresspolymlett.com
DOI: 10.3144/expresspolymlett.2008.10

Editorial corner – a personal view
Smart polymers for biomedical application and environmental protection

*G. Filipcsei**

Materials Structure and Modelling Research Group of the Hungarian Academy of Sciences at the Budapest University of Technology and Economics, H-1521 Budapest, Hungary

In the recent years, the environmental responsive polymers have become of major interest as novel intelligent or smart materials. Many kinds of such gels have been developed and studied in regard to the application to several biomedical and industrial fields, e.g. controlled drug delivery systems, muscle-like soft linear actuators, biomimetic energy transducing devices and separation technique.

The combination of polymers with nano-, or micron sized magnetic particles displays novel and often enhanced properties compared to the traditional materials. Synthesis of stimuli-responsive polymer gel microspheres has been receiving growing attention in the past decade. Polymer microspheres that combine both temperature- and pH-responsive volume phase transitions were developed. Due to their relatively rapid and easy magnetic separation, the magnetic microspheres could be widely used in biomedical and bioengineering, such as enzyme immobilization and immunoassay, cell separation, and clinical diagnosis. In addition owing to their sensitivities to both magnetic field and temperature, thermosensitive polymer magnetic microspheres offer a high potential application in the design of a targeting drug delivery system. The utilization of microspheres is considered as a safe and effective way for tissue-specific release of drugs, with a small amount of magnetic thermoresponsive polymer microspheres, a large amount of drug could be easily administered and transported to the site of choice.

Driving forces for international efforts in the field of wastewater treatment technologies are the recognition of environmental problems in surface waters (oxygen depletion, eutrophication, etc.). The development of environmental sensitive polymers gives a great opportunity to fabricate artificial floc structure according to the technological requirements. The smart polymer microspheres with controllable porosity and properties would provide adequate surface for the bacteria to colonize and grow in a controlled environment of microscopic dimensions. Moreover, the constructed artificial flocs are able to respond to the environmental changes, such as temperature and pH alterations. Simple environmental factors could trigger the changes in the shape and size of the artificial floc (i.e., reacting by swelling or shrinking). Hence the microspheres could regulate the availability of electron acceptors and donors by controlling the diffusion kinetics.

Dr. Genoveva Filipcsei
Member of International Advisory Board

*Corresponding author, e-mail: gfilipcsei@mail.bme.hu

eXPRESS Polymer Letters Vol.2, No.2 (2008) 78–87
Available online at www.expresspolymlett.com
DOI: 10.3144/expresspolymlett.2008.11

Thermal, mechanical and morphological properties of polypropylene/clay/wood flour nanocomposites

S. Y. Lee[1], I. A. Kang[1], G. H. Doh[1], W. J. Kim[1], J. S. Kim[2], H. G. Yoon[2], Q. Wu[3]*

[1]Division of Environmental Material Engineering, Department of Forest Products, Korea Forest Research Institute(KFRI), Hoegi-Ro 57, Dongdaemun-Gu, Seoul, 130-712, Korea
[2]Department of Material Science and Engineering, Korea University, Anam-5Dong, Seongbuk-Gu, Seoul, 136-713, Korea
[3]School of Renewable Natural Resources, Louisiana State University Agricultural Center, Baton Rouge, LA 70803, USA

Received 1 September 2007; accepted in revised form 11 December 2007

Abstract. Nanocomposites with polypropylene/clay/wood flour were prepared by melt compounding. Thermal, mechanical and morphological properties were characterized. The addition of clay, compatibilizer and wood flour considerably improved the thermal stability (i.e., decomposition and melting temperatures) of the hybrids. The tensile modulus and strength of most hybrids were highly increased with the increased loading of clay, MAPP and wood flour, compared to the hybrids without wood flour. The wide angle X-ray diffraction (WAXD) patterns showed the increased d-spacing of clay layers, indicating enhanced compatibility between PP and clay with the addition of maleated polypropylene (MAPP). The transmission electron microscopy (TEM) photomicrographs illustrated the intercalated and partially exfoliated structures of the hybrids with clay, MAPP and wood flour.

Keywords: *nanocomposites, nanoclay, MAPP, PP, wood*

1. Introduction

Composites can be tailored to have the desired properties by incorporating particulate fillers into a polymer matrix to suit different applications. There has been an increasing use of composites in myriad fields from the residential buildings to aeronautics industries [1]. Lignocellulosic fillers such as wood flour, rice husk, jute and sisal have numerous advantages over glass fibers including low cost, biodegradability, easiness of processing and the absence of toxic byproducts. Therefore, they have been widely used as reinforcements for thermoplastic composites [2–5]. The addition of wood flour to neat thermoplastics can greatly stiffen them, but makes them more brittle at the same time [2, 6, 7]. Compatibilizers such as maleated polyethylene (MAPE) and maleated polypropylene (MAPP) played an important role in improving the compatibility and bonding strength between hydrophilic wood flour and hydrophobic thermoplastics [8–10]. Composites with structure and composition at the nanoscale exhibit highly improved mechanical properties and high temperature endurance [11–14]. Among the inorganic layered materials, layered silicates are often used for inclusion in the hybrids due to their ability to intercalate and exfoliate at the nanoscale in the thermoplastic matrix. In particular, the smectite group of clay minerals like montmorillonite (MMT) has been predominantly used, due to its excellent intercalation ability [15–20].

Since thermoplastics such as polyethylene (PE) and polypropylene (PP) are hydrophobic and have poor miscibility with hydrophilic layered silicates, nan-

*Corresponding author, e-mail: nararawood@forest.go.kr

oclay was usually organo-chemically modified with alkylammonium groups to facilitate their interaction with thermoplastics. In addition, the miscibility between nanoclay and PE or PP can be improved by the addition of compatibilizers such as MAPE, MAPP or carboxylated PE [18, 21].

There are two concepts of intercalation and exfoliation, which can define the structures in clay-polymer hybrids. Intercalation, defined as the well-ordered and stacked multilayers that result from intercalated polymer chains within host nanoclay layers. Exfoliation refers to formation of monolayers of clay well-dispersed in a continuous polymer matrix or individually distributed in the polymer matrix. The intercalated and exfoliated hybrids exhibit improved in strength and modulus, compared with neat polymer and conventional composites [11–14,16–18].

The enhanced properties of the composites can be achieved at a low clay loading level (e.g., less than 5.0 wt% addition of clay) [22]. At the 5 wt% clay loading, an approximately 70% increase in modulus and strength was observed for Nylon-clay systems, and both heat distortion temperature and impact strength also increased by more than 100% [23]. However, the dispersion of clay layers in most polymers is not easily accomplished due to face-to-face stacking in agglomerated tactoids and the conversion to a single platelet by complete exfoliation [24, 25].

Although some studies have been conducted on the reinforcement effect of clay in thermoplastics such as PP and PE, limited data is available on the wood flour/clay/plastic hybrids by melt compounding. With the presence of larger-size wood fibers, a synergetic combination of clay and coupling agent is often needed to achieve desired composite properties [21]. The objective of this study was to examine the effect of wood flour, clay, compatibilizer on thermal, mechanical and morphological properties of PP-based composites. Wide angle X-ray diffraction (WAXD), transmission electron microscopy (TEM), thermogravimetric analysis (TGA), differential scanning calorimetry (DSC) and stress-strain behavior were used to evaluate composite properties.

2. Materials and methods

2.1. Materials

Polypropylene (PP 5014, M_w = 180 000 g/mol) was obtained from the Korea Petrochemical Ind. Co., Ulsan, South Korea. Neat PP was in the form of homopolymer pellets with a melt flow index of 3.2 g/10 min and a density of 0.9 g/cm^3. The wood flour (Lignocel C120, particle size of 100–120 mesh per 2.54 cm^2) was supplied from J. Retenmaier & Sohne Co. (Rosenberg, Germany) and manufactured from some European softwood. Maleated polypropylene (MAPP; PH-200, Honam Petrochemical Co., Daejeon, Korea) was used as a compatibilizer. The molecular weight and maleic anhydride grafting level of MAPP were 40 000 g/mol and 5%, respectively. Clay (Montmorillonite, Cloisite® 15A), chemically-modified with a quaternary ammonium salt was purchased from Southern Clay Products, Inc. (Gonzales, Texas, U.S.A.). The clay was a fine powder with a cation exchange capacity of 125 mequiv/100 g. The density and layer distance of clay were 1.6 g/cm^3 and 30.3 Å, respectively. The clay was dried in a vacuum oven at 90°C for 24 h prior to use. The wood flour was dried to 1–2% moisture content using an oven at a temperature of 80°C, and then stored in polyethylene bags until needed.

2.2. Melt compounding

The hybrids with wood flour/clay/PP were prepared with a co-rotating twin-screw extruder (Bautek Co, Uijungbu-city, Korea). The extruder had a screw diameter of 19 mm with an *L*/*D* ratio of 40. A compounding temperature of 190°C was used to prevent the thermal degradation of the wood flour. The screw speed for compounding was in the range of 100–150 rpm, depending on the processing speed through a circular nozzle. The loading levels were 0, 10, 20 and 30 phr (part based on one hundred resin) for wood flour, 0, 1, 3 and 5 phr for clay, and 3, 6 and 10 phr for MAPP. The neat PP (used as control), PP/clay and PP/clay/MAPP hybrids were compounded using a one-step method. A two-step method was used to compound wood flour with PP/clay/MAPP hybrids. In the two step process, PP/clay/MAPP hybrids were compounded and palletized first, and then wood flour was finally compounded with the pellets of PP/clay/MAPP

hybrids. The extrudate in the strand form was air-cooled and pelletized with a pelletizer (Bautek Co., Uijungbu-city, Korea). The hybrid samples were dried at 90°C for 24 h in a vacuum oven to remove the absorbed water before being injection molded at 190°C and then cooled to room temperature.

2.3. TGA and DSC

Thermogravimetric analysis (TGA) was used to investigate thermal decomposition behavior of hybrids with a SDT Q600 Thermogravimetric analyzer (TA Instrument Inc. New Castle, Deleware, U.S.A.). Tests were done under nitrogen at a scan rate of 10°C/min in a programmed temperature range of 30 to 600°C. A sample of 5 to 10 mg was used for each run. The weight change was recorded as a function of temperature. Derivative peak temperature (DT_p) was taken as the maximum temperature acquired from the differentiation of the weight change as a function of time. Differential scanning calorimetry (DSC) experiments were performed with a DSC Q10 system (TA Instrument Inc. New Castle, Deleware, U.S.A.). Each sample was heated and cooled at a scanning rate of 10°C/min under nitrogen atmosphere in order to prevent oxidation. A test sample of 5 to 10 mg was placed in an aluminum capsule and heated from 30 to 200°C for each run. The melting temperature (T_m), enthalpy (ΔH_m), crystallization temperature (T_c), crystalline enthalpy ($-\Delta H_m$) and crystallinity (X_c) were determined after the melt-crystallization process.

2.4. Tensile properties

The tensile strength test for hybrids was performed according to ASTM D638 using an Universal Testing Machine (Zwick Testing Machine Ltd., Leomister, United Kingdom). Test specimens were molded in a size of 3.18 mm (width), 63.66 mm (length) and 3.00 mm (thickness) with a gauge length of 12.5 mm. Tensile strength and modulus were determined the testing machine with an extensometer at a crosshead speed of 10 mm/min. For each treatment level, five replicated specimens were tested.

2.5. Wide angle X-ray diffraction (WAXD)

The intercalation of the clay layers in the hybrids was investigated using a wide angle X-ray diffractometer (WAXD: Model Rigaku ATXG, Rigaku Corp., Tokyo, Japan). Measurements were performed using a nickel-filtered Cu-$K_{\alpha 1}$ radiation source under a voltage of 50 kV and a current of 300 mA. The WAXD scans were obtained in the reflection mode using an incident X-ray wavelength of 31.5 Å at a scan rate of 0.01 degree/min from a 2θ range of 2 to 10°. The interlayer distance of clay in the hybrids was calculated by Bragg's law ($d = n\lambda/2\sin\theta$) from the (001) plane diffraction peak in the WAXD pattern with d as the distance between the atomic layers in a crystal, λ as the wavelength of the incident X-ray beam, and n an integer.

2.6. Transmission electron microscopy (TEM)

The morphology of the hybrids was imaged using a Phillips CM 30 transmission microscope (TEM: FEI Company, Hillsboro, OR, U.S.A.) with an acceleration voltage of 200 kV. Ultra-thin sections of 70–90 nm were cut from injection molded bars perpendicular to the flow direction under cryogenic conditions using a Nova CM-20 ultramicrotome and then placed on 300 mesh grids.

3. Results and discussion

3.1. Thermal properties

3.1.1. TGA results

TGA curves of PP/clay hybrids are shown in Figure 1a. With the addition of clay (1 to 5 phr), a 67°C increase in decomposition temperature compared to neat PP was observed at the 50% weight loss level. The increase in decomposition temperature is attributed to the hindered diffusion (i.e., barrier effect) of volatile decomposition products caused by the dispersed clay particles in the PP matrix [26]. The derivative peak temperature (DT_p) of neat PP was 403.7°C, while the hybrids with clay (1 to 5 phr) showed an increase in the derivative peak temperatures in the range of 17 to 32°C.
Figure 1b shows the TGA thermographs of the hybrids with and without compatibilizer. The addition of compatibilizer (3 phr) to the hybrids increased the decomposition temperature by about 20°C compared to that of hybrids without compatibilizer. This increase was probably due to the physico-chemical adsorption of the volatile prod-

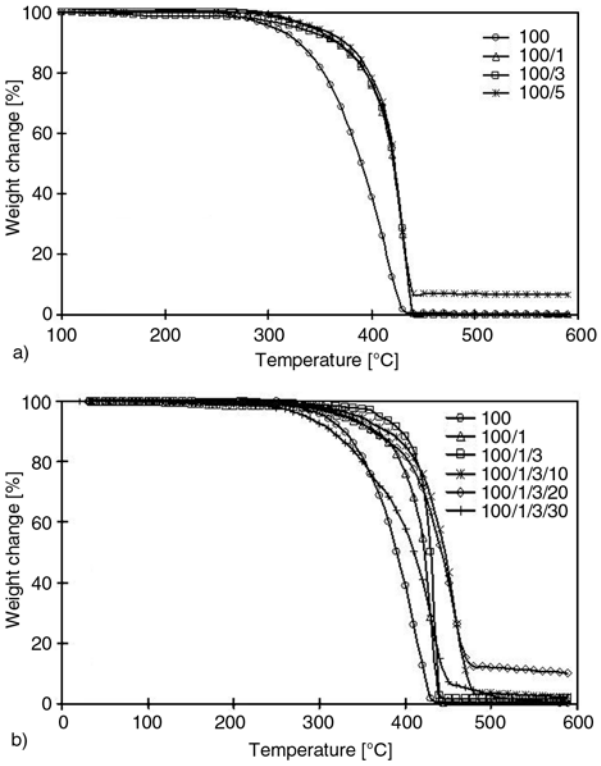

Figure 1. TGA thermographs of (a) PP/clay hybrids, and (b) PP/clay/MAPP/wood flour hybrids

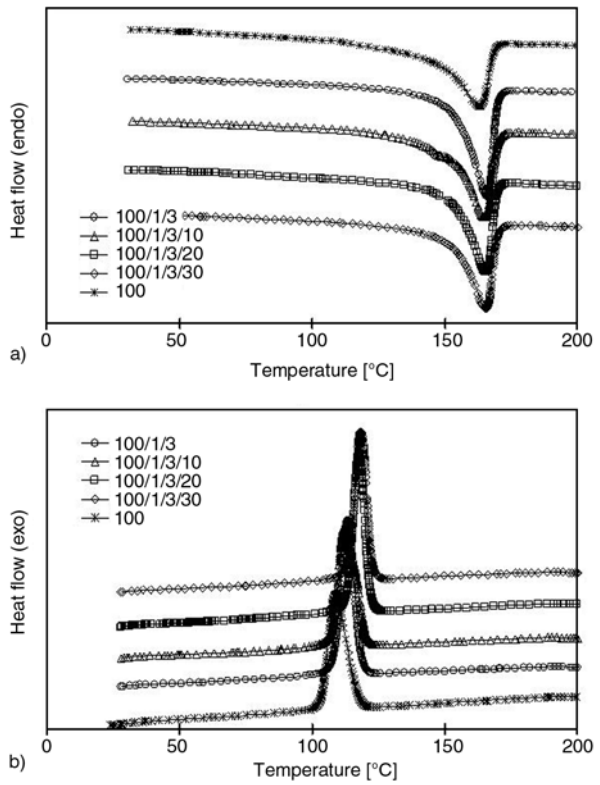

Figure 2. DSC melting results of PP/clay/MAPP/wood flour hybrids. (a) endo heat flow; (b) exo heat flow

ucts on the clay [27], which indicates that the dispersion of clay was improved by the addition of compatibilizer in polymer. The TGA thermographs of the hybrids with wood flour/clay/compatibilizer are shown in Figure 1b. The addition of wood flour (10 and 20 phr) increased the decomposition temperature of clay/compatibilizer hybrids. At the 50% weight loss level, the addition of 10–20 phr increased the decomposition by 40°C, whereas the decomposition temperature decreased slightly at the level of 30 phr wood flour.

3.1.2. DSC results

Table 1 shows the DSC results of PP/clay/wood flour/compatibilizer hybrids used in this study. All hybrid systems had a higher melting temperature (T_m), compared to neat PP. Neat PP had the lowest T_m (163.1°C), while hybrids with clay (5 phr)/MAPP (10 phr)/wood flour (20 phr) had the highest T_m (166.1°C). The increased loading level of clay and MAPP had no significant effect on the T_m of the hybrids. At 1 phr loading of clay, the T_m increased up to 2.1°C with increasing wood flour content (Figure 2a). However, at the 3 and 5 phr clay loading level, the effect of wood flour on the change of T_m was not significant (Table 1).

The enthalpy (ΔH_m) of caloric processes was determined at the heating rate of 10°C/min (Table 1). The ΔH_m of neat PP at transition temperature was 81.8 J/g, but the ΔH_m with different clay (1 to 3 phr) and MAPP (3 to 10 phr) loading levels ranged from 87.5 to 90.4 J/g, indicating an increasing thermal stability. Meanwhile, the addition of wood flour from10 to 30 phr decreased the ΔH_m from 11.8 to 21.0 J/g. This result indicates that wood flour absorbed more heat energy in the melting of the composites as the ΔH_m of wood flour was much lower than that of neat PP [28].

The crystalline peak temperature (T_c) of the hybrids is shown in Table 1. The T_c of PP was 108.7°C, and the addition of clay (1 phr) and MAPP (3 phr) increased the T_c to 111.9°C. Clay and MAPP act as a nucleating agents, which increase the crystallization temperature of PP matrix [20, 29, 30]. The addition of wood flour (10 to 30 phr) to the hybrids increased the T_c to 118.3°C (Figure 2b). The addition of wood flour (30 phr) to PP/clay/MAPP hybrids increased the T_c by up to 6.4–7.9°C com-

Table 1. Thermal and tensile properties of PP/clay/MAPP/wood flour hybrids

Systems	PP/Clay/ MAPP/WF	Thermal properties					Tensile properties	
		T_m [°C]	ΔH_m [J/g]	T_c [°C]	$-\Delta H_m$ [J/g]	X_c [%]	Strength [MPa]	Modulus [MPa]
S1[a]	100/0/0/0	163.1	81.8	108.7	91.0	39.15	32.83 (1.1)[b]	441.7 (21.3)[c]
S2[a]	100/1/3/0	165.9	90.4	111.9	92.0	42.24	36.95 (7.1)	584.7 (27.2)
S3[b]	100/1/3/10	164.8	88.3	113.6	86.8	43.25	37.83 (1.4)	750.3 (45.4)
S4[b]	100/1/3/20	165.4	79.0	117.8	82.6	37.82	38.22 (1.9)	830.1 (51.0)
S5[b]	100/1/3/30	165.2	78.7	118.3	78.2	37.63	40.08 (9.5)	905.6 (54.9)
S6[a]	100/3/6/0	166.2	87.5	110.8	88.2	42.20	38.02 (1.2)	634.9 (34.0)
S7[b]	100/3/6/10	164.7	75.7	117.8	80.9	41.85	36.55 (1.9)	782.0 (19.5)
S8[b]	100/3/6/20	165.5	69.7	117.0	72.4	33.36	37.34 (0.8)	836.4 (36.1)
S9[b]	100/3/6/30	164.6	67.6	118.6	70.0	32.35	36.46 (1.8)	958.4 (26.6)
S10[a]	100/5/10/0	165.5	89.1	111.4	88.8	42.65	41.16 (1.0)	755.5 (34.0)
S11[b]	100/5/10/10	165.4	79.6	115.6	82.8	38.09	47.63 (1.4)	871.3 (31.2)
S12[b]	100/5/10/20	166.1	72.2	116.4	76.8	34.53	38.51 (1.5)	867.4 (46.4)
S13[b]	100/5/10/30	164.9	65.2	118.1	68.8	31.20	39.90 (1.6)	963.8 (36.9)

[a and b] the hybrid systems made using a one-step and two-step compounding method, respectively
[c] mean and standard deviation based on five samples. MAPP = maleated polypropylene, WF = wood flour
T_m = melting point; ΔH_m = enthalpy; T_c = crystalline temperature; $-\Delta H_m$ = crystalline enthalpy; X_c = crystallinity

pared to the hybrids without wood flour. This result indicates that the nucleating effect of clay was further strengthened by the addition of wood flour (Table 1).

The crystalline enthalpy ($-\Delta H_m$) of neat PP was 90.95 J/g. As clay, MAPP and wood flour were added, the $-\Delta H_m$ decreased (Table 1). Since the addition of clay and wood flour interfered with crystallization, it is assumed that the decrease of $-\Delta H_m$ was closely related to the decrease of crystal size itself. However, crystallization occurs because the clay and wood flour played a role of nucleating agent. As shown in Table 1, the crystallinity (X_c) of PP was 39.15%. With the addition of clay and MAPP into neat PP, the X_c increased. As clay loading increased, the X_c of hybrids decreased gradually. The addition of wood flour (10 phr) had no significant effect on the X_c, while the higher loading of wood flour (20–30 phr) greatly reduced the X_c. This indicates that the X_c is generally affected by the dispersion, the loading level, the surface chemistry of fillers and the viscosity of hybrids [31].

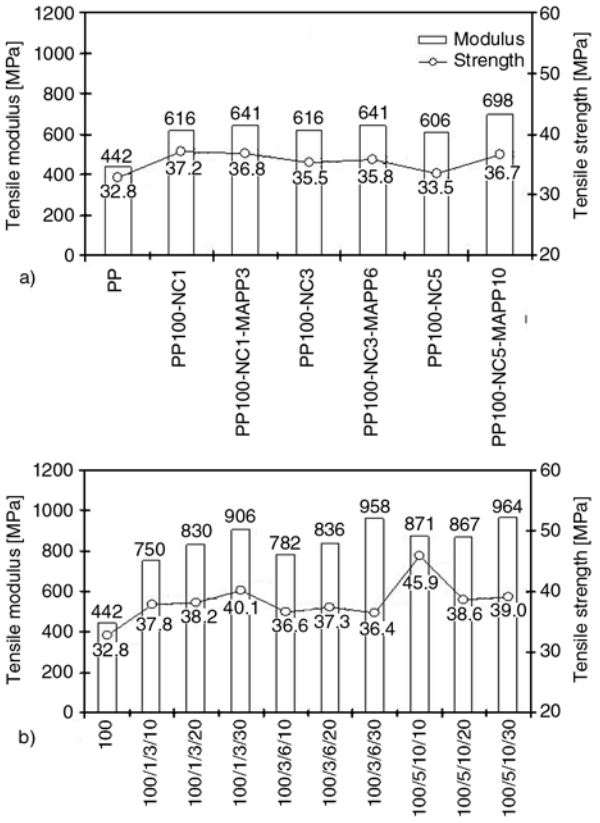

Figure 3. Tensile properties of (a) PP/clay/MAPP hybrids; (b) PP/clay/MAPP/wood flour hybrids

3.2. Mechanical properties

The tensile properties of wood flour/clay hybrids manufactured by the one-step and two-step compounding methods are summarized in Table 1. The tensile strength and modulus of neat PP (S1) were, respectively, 32.8 and 441.7 MPa. Figure 3a shows the effect of clay and compatibilizer contents on the tensile properties of hybrids made by the one-step compounding method. The addition of clay (1, 3 and 5 phr) to PP increased the tensile modulus to 37.1 to 39.4% and increased the tensile strength to

9.1 to 13.4%, compared with those of neat PP. However, the loading level of clay to neat PP showed no effect on the tensile modulus of hybrids. The addition of clay (1, 3 and 5 phr) and MAPP (3, 6 and10 phr) for systems S2, S6 and S10 increased the tensile modulus and strength, compared with the hybrids with only clay. For example, the tensile modulus of the hybrid with 5 phr clay and 10 phr MAPP increased by 15.2% and the tensile strength increased by 9.6%, compared with the hybrids without MAPP. From these results, the high tensile strength is seen to be an intercalation phenomenon of clay layers by MAPP. On the other hand, the increased tensile modulus is attributed to the increased stiffness and brittleness of hybrid composites by the addition of clay.

Figure 3b shows the influence of clay, compatibilizer and wood flour contents on the tensile modulus of the hybrids made by the two-step compounding method. At the loading level of 1% clay, the tensile modulus of hybrids increased as wood flour content increased. As wood flour loading increased to 10, 20 and 30 phr, the tensile modulus increased 21.8, 34.7 and 47.1%, respectively, compared to the system S2. The tensile modulus of most hybrids was highly increased with the increased loading of clay, MAPP and wood flour, compared to the hybrids (S2, S6 and S10). The maximum tensile modulus (964 MPa) was obtained from system S13. This value is 38.1% higher than that of system S10. From these results, it is assumed that the increased modulus is highly related to the increased brittleness and stiffness of the hybrids, due to the addition of wood flour.

The influence of clay, compatibilizer and wood flour contents on the tensile strength of the hybrids is shown in Figure 3b. At the loading of 1 phr clay, the tensile strength of hybrids increased as wood flour content increased. As wood flour loading increased to 10, 20 and 30 phr, the tensile strength increased 2.7, 3.8 and 9.0%, respectively, compared to system S2. On the other hand, the tensile strengths of hybrids at a clay loading level of 3 phr were lower than those at 1 phr clay. At 3 phr clay, the tensile strengths of the clay/MAPP hybrid composites with 10, 20 and 30 phr wood flour were increased by 2.2, 4.2 and 1.7%, respectively, compared to system S6. In other words, the tensile strengths leveled-off as the wood flour loading increased. At 5 phr clay loading, the tensile strength of hybrids decreased as wood flour content increased. The maximum tensile strength (45.9 MPa) was obtained at the wood flour loading of 10 phr (system S11). The tensile strengths of clay/MAPP hybrid composites with 20 and 30 phr wood flour were increased by 5.2 and 6.3%, compared to those of system S10. These results indicate that the increase in tensile strength with the increase of wood flour at low levels of clay is related to the improved bonding strength between wood flour and neat PP compared to the intermolecular bonding of neat PP [2, 8]. It is assumed that the decrease in tensile strength with increasing wood flour at higher clay levels is highly related to the increased viscosity of the hybrids rather than the boding strength.

3.3. Morphology from WAXD and TEM

3.3.1. WAXD results

The WAXD of clay reinforced PP composites can quantify the periodic intercalated structures of inorganic crystalline layers in the 2θ range of 2 to 10° Therefore, the clay product with a d-spacing of 30.3 Å (2θ = 2.91), was compared with hybrid composites. Figure 4a and Table 2 illustrate the

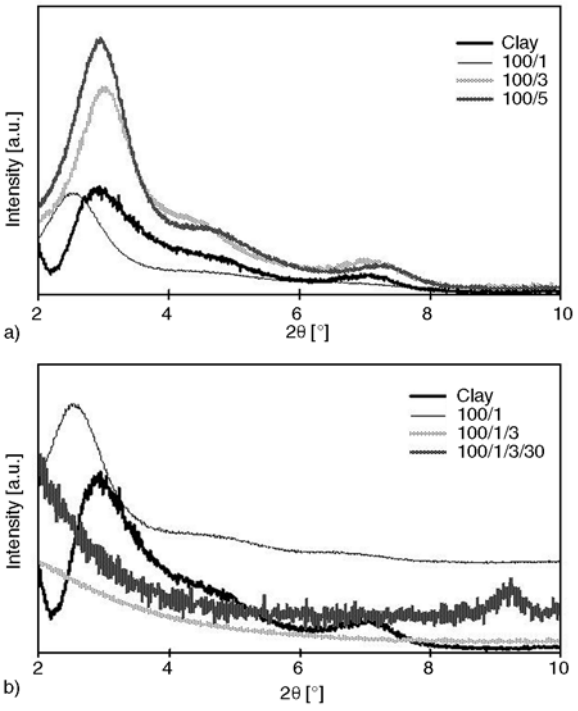

Figure 4. WAXD patterns of selected composite systems. (a) clay and PP/clay hybrids; (b) clay, PP/clay, PP/clay/MAPP, and PP/clay/MAPP/wood flour hybrids

Table 2. Interlayer distance of clay by wide angle X-ray diffraction

Systems	PP/clay	Value at 2θ [°]	d_{001} spacing [Å]
S1[a]	100/0	2.91	30.3
S2[a]	100/1	2.59	34.1
S3[a]	100/2	2.95	29.9
S4[a]	100/3	3.10	28.5
S5[a]	100/4	3.05	29.0
S6[a]	100/5	3.00	29.4

[a]hybrid systems made using a one-step compounding method

comparison of WAXD patterns of hybrid composites with different levels of clay. The (001) peak of the hybrid with 1 phr clay was shifted to a lower value (2θ = 2.95, d-spacing = 34.1 Å), which indicates an increase of d-spacing for clay layers. On the other hand, the (001) peaks of hybrids with 2 to 5 phr clay were shifted to a higher value (minimum 2θ = 3.10, d-spacing = 28.5 Å), which indicates a decrease in d-spacing for clay layers. This decrease of the d-spacing of clay layers is presumably due to the low compatibility at interfaces between neat PP and clay.

Through the enhancement of the compatibility between neat PP and clay, the polymer chains could be well diffused into the clay layers and the d-spacing of clay layers might be increased (Figure 4b). Therefore, the peaks disappeared when 3 phr MAPP was incorporated, representing the intercalation of PP into the clay layers or the partial exfoliation of the clay layers. The (001) peaks of WAXD of the composites with the MAPP showed a broad and weak peak intensity compared to the (001) peaks of WAXD without MAPP. The (001) peaks of WAXD with wood flour/MAPP/clay hybrid prepared by the two-step compounding method are shown in Figure 4b. The addition of wood flour with clay and MAPP gave much wider peaks, indicating the improved compatibility of wood flour and PP matrix by adding MAPP and the enhancement of intercalation from the better shear action by adding wood flour during the compounding process.

3.3.2. TEM results

The TEM photomicrographs of the hybrids with clay, MAPP and wood flour prepared by the one-step and two-step compounding are shown in Figures 5a–5h. The dark lines in Figures 5a and 5b correspond to the intersection of clay layers of 3.15 nm thick clay layers, showing a large number of multi-layered stacks of clay platelets, and no clay platelets intercalated with polymer. The TEM photomicrographs in Figures 5c and 5d contain a large number of multilayered clay platelets intercalated with PP, corroborating the WAXD results [15]. This result is closely related to the enhancement of clay dispersion by MAPP and the intercalation of clay platelets with polymer. Moreover, the TEM photomicrographs in Figures 5e–5h reveal well-intercalated and partially exfoliated structures containing dispersed layers of clay, showing a larger number of platelets per unit area on average. With the addition of wood flour, the intercalated and partially exfoliated structures were clearly detected.

4. Conclusions

The effects of clay, wood flour and compatibilizer on the melting and crystallization behavior, mechanical properties and morphology of PP/clay/wood flour nanocomposites were studied. The addition of clay (1 to 5 phr), compatibilizer (5 to 10 phr) and wood flour (10 to 20 phr) increased the decomposition temperature and melting temperature of the hybrids. The crystalline peak temperature of the hybrids increased with the use of clay and wood flour compared to that of neat PP. The crystalline enthalpy largely decreased due to the increase of viscosity and the decrease of dispersion in the polymer as clay, compatibilizer and wood flour were added. The addition of clay to neat PP increased the tensile modulus and strength. The addition of clay and MAPP to neat PP increased the tensile modulus and strength, compared with the hybrids with only clay. The tensile modulus and strength of most hybrids were highly increased with the increased loading of clay, MAPP and wood flour, compared to the hybrids without wood flour. The increased tensile modulus is attributed to the increased stiffness and brittleness of hybrid composites by the addition of clay and wood flour. On the other hand, the high tensile strength is related to an intercalation phenomenon of clay layers and the increased bonding strength between wood flour and neat PP by MAPP. The WAXD pattern of the hybrids showed increased d-spacing of clay layers, indicating improved compatibility of

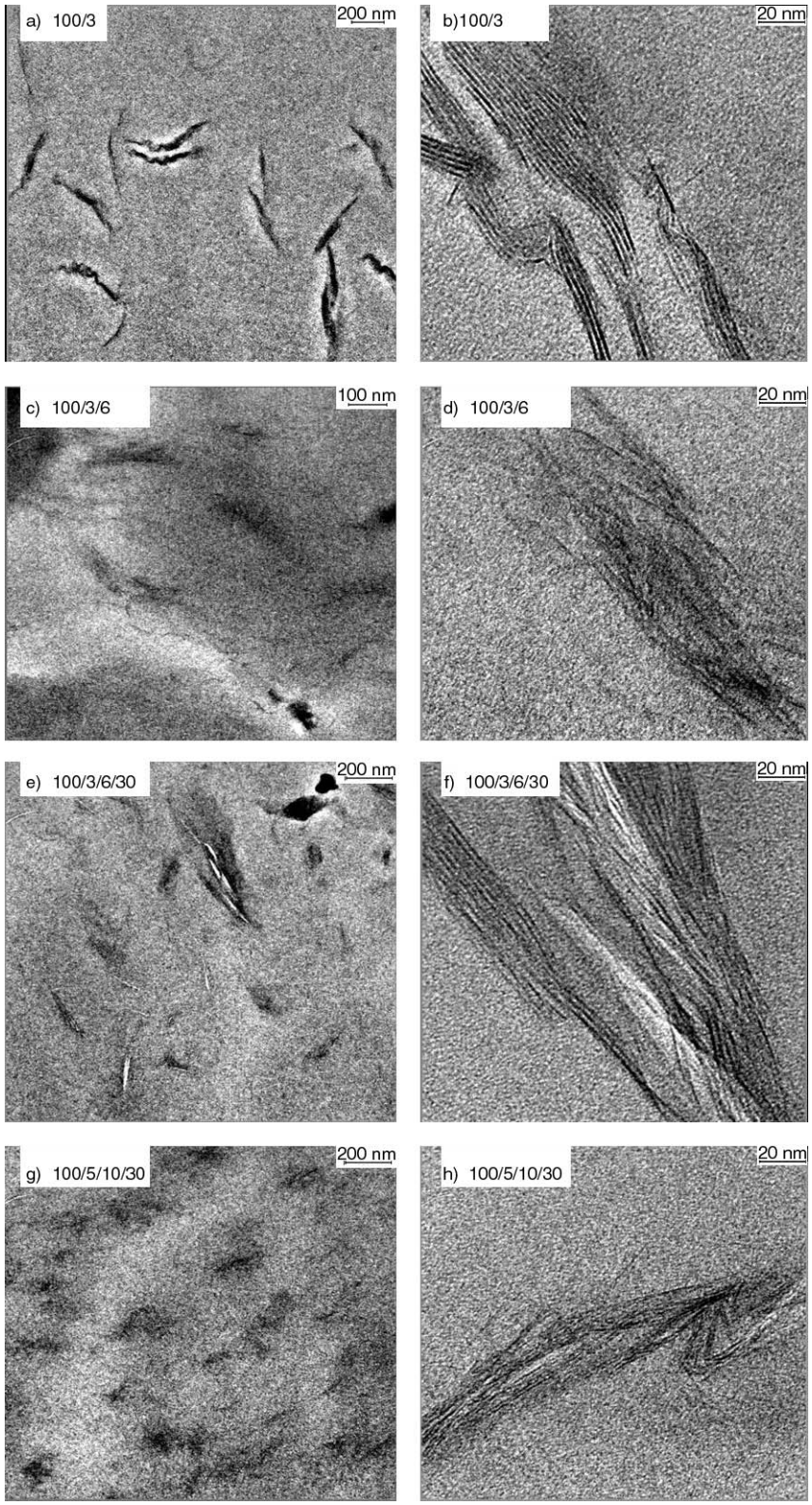

Figure 5. TEM images of PP/clay/MAPP/wood flour hybrids. a) and b) PP/clay: 100/3; c) and d) PP/clay/MAPP: 100/3/6; e) and f) PP/clay/MAPP/WF: 100/3/6/30; and g) and h) PP/clay/MAPP/WF: 100/5/10/30. Scale-bar of (a), (c), (e), and (g) was 100 nm, and scale-bar of (b), (d), (f), (h) was 20 nm

neat PP and clay by the addition of MAPP and the intercalation and partial exfoliation of clay layers. The TEM photomicrographs further illustrated the intercalated and partially exfoliated structures formed by the addition of clay, MAPP and wood flour. From this study, the desired composite properties can be tailored by a synergetic combination

of clay and coupling agent with the presence of large-size wood flour.

References

[1] Bledzki A. K., Gassan J.: Composites reinforced with cellulose fibres. Progress in Polymer Science, **24**, 221–274 (1999).

[2] Lee S-Y., Yang H-S., Kim H-J., Jeong C-S., Lim B-S., Lee J-N.: Creep behavior and manufacturing parameters of wood flour filled polypropulene composites. Composite Structures, **65**, 459–469 (2004).

[3] Kim H-S., Yang H-S., Kim H-J., Park H-J.: Thermogravimetric analysis of rice husk flour filled thermoplastic polymer composites. Journal of Thermal Analysis and Calorimetry, **76**, 395–404 (2004).

[4] Svelto C., Taccheo S., Bava E., Laporta P., Joseph P. V., Joseph K., Thomas S.: Effect of processing variables on the mechanical properties of sisal-fiber-reinforced polypropylene composites. Composite Science and Technology, **59**, 1625–1640 (1999).

[5] Rana A. K., Mandal A., Mitra B. C., Jacobson R., Rowell R., Banerjee A. N.: Short jute-reinforced polypropylene composites: Effect of compatibilizer. Journal of Applied Polymer Science, **69**, 329–338 (1998).

[6] Premalal B. H. G., Ismail H., Baharin A.: A comparison of the mechanical properties of rice husk powder filled polypropylene composites with talc filled polypropylene composites. Polymer Testing, **21**, 833–839 (2002).

[7] Yang H-S., Kim H-J., Son J., Park H-J. Lee B-J., Hwang T-S.: Rice husk flour filled polypropylene composites: mechanical and morphological study. Composite Structures, **63**, 305–312 (2004).

[8] Lu J. Z., Wu Q., McNabb Jr. H. S.: Chemical coupling in wood fiber and polymer composites: A review of coupling agents and treatments. Wood Fiber Science, **32**, 88–104 (2000).

[9] Woodhams R. T., Thomas G., Rodgers D. K.: Wood fibers as reinforcing fillers for polyolefins. Polymer Engineering and Science, **24**, 1166–1171 (1984).

[10] Clemons C.: Wood-plastic composites in the United States: The interfacing of two industries. Forest Products Journal, **52**, 10–18 (2002).

[11] Oksman K., Sain M.: Cellulose nanocomposites: processing, characterization and properties. ACS Symposium Series, Washington D.C. (2005).

[12] Pinnavaia T. J., Beall G. W.: Polymer-clay nanocomposites. John Wiley and Sons, West Sussex (2000).

[13] Ajayan P. M., Schadler L. S., Braun P. V.: Nanocomposite Science and Technology. Wiley-VCH, Weinheim (2006).

[14] Ktawczak P.: Compounding and processing of polymer nanocomposites: from scientific challenges to industrial stakes. Express Polymer Letters, **1**, 188 (2007).

[15] Giannelis E. P., Krishnaoorti R., Manias E.: Polymer-silicate nanocomposites: model system for confined polymers and polymer brushes. Advances in Polymer Science, **138**, 107–147 (1999).

[16] Kojima Y., Usuki A., Kawasumi M., Okada A., Fukushima Y., Kurauchi T., Kamigaito O.: Mechanical properties if nylon 6-clay hybrid. Journal of Material Research, **8**, 1185–1189 (1993).

[17] Liu T. X., Liu Z. H., Ma K. X., Shen L., Zeng K. Y., He C. B.: Morphology, thermal and mechanical behavior of polyamide 6/layered-silicate nanocomposites. Composite Science and Technology, **63**, 331–337 (2003).

[18] Lee S. U., Oh I. H., Lee J. H., Choi K. Y., Lee S. G.: Preparation and characterization of polyethylene/montmorillonite nanocomposites. Polymer (Korea), **3**, 271–276 (2005).

[19] Lee S. G., Won J. C., Lee J. H., Choi K-Y.: Flame retardancy of polyproplynene-Montmorillonite nanocomposites. Polymer (Korea), **29**, 248–252 (2005).

[20] Chow W. S.: Water absorption of epoxy/glass fiber/organo-montmorillonite nanocomposites. Express Polymer Letters, **1**, 104–108 (2007).

[21] Lei Y., Wu Q., Clemons C. M.: Preparation and properties of recycled HDPE/clay Hybrids. Journal of Applied Polymer Science, **103**, 3056–3063 (2006).

[22] Fornes, T. D., Yoon P. J., Hunter D. L., Keskkula H., Paul D. R.: Effect of organoclay structure on nylon 6 nanocomposites morphology and properties. Polymer, **43**, 5915–5933 (2002).

[23] Wu Q., Liu X., Berglund L. A.: FT-IR spectroscopic study of hydrogen bonding in PA6/clay nanocomposites. Polymer, **43**, 2445–2449 (2002).

[24] Yoon P. J., Fornes T. D., Paul D. R.: Thermal expansion behavior of nylon 6 nanocomposites. Polymer, **43**, 6727–6741 (2002).

[25] Carrado K. A., Xu L., Seifert S., Csencsits R., Bloomquist C. A.: Polymer-clay nanocomposites derived from polymer-silicate gels. in 'Polymer-Clay Nanocomposites' (Eds.: by Pinnavaia T. J. and Beall G. W.) John Wiley and Sons, Chichester 47–63 (2001).

[26] Qin H., Zhang S., Zhao C., Feng M., Yang M., Shu Z., Yang S.: Thermal stability and flammability of polypropylene/montmorillonite composites. Polymer Degradation and Stability, **85**, 807–813 (2004).

[27] Zanetti M., Camino G., Peichert P., Mülhaupt R.: Thermal behavior of poly(propylene) layered silicate nanocomposites. Macromolecular Rapid Communcations, **22**, 176–180 (2001).

[28] Lee S. Y., Doh G. H., Kang I. A.: Thermal behavior of hwangto and wood flour reinforced high density polyethylene (HDPE) composites. Mokchae Konghak, **34**, 59–66 (2006).

[29] Liang G., Xu J., Bao S., Xu W.: Polyethylene/maleic anhydride grafted polyethylene/organic-montmorillonite nanocomposites. Preparation, microstructure, and mechanical properties. Journal of Applied Polymer Science, **91**, 3974–3980 (2004).

[30] Gopakumar T. G., Lee J. A., Kontopoulou M., Parent J. S.: Influence of clay exfoliation on the physical properties of montmorillonite/polyethylene composites. Polymer, **43**, 5483–5491 (2002).

[31] Wang K. H., Choi M. H., Koo C. M., Xu M., Chung I. J., Jang M. C., Choi S. W., Song H. H.: Morphology and physical properties of polyethylene/silicate nanocomposite prepared by intercalation. Journal of Polymer Science, Part B: Polymer Physics, **40**, 1454–1463 (2002).

eXPRESS Polymer Letters Vol.2, No.2 (2008) 88–92
Available online at www.expresspolymlett.com
DOI: 10.3144/expresspolymlett.2008.12

Development of dental resin luting agents based on Bis-EMA4: bond strength evaluation

R. R. Moraes[1*], *L. S. Gonçalves*[1], *F. A. Ogliari*[2], *E. Piva*[2], *M. A. Sinhoreti*[1], *L. Correr-Sobrinho*[1]

[1]Department of Restorative Dentistry, Dental Materials Division Piracicaba Dental School, State University of Campinas Av. Limeira, 901 – 13414-903 – Piracicaba, SP, Brazil
[2]Department of Restorative Dentistry School of Dentistry, Federal University of Pelotas R. Gonçalves Chaves, 457 – 96015-560 – Pelotas, RS, Brazil

Received 25 September 2007; accepted in revised form 11 December 2007

Abstract. The aim of this study was to investigate the influence of incorporating Bis-EMA4 monomer into experimental Bis-GMA/TEGDMA-based resin luting agents on the bond strength to dentin. Seven mixtures were prepared with the following ratios (wt%) of Bis-GMA/TEGDMA/Bis-EMA4: 50/50/0, 50/30/20, 50/10/40, 50/0/50, 30/10/60, 10/10/80 and 0/0/100. Camphorquinone (0.4 wt%), N,N-dimethyl-p-toluidine (0.8 wt%) and hydroquinone (0.2 wt%) were dissolved in each mixture, which was loaded with silanated strontium glass fillers to a constant content of 60 wt%. Bond strength was evaluated by microshear testing (n = 10) on bovine dentin. Data were submitted to Analysis of Variance ($p < 0.05$). Modes of failure were classified under magnification (200×). Bond strength means (MPa), respective to each agent, were: 19.4, 19.8, 20.0, 19.1, 16.8, 18.7 and 17.8. No significant differences were detected among groups. Mixed failures were generally predominant for all materials. In conclusion, the addition of Bis-EMA4 presented no significant influence on the bond strength of the experimental resin luting agents to dentin.

Keywords: *adhesion, dental materials, dentin, resin luting agents*

1. Introduction

Over the past decade, the synthesis and characterization of inorganic-organic hybrid materials have received considerable attention [1]. In dentistry, the use of hybrid materials such as resin composites and luting agents is increasingly popular, mainly due to their aesthetics, low solubility and ability to bond to tooth structure. Formulations are generally a mixture of mono and dimethacrylate monomers loaded with silanated glass filler particles. Bisphenol A glycol dimethacrylate (Bis-GMA) is the most common monomer in the resin phase, presenting high molecular weight and low polymerization shrinkage [2]. Due to its high viscosity, the Bis-GMA is usually diluted with triethylene glycol dimethacrylate (TEGDMA) [2]. However, TEGDMA has been linked to increased water sorption and polymerization shrinkage [2–4].

In order to overcome the drawbacks of the dilution process using TEGDMA, ethoxylated bisphenol A glycol dimethacrylate (Bis-EMA) has been investigated as an alternative monomer [5–6]. This is structurally analogous to Bis-GMA, but without the two pendant hydroxyl groups responsible for the high viscosity and water affinity of Bis-GMA. Therefore, the addition of Bis-EMA could minimize or eliminate the use of TEGDMA as a diluent comonomer, while potentially reducing the polymerization shrinkage and stress due to the higher molecular weight and lower mobility of Bis-EMA molecule compared with TEGDMA.

*Corresponding author, e-mail: moraesrr@fop.unicamp.br

Previous studies reported that the monomers composing the organic phase might affect the properties of a composite, such as its viscosity, degree of conversion and curing shrinkage [2–4, 6, 7]. In addition, as distinct monomers may present different wettability, shrinkage stress and double bond conversion values, their bond ability to tooth structures, mediated by an adhesive system, might be different. However, the effect of Bis-EMA addition on the bond strength of resin composites to dentin is not well-established.

Therefore, the aim of this study was to investigate the bond strength to dentin of experimental luting agents in which Bis-EMA4 replaced Bis-GMA and/or TEGDMA. The null hypothesis was that no significant difference in bond strength would be observed, irrespective of the monomers composing the luting materials.

2. Experimental

Seven experimental resin luting agents based on Bis-GMA, TEGDMA and/or Bis-EMA4 (Esstech Inc., Essington, PA, USA), were tested. The chemical structure of each monomer is shown in Figure 1. Bis-EMA4 is analogous to Bis-GMA; however, the former has four ethylene oxide units substituting the two hydroxyl groups between the aromatic backbone and the insaturates. The formulation of all luting agents is shown in Figure 2.

Starting from a 50:50 wt:wt ratio blend of Bis-GMA and TEGDMA, different mixtures were produced in which Bis-GMA and/or TEGDMA were substituted by Bis-EMA4.

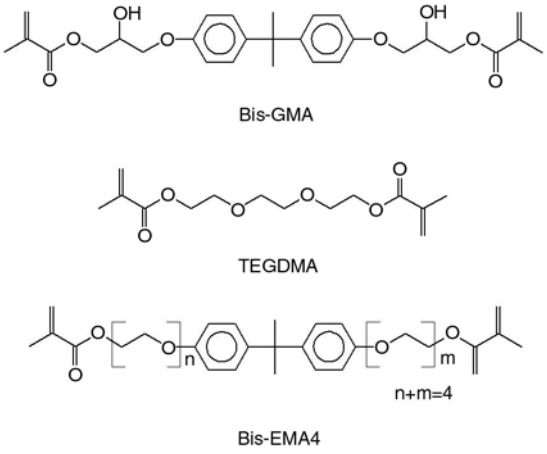

Figure 1. Molecular structure of the monomers used in the study

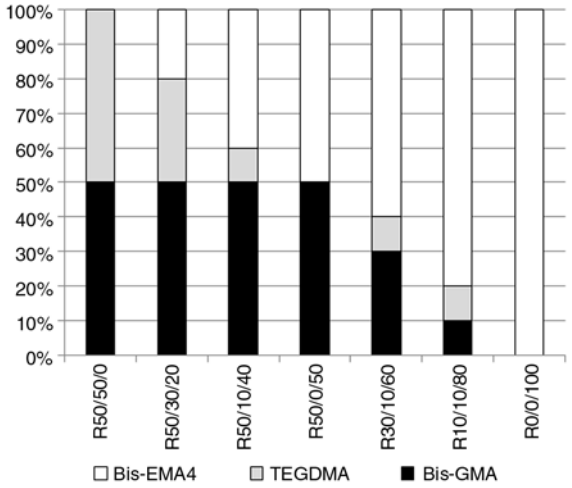

Figure 2. Formulation of the materials tested in the study

In order to make light-curing materials, 0.4 wt% of camphorquinone (Esstech Inc.) and 0.8 wt% of N,N-dimethyl-p-toluidine (Aldrich Chemical Co., Milwaukee, WI, USA) were dissolved in each mixture as photo-initiators. The proprietary monomers used in the study present an average of 0.03% of inhibitor. However, as a photo-sensitive curing initiation system was added to the mixtures, 0.2 wt% of hydroquinone (Aldrich) was used as a radical scavenger to increase the shelf-life of the materials. All chemicals were used as received, without further purification.

Materials were loaded with silanated strontium glass fillers (Esstech Inc.), 0.7 and 2 μm in size, to a constant content of 60 wt% (1:1 of each size). Each material was labeled as R(G/T/E), where G = Bis-GMA wt%, T = TEGDMA wt% and E = Bis-EMA4 wt%. The percentage values are relative to the monomer fraction in the organic phase.

For bond strength evaluation, bovine incisors were obtained, cleaned and stored in 0.5% chloramine-T solution for seven days. The teeth were then embedded in epoxy resin and their buccal faces were wet-ground with 180-, 220-, 400- and 600-grit SiC abrasive papers, in order to create a smooth, flat surface in medium dentin. The adhesive system Single Bond 2 (3M ESPE, St. Paul, MN, USA) was applied on dentin, according to the manufacturer's instructions. Absorbent paper was used to remove the excess dentin moisture.

In order to obtain specimens for the microshear bond strength test, the experimental set-up shown in Figure 3 was carried out [8]. Customized 0.5 mm-thick elastomer molds, each with three

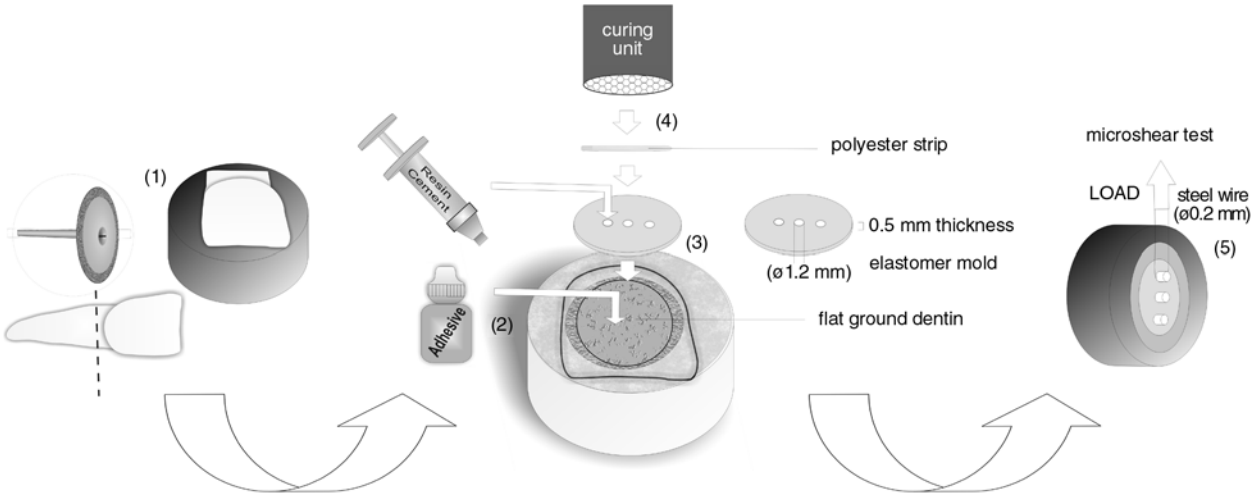

Figure 3. Experimental set-up for the bond strength evaluation: (1) bovine teeth embedded in epoxy resin; (2) bonding agent applied to ground dentin; (3) elastomer mold with cylinder-shaped orifices positioned onto the surface and filled with luting agent; (4) polyester strip placed between the mold and the light guide tip; (5) microshear bond strength test carried out

cylinder-shaped orifices (1.2 mm in diameter), were placed in the teeth surfaces, allowing delimitation of the bonding area. After photo-activation of the bonding agent (quartz-tungsten-halogen light-curing unit XL2500; 3M ESPE), the orifices were filled with each experimental luting agent, and a transparent polyester strip was placed over the filled orifices. Prior to the curing procedures, a constant and uniform 250 g cementation load was applied for 2 min, using a custom-made device. The output irradiance of the curing unit was 700 mW/cm^2, between 410 and 510 nm, confirmed with a digital power meter (Ophir Optronics, Danvers, MA, USA) and a computer-controlled spectrometer (USB 2000; Ocean Optics, Dunedin, FL, USA), respectively.

After storing the samples in distilled water at 37°C for 24 h, all resin cylinders were checked under magnification (40×): those presenting flaws, irregularities or bonding defects were eliminated. For the microshear test, a thin steel wire (0.2 mm in diameter) was looped around each cylinder and aligned with the bonding interface. The test was conducted in a universal testing machine (model 4411; Instron Inc., Canton, MA, USA), at a cross-head speed of 0.5 mm/min until failure. Bond strength values were calculated in MPa. For each group, 10 specimens were tested, and the average value of the three resin cylinders was recorded as the bond strength for each sample. Bond strength data were submitted to one-way Analysis of Variance ($p = 0.05$).

The fractured specimens were examined under optical microscopy at a 200× magnification. Modes of failure were classified as follows: adhesive failure (Mode 1), cohesive failure within dentin (Mode 2), or mixed failure involving bonding agent, luting material and dentin (Mode 3). Additionally, representative fractured specimens were coated with gold and examined under scanning electron microscopy (SEM – JSM5600LV; Jeol Inc., Peabody, MA, USA).

3. Results

Results for the microshear test are shown in Table 1. The Analysis of Variance showed that,

Table 1. Means (standard deviations) for bond strength to dentin, and percentage of scores for the failure analysis

Material	Bond strength [MPa]	Failure modes*[%]		
		Mode 1	Mode 2	Mode 3
R50/50/0	19.4 (4.3)	14.3	33.3	52.4
R50/30/20	19.8 (5.6)	27.8	18.7	53.5
R50/10/40	20.0 (6.7)	12.5	12.5	75.0
R50/0/50	19.1 (4.3)	64.8	0	35.2
R30/10/60	16.8 (4.2)	25.9	18.5	55.6
R10/10/80	18.7 (5.3)	30.4	13.0	56.6
R0/0/100	17.8 (3.6)	32.0	12.0	56.0

*Mode 1: adhesive failure; Mode 2: cohesive failure within dentin, Mode 3: mixed failure involving bonding agent, luting material and dentin

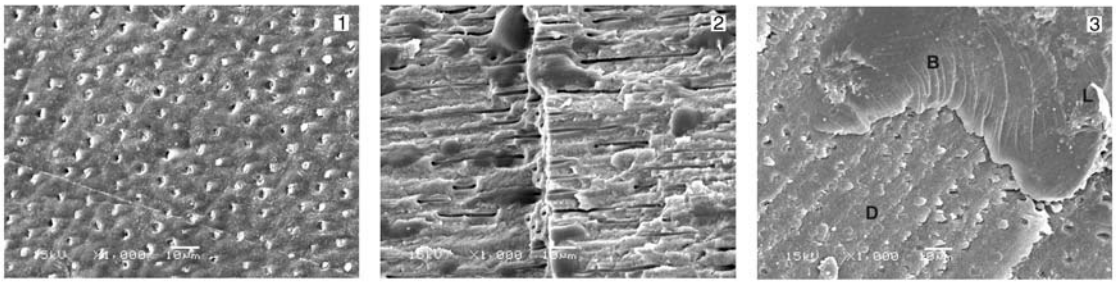

Figure 4. Representative SEM images of fractured specimens. (1) adhesive failure, which is characterized by the presence of opened and partially opened dentinal tubules and scratch lines formed during grounding procedures; (2) cohesive failure within dentin; (3) mixed failure involving bonding agent (B), luting material (L) and dentin (D)

irrespective of the monomers composing the organic phase of the luting agents, no significant differences in bond strength were detected (p = 0.778). Table 1 also shows the results for the failure analysis. SEM pictures of fractured specimens are shown in Figure 4. A predominance of mixed failures (Mode 3) was generally detected for all materials, except for R50/0/50, for which a predominance of adhesive failures (Mode 1) was detected. Cohesive failures within the luting agent were not observed, irrespective of the material tested.

4. Discussion

The current outcomes showed similar microshear bond strengths to dentin for the different resin luting agents. Therefore, the null hypothesis was accepted. The distinct monomers present different molecular weight, chain flexibility and curing reactivity [2, 5–7], implying that several properties of a composite might be affected by its components [9]. Although the bonding ability to tooth substrate could also be influenced by the composition of the agents [10], the current outcomes showed no significant effect.

For a resin-based composite, the main properties that might affect its bonding ability to tooth tissues are the degree of conversion, wetability and shrinkage stress. In fact, Xu *et al*. [11] reported that the higher the double bond conversion of a composite, the higher its bond strength to dentin. This might result from the better mechanical properties disclosed by more properly cured materials [9], which could enhance the bonding to dentin. Previous tests with the same experimental luting agents tested here showed differences in the degree of conversion among materials [12]. Furthermore, during the mixing procedures for preparing the luting agents, replacing TEGDMA with Bis-EMA4 increased the apparent viscosity of the agents. Although both of these monomers are less viscous than Bis-GMA, this observation is related to the fact that Bis-EMA4 presents a higher molecular weight and structure stiffness than TEGDMA. Materials with high viscosity might present poor wettability with the substrate surface, potentially interfering with the bonding outcomes.

Moreover, differences in the resin component might interfere with the shrinkage stress and the interaction of force vectors created during constrained polymerization, which may produce effects detrimental to the material being bonded, as a competition between contraction and bond is created [13]. Nonetheless, despite the above mentioned characteristics, no significant differences in microshear bond strength were detected among the experimental materials, suggesting that the bonding ability to dentin is less influenced by the components of the resin phase than other properties of the polymer.

Although it is known that polymerization shrinkage is related to double bond conversion, it has been demonstrated that the shrinkage stress development of a resin material depends not only upon its mass and properties, but also on the configuration-factor (C-factor) [14, 15]. The C-factor refers to a ratio of bonded to unbonded surface area in a cavity preparation. For example, a box-like cavity has five bonded surfaces and one unbonded surface, giving it a C-factor of 5, assuming all walls have the same surface area. During the polymerization stage, the maturing composite-dentin bond strength competes with the shrinkage stress of the setting material [14]. In situations where shrinkage stress exceeds bonding strength, debonding of restorations might

occur, posing a risk to post-operative sensitivity and secondary caries.

However, it is important to highlight that the experimental design of traditional bond strength tests allow the composite to be cured from a free surface, with low C-factor, and having the polymerization shrinkage restricted to one direction could minimize the development of setting stresses [14]. Therefore, further investigations on the current materials are required. In clinical practice, this situation could be relevant during the cementation of an intra-radicular post, for instance, as a high C-factor condition would be established.

Results for the failure analysis were in general similar for all materials. However, more adhesive failures were verified for R50/0/50, with no cohesive failures within dentin. This result is probably explained by the high viscosity of this luting material, which might have interfered with its wettability to the bonding system surface, resulting in increased adhesive failures. In summary, the current outcomes indicate that the monomers composing the resin phase of resin luting agents seem to present no significant influence on their bonding ability to bovine dentin. Nonetheless, other properties need to be evaluated in order to known the characteristics of polymers derived from different mixtures of monomers.

5. Conclusions

The addition of Bis-EMA4 into experimental luting agents based on Bis-GMA/TEGDMA presented no significant influence on the bond strength to dentin. From this standpoint, Bis-EMA4 demonstrated to be a useful alternative in the development of resin luting agents.

Acknowledgements

The first author is grateful to CNPq/Brazil for a scholarship. Authors thank Esstech Inc. for the donation of the reagents.

References

[1] Da Z. L., Zhang Q. Q., Wu D. M., Yang D. Y., Qiu F. X.: Synthesis, characterization and thermal properties of inorganic-organic hybrid. Express Polymer Letters, **1**, 698–703 (2007).

[2] Anseth K. S., Goodner M. D., Reill M. A., Kannurpatti A. R., Newman S. M., Bowman C. N.: The influence of comonomer composition on dimethacrylate resin properties for dental composites. Journal of Dental Research, **75**, 1607–1612 (1996).

[3] Dermann K., Rupp N. W., Brauer G. M.: Effect of hydrophilic diluents on the properties of cured composites. Journal of Dental Research, **61**, 1250–1254 (1982).

[4] Dulik D., Bernier R., Brauer G. M.: Effect of diluent monomer on the physical-properties of Bis-GMA-based composites. Journal of Dental Research, **60**, 983–989 (1981).

[5] Sideridou I., Achilias D. S., Spyroudi C., Karabela M.: Water sorption characteristics of light-cured dental resins and composites based on Bis-EMA/PCDMA. Biomaterials, **25**, 367–376 (2004).

[6] Sideridou I., Tserki V., Papanastasiou G.: Effect of chemical structure on degree of conversion in light-cured dimethacrylate-based dental resins. Biomaterials, **23**, 1819–1829 (2002).

[7] Stansbury J. W., Dickens S. H.: Network formation and compositional drift during photo-initiated copolymerization of dimethacrylate monomers. Polymer, **42**, 6363–6369 (2001).

[8] Moraes R. R., Correr-Sobrinho L., Sinhoreti M. A., Puppin-Rontani R. M., Ogliari F. A., Piva E.: Light-activation of resin cement through ceramic: relationship between irradiance intensity and bond strength to dentin. Journal of Biomedical Materials Research, Part B: Applied Biomaterials, in press, doi: 10.1002/jbm.b.30928 (2007).

[9] Ferracane J. L., Greener E. H.: The effect of resin formulation on the degree of conversion and mechanical properties of dental restorative resins. Journal of Biomedical Materials Research, **20**, 121–131 (1986).

[10] Thomsen K. B., Peutzfeldt A.: Resin composites: Strength of the bond to dentin versus mechanical properties. Clinical Oral Investigations, **11**, 45–49 (2007).

[11] Xu X., Sandras D. A., Burgess J. O.: Shear bond strength with increasing light-guide distance from dentin. Journal of Esthetic and Restorative Dentistry, **18**, 19–27 (2006).

[12] Moraes R. R., Ogliari F. A., Piva E., Petzhold C. L., Sinhoreti M. A. C., Correr-Sobrinho L.: Influence of Bis-EMA4 on properties of experimental resin luting agents. Brazilian Oral Research, **21**, 194 (2007).

[13] Cabrera E., de la Macorra J. C.: Polymerization shrinkage influences microtensile bond strength. Journal of Dental Research, **86**, 227–231 (2007).

[14] Feilzer A. J., De Gee A. J., Davidson C. L.: Setting stress in composite resin in relation to configuration of the restoration. Journal of Dental Research, **66**, 1636–1639 (1987).

[15] Watts D. C., Satterthwaite J. D.: Axial shrinkage-stress depends upon both C-factor and composite mass. Dental Materials, **24**, 1–8 (2008).

eXPRESS Polymer Letters Vol.2, No.2 (2008) 93–100
Available online at www.expresspolymlett.com
DOI: 10.3144/expresspolymlett.2008.13

Graft copolymerization of MMA onto flax under different reaction conditions: a comparative study

B. S. Kaith[1], *S. Kalia*[2*]

[1]Department of Chemistry, Dr. B.R. Ambedkar National Institute of Technology (Deemed University), Jalandhar – 144 001 (Pb.) India
[2]Department of Chemistry, Singhania University, Pacheri Badi – 333 515 Jhunjhunu (Rajasthan) India

Received 26 October 2007; accepted in revised form 21 December 2007

Abstract. In the present paper, grafting of methyl methacrylate (MMA) onto flax fiber was carried-out under different reaction condition such as in air (IA), under pressure (UP) and under the influence of micro-wave radiations (MWR). Maximum percentage grafting (41.7%) has been observed in case of graft copolymerization carried-out in air at 55°C followed by grafting under pressure (36.4%) at 0.8 MPa and under the influence of microwave radiations (24.6%) at 210 W microwave power. Graft copolymers were characterized with FTIR spectroscopy, scanning electron microscopy (SEM), thermal analysis (TGA/DTA) and X-ray diffraction (XRD). Thermal stability of flax decreases on grafting under different reaction conditions. In case of XRD studies, cellulose crystals are better oriented in flax fiber followed by Flax-g-poly(MMA)-MWR, Flax-g-poly(MMA)-UP and Flax-g-poly(MMA)-IA.

Keywords: *thermal properties, IR, SEM, XRD*

1. Introduction

Modification of natural or synthetic polymers with the aim of imparting specific properties to the product has given a great thrust to macromolecular science. Desirable and targeted properties can be imparted to the natural or synthetic polymers through graft copolymerization in order to meet-out the requirement of specialized applications. It is a convenient and clean mean for altering the properties of numerous polymer back-bones. Mishra and Tripathy [1] reported the grafting of vinyl monomers onto natural fibers using peroxy diphosphate-tartaric acid redox system. Methyl acrylate was graft copolymerized onto cellulose in alkaline aqueous solution by using potassium ditelluratoargentate (III) redox system. The evidence of grafting was obtained from IR spectra and gravimetric analysis. Thermal stability, crystallinity and morphology of the graft copolymers were also studied [2]. Modifying the properties of natural polymers through graft copolymerization has been reported by various workers [3–13].

Since the grafting under pressure and microwave radiations is meagerly reported in literature, so in the present manuscript, we report the grafting of MMA onto flax under different reaction conditions and a comparative study has been made.

2. Experimental

2.1. Materials

Flax fiber was obtained from the Department of Agronomy, Chaudhary Sarwan Kumar Himachal Pradesh Krishi Vishwavidyalaya, Palampur (H. P.) India.

*Corresponding author, e-mail: susheel_kalia@yahoo.com

MMA (Fluka) was washed with 5% sodium hydroxide followed by water and was dried over anhydrous sodium sulphate. The dried monomer was distilled and the middle fraction was used. Ferrous ammonium sulphate (S d Fine) was recrystallized from hot water. Hydrogen peroxide (30% W/V, Qualigens Fine Chemicals) was used as received.

2.2 .Methods

2.2.1. Purification of flax fiber

Flax fiber was purified by Soxhlet extraction with acetone for 72 hours and was dried at room temperature.

2.2.2. Infra red spectroscopy (IR)

IR spectra of the ungrafted and grafted flax fiber were taken with KBr pellets on PERKIN ELMER RXI Spectrophotometer.

2.2.3. Scanning electron microscopy (SEM)

Scanning electron microscopic studies of flax and its graft copolymers were carried-out on Electron Microscopy Machine (LEO 435 VP). Since cellulose has non conducting behaviour so it was gold plated in order to prevent charge buildup on the sample. Scanning was synchronized with microscopic beam in order to maintain the small size over large distance relative to the specimen. The resulting images had a great depth of the field. A remarkable three-dimensional appearance with high resolution was obtained. The scans could easily verify the fact that cellulosic fibers lying apart in raw sample started forming bundles in the graft copolymers.

2.2.4. Thermogravimetric analysis/differential thermal analysis (TGA/DTA)

Thermogravimetric analysis and differential thermal analysis studies were carried-out in air at a heating rate of 10°C/minute on a thermal analyzer (LINSEIS, L-81 11).

2.2.5. X-ray diffraction (XRD) studies

X-ray diffraction studies were performed under ambient conditions on Bruker-D_8 advance model using CuK_α (1.5418 Å) radiation, Ni-filter and scintillation counter as detector at 40 kV and 40 mA on rotation between 5 to 50° at 2θ scale at 1 second step size and increment of 0.01 degree with 0.5° or 1.0 mm of divergent and anti-scattering slit. The small particle size of each sample of Flax-g-copolymers and flax fiber was made. Each sample was homogenously mixed prior to subjecting it for X-ray diffractometry.

The randomly oriented powdered sample with a uniform surface was exposed to X-rays from all possible planes of the sample and then measuring the scattering angle of the diffracted X-rays with respect to the angle of the incident beam. The continuous scans were taken and relative intensity was obtained. Crystallinity index (C.I.), which measures the orientation of the cellulose crystals in a fiber to the fiber axis, was determined by using the wide angle X-ray diffraction counts at 2θ angle close to 22 and 18°. The counter reading at peak intensity at 22° is said to represent the crystalline material and the peak intensity at 18° corresponds to the amorphous material in cellulose material [14, 15]. Percentage crystallinity (%Cr) [16] and crystallinity index (C.I.) [17, 18] were calculated according to Equations (1) and (2):

$$\%\mathrm{Cr} = \frac{I_{22}}{I_{22} + I_{18}} \cdot 100 \tag{1}$$

$$\mathrm{C.I} = \frac{I_{22} - I_{18}}{I_{22}} \tag{2}$$

where I_{22} and I_{18} are the crystalline and amorphous intensities at 2θ scale close to 22 and 18°, respectively.

2.2.6. Graft copolymerization of methyl methacrylate onto flax fiber

Grafting of MMA onto flax in air was carried out at water-bath with a range of temperatures (35–75°C). Grafting under pressure was carried out in autoclave at various pressures (0.5–1.7 MPa). Graft copolymerization of MMA onto flax under the influence of microwave radiations was carried out in microwave reactor at 210 W microwave power. Microwave frequency used was 2450 MHz.

Flax fiber (500 mg) was immersed in 100 ml of distilled water for 24 hours prior to its grafting. A definite ratio of Fenton's reagent was added to the

reaction flask as an initiator. A known amount of monomer was added to the reaction mixture, which was stirred constantly for a definite period of time. After the completion of reaction, the reaction flask was taken-out. The graft copolymer was Soxhlet extracted with acetone for about 5–6 hours so as to remove homopolymer. Further, the traces of homopolymer were separated from graft copolymer by stirring the graft copolymer in acetone for about 24 hours using magnetic stirrer. After homopolymer extraction, grafted fiber was dried in oven at 50°C till a constant weight was obtained and percentage graft yield was calculated. Different reaction parameters such as monomer concentration, initiator ratio, reaction temperature, reaction pressure, reaction time and pH were optimized so as to get maximum graft yield. Percentage graft yield (P_g) was calculated by Equation (3):

$$P_g = \frac{W_2 - W_1}{W_1} \cdot 100 \quad (3)$$

where W_1 and W_2 are the weights of flax fiber and grafted flax, respectively.

3. Results and discussion

It was postulated that ferrous ammonium sulphate interacts with hydrogen peroxide to produce OH^*, which is responsible for chain propagation reaction and helps in creating active sites on the polymeric back-bone where grafting can take place. In case of flax cellulose C_2, C_3 and C_6 hydroxyls are the most active sites for grafting of vinyl monomers. The mechanism for the grafting of methyl methacrylate in presence of Fenton's reagent onto flax is described by Equations (4)–(10):

$$Fe^{2+} + H{-}O{-}O{-}H \longrightarrow OH^* + Fe^{3+} + OH^- \quad (4)$$

$$OH^* + M \longrightarrow OH{-}M^* \xrightarrow{nM} OH{-}(M)^*_{n+1} \quad (5)$$

$$OH^* + Flax{-}H \longrightarrow Flax^* + H_2O \quad (6)$$

$$OH{-}(M)^*_{n+1} + Flax{-}H \longrightarrow Flax^* + OH{-}(M)^*_{n+1}{-}H \quad (7)$$

$$Flax^* + M \longrightarrow Flax{-}M^* \xrightarrow{nM} Flax{-}(M)^*_{n+1} \quad (8)$$

$$Flax{-}(M)^*_{n+1} + OH^* \longrightarrow Flax{-}(M)_{n+1}{-}OH \quad (9)$$

$$Flax{-}(M)^*_{n+1} + Fe^{3+} \longrightarrow Flax{-}(M)_{n+1} + Fe^{2+} \quad (10)$$

where M denotes the monomer.

On the basis of the above mechanism, reaction sites on the back-bone polymer can be generated by the reaction between OH^* and flax fiber (Equation (6)). As is evident from Equation (4), the formation of hydroxyl free radicals (OH^*) occurs by the reaction between ferrous ion (Fe^{+2}) and hydrogen peroxide (H_2O_2). The hydroxyl free radicals (OH^*) initiate the polymerization reaction to produce the growing polymeric chains (Equation (6)), which can attack the active sites of polymeric back-bone to give the graft copolymers (Equation (8)). Alternatively, the growing polymeric chains can lead to the formation of homo polymer (Equation (5)). However, the abstraction of hydrogen atom from main back-bone through Equation (6) is unlikely as the concentration of Fenton's reagent is very small. Therefore, hydroxyl free radicals will prefer to interact with vinyl monomer thereby giving growing polymeric chain which in turn creates active sites on flax back-bone by hydrogen abstraction (Equation (7)) [19]. Termination of various active species in the reaction mixture takes place by recombination (Equation (9)) and by transfer process (Equation (10)). The concentration of ferric ions (Fe^{+3}) in the reaction mixture plays an important role in getting the percentage grafting as it is directly involved in the termination of the reaction.

3.1. Optimized reaction parameters for maximum graft yield

Optimum reaction conditions for getting maximum graft yield in case of graft copolymerization of MMA onto flax fiber in air (41.7%), under pressure (36.4%) and under the influence of microwave radiations (24.6%) were: MMA ($mol \cdot l^{-1}$) = $1.96 \cdot 10^{-3}$, FAS:H_2O_2 (molar ratio) = 1:6, temperature [°C] = 55, time [minutes] = 120, pH = 7.0; MMA ($mol \cdot l^{-1}$) = $1.96 \cdot 10^{-3}$, FAS-H_2O_2 (molar ratio) = 1:7, pressure [MPa] = 0.8, time [minutes] = 120, pH = 9.0 and MMA ($mol \cdot l^{-1}$) = $1.96 \cdot 10^{-3}$, FAS:H_2O_2 (molar ratio) = 1:6, time [minutes] = 30, pH = 7.0, respectively (Table 1) [20, 21].

Table 1. Optimized reaction conditions for grafting of MMA onto flax

Reaction method	MMA concentration [mol/l]	Reaction time [minutes]	FAS:H_2O_2 ratio	pH	Temperature (pressure) Microwave Power
In air	$1.96 \cdot 10^{-3}$	120	1:6	7.0	55°C
Under pressure	$1.96 \cdot 10^{-3}$	120	1:7	9.0	0.8 MPa
Under microwave radiations	$1.96 \cdot 10^{-3}$	30	1:6	7.0	120 W

3.2. Comparative study of the percentage graft yield obtained in air, under pressure and under the influence of microwave radiations

As is evident from the above results that maximum percentage grafting (41.7%) has been observed in case of graft copolymerization carried-out in air followed by grafting under pressure (36.4%) and under the influence of microwave radiations (24.6%). In case of grafting in presence of microwave radiations, the electromagnetic waves which pass through the reaction medium cause the chain carrier free radicals to oscillate at a high speed, therefore, there exist a rapid collision between the different free radical species, resulting in chain termination reaction (equation (11)):

$$\text{Flax}—(\text{M})^{*}_{n+1} + —(\text{M})^{*}_{n+1}\ \text{Flax} \longrightarrow \text{Flax}—(\text{M})_{n+1}—(\text{M})_{n+1}\ \text{Flax} \quad (11)$$

where M = monomer

This leads to the formation of small molecular chain graft copolymers and resulted in getting the maximum graft yield in a short time. Hence a low graft yield was observed in case of grafting under the influence of microwave radiations.

In case of graft copolymerization carried-out under pressure though graft yield was higher than obtained in presence of microwave radiations but it was not as high as obtained in air. It is due to the fact that on carrying-out grafting under pressure, there are maximum chances of collisions of inter-free radical species, thereby resulting in early decay of the propagating free radical chain and giving rise to short chain graft copolymers. Under high pressure, homopolymerization also predominates graft copolymerization, OH^{*} radicals preferably react with the MMA molecules and results in the termination of growing homopolymer chains (Equation (12)). Hence a low graft yield was obtained in case of grafting under pressure.

$$^{*}\text{OH} + \text{M} \longrightarrow \text{OH}—\text{M}^{*} \xrightarrow{n\text{M}} \text{H}—\text{O}—(\text{M})^{*}_{n+1}$$

$$\text{HO}—(\text{M})^{*}_{n+1} + —(\text{M})^{*}_{n+1}\ \text{OH} \longrightarrow \text{HO}—(\text{M})_{n+1}—(\text{M})_{n+1}\ \text{OH} \quad (12)$$

Homopolymer

In case of grafting in air, the growing free radical chains do not face rapid collision and yield long chain graft copolymers. Moreover, OH^{*} radicals get a lot of opportunities to strike the back-bone polymer and result in the abstraction of H-atom, thereby, generating free radical sites on the back-bone, which further propagate the graft copolymerization through interaction with monomer species Equation (13)):

$$^{*}\text{OH} + \text{Flax–H} \longrightarrow \text{Flax}^{*} + \text{H}_2\text{O}$$

$$\text{Flax}^{*} + \text{M} \longrightarrow \text{Flax} — \text{M}^{*} \xrightarrow{n\text{M}} \text{Flax} —(\text{M})— \quad (13)$$

Graft copolymer

On the other hand, growing long chain monomer species attack the active sites of the back-bone polymer generating graft copolymer. Whereas, in case of graft copolymerization carried-out under pressure and under the influence of microwave radiations, the possibilities of generation of active sites on the flax back-bone are minimized due to rapid collision between the different active species, thereby, resulting in lower graft yields as compared to the grafting in air.

3.3. Characterization of graft copolymers

3.3.1. Infra red spectral analysis (IR)

IR spectrum of the flax fiber showed a broad peak at 3422.8 cm^{-1} due to bonded –OH group and at 2918.8, 1653.5 and 1058.7 cm^{-1} arising from $–CH_2$, C–C and C–O stretching, respectively. However, in case of Flax-g-poly(MMA)-IA, Flax-g-poly(MMA)-UP and Flax-g-poly(MMA)-MWR an

additional peak at 1734.1, 1735.0 and 1731.2 cm^{-1}, respectively, has been observed due to >C=O group of MMA. This suggests that MMA has been grafted onto flax through covalent linkages [20, 21].

3.3.2. Scanning electron microscopy (SEM)

It is quite evident from Figures 1a–1c that there has been a sufficient deposition of poly(MMA) onto flax. Comparison of the scanning electron micrographs of flax fiber (Figure 1), Flax-g-poly(MMA)-IA, Flax-g-poly(MMA)-UP and Flax-g-poly (MMA)-MWR reveals a clear cut distinction between the ungrafted and different grafted fibers [20, 21].

3.3.3. Thermal properties (TGA/DTA)

Thermogravimetric analysis (TGA) is an important technique to measure the physical properties of a substance and its reaction products as a function of temperature whilst the substance is subjected to a controlled temperature program [22]. Differential thermal analysis on the other hand, is important to identify polymers, to generate phase diagram and for phase transition studies. It helps to determine melting and decomposition of organic compounds [23].

It is evident from Table 2 that initial and final decomposition temperatures of flax fiber are 279.9 and 489.1°C, respectively (Figure 2). Whereas, in case of Flax-g-poly(MMA)-IA, Flax-g-poly(MMA)-UP and Flax-g-poly(MMA)-MWR, the initial

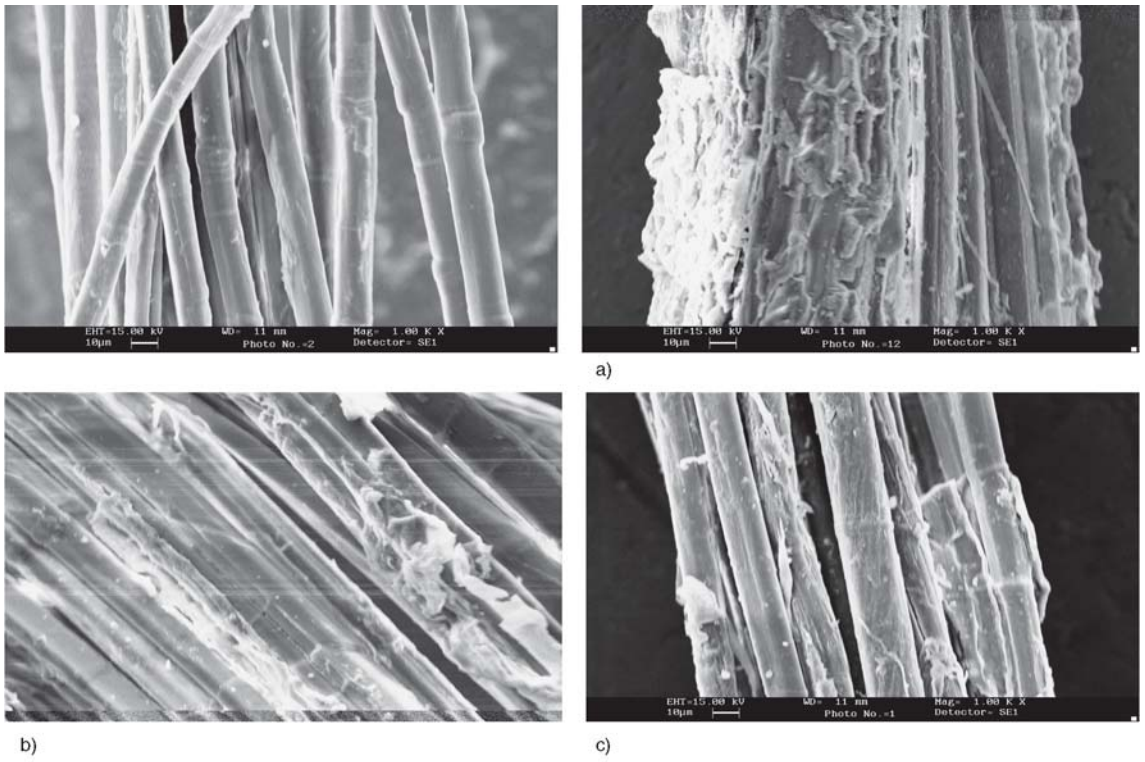

Figure 1. SEM of fiber. a – SEM of Flax-g-poly(MMA)-IA, b – SEM of Flax-g-poly(MMA)-UP, c – SEM of Flax-g-poly(MMA)-MWR

Table 2. Thermal analysis of flax and its graft copolymers

Sr. No.	Sample	TGA		DTA Exothermic peaks at temperature (μV)
		IDT	FDT	
1.	Flax fiber	279.9°C	489.1°C	325.3°C (13.8 μV)/ 455.3°C (38.9 μV)
2.	Flax-g-poly(MMA)-IA	212.5°C	436.3°C	344.9°C (20 μV)/ 395.2°C (19 μV)
3.	Flax-g-poly(MMA)-UP	248.1°C	418.2°C	359.5°C (32.9 μV)/ 393.4°C (30.7 μV)
4.	Flax-g-poly(MMA)-MWR	207.9°C	436.2°C	383.7°C (41.5 μV)

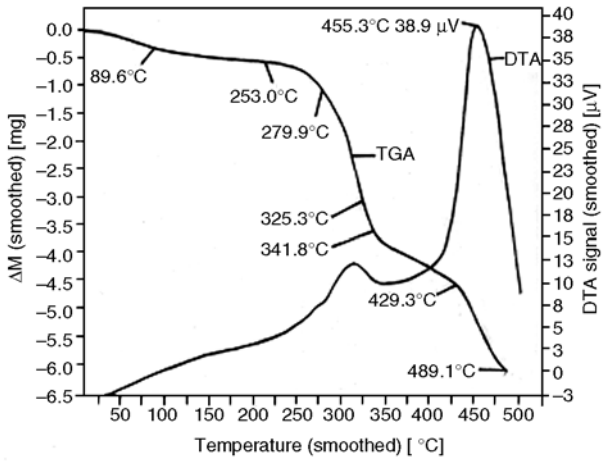

Figure 2. TGA/DTA curve of flax fiber

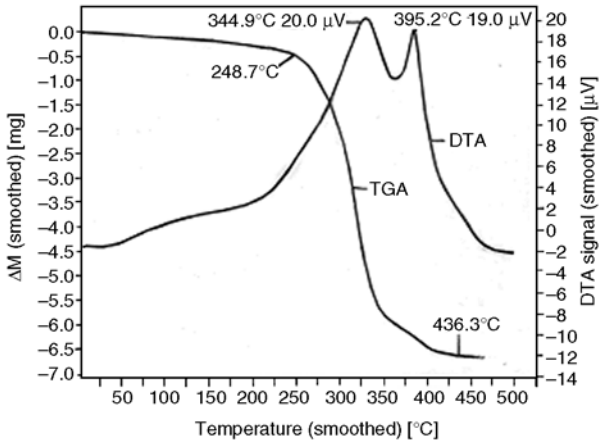

Figure 3. TGA/DTA curve of Flax-g-poly(MMA)-IA

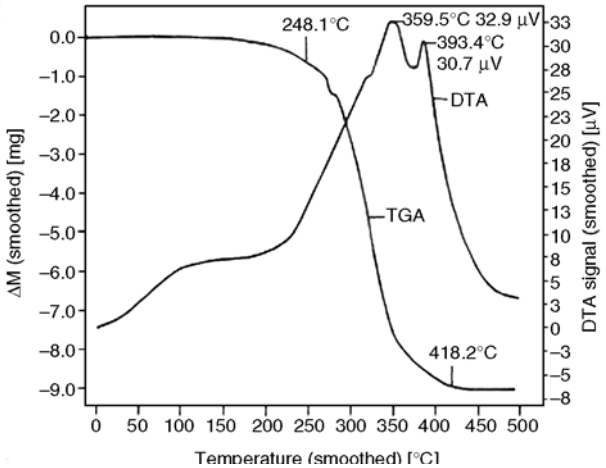

Figure 4. TGA/DTA curve of Flax-g-poly(MMA)-UP

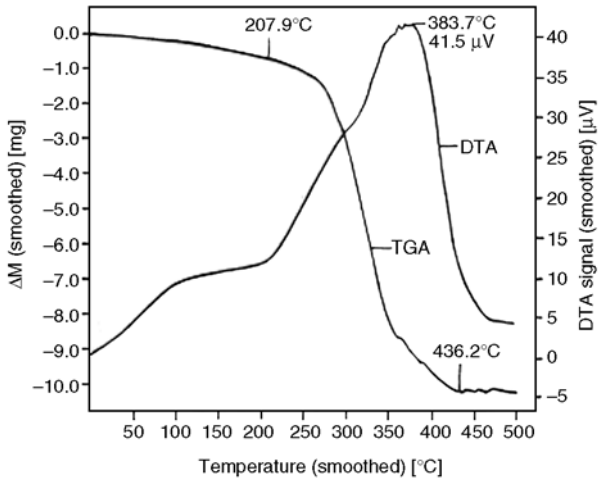

Figure 5. TGA/DTA curve of Flax-g-poly(MMA)-MWR

decomposition temperatures (IDTs) are 248.7, 248.1 and 207.9°C, respectively and the final decomposition temperatures (FDTs) are 436.3, 418.2 and 436.2°C, respectively (Figures 3–5). It is evident from the Table 2 that grafting of MMA onto flax decrease the thermal stability. It is explained on the basis that on grafting the crystalline lattice of the fiber is disturbed and the fiber becomes more amorphous, thereby resulting in lower FDTs of the graft copolymers obtained. Moreover, in case of flax fiber three stage decomposition has been observed with maximum weight loss occurring between 279.9–341.8°C (37.0%), 341.8–429.3°C (12.57%) and 429.3–489.1°C (22.57%). Whereas, graft copolymers: Flax-g-poly (MMA)-IA, Flax-g-poly(MMA)-UP and Flax-g-poly(MMA)-MWR, showed single stage decomposition only with maximum weight loss of 87.71% at 436.3°C, 67.36% at 418.2°C and 80.55% at 436.2°C, respectively. This can again be explained on the basis of disturbance in the crystal lattice of flax fiber on graft copolymerization. Flax fiber becomes more amorphous after grafting process.

Differential thermal analysis of flax fiber showed exothermic peaks at 325.3°C (13.8 µV) and 455.3°C (38.9 µV), which indicates the complete break down of C–C and C–O bonds of the crystalline region (Table 2 and Figure 2). However, in case of Flax-g-poly(MMA)-IA, Flax-g-poly (MMA)-UP and Flax-g-poly(MMA)-MWR, a continuous exothermic rise in temperatures has been observed and the exothermic peaks at 344.9°C (20 µV)/395.2°C (19 µV), 359.5°C (32.9 µV)/ 393.4°C (30.7 µV) and 383.7°C (41.5 µV), respectively, have been obtained (Figures 3–5). As is evident from Table 2 that broader exothermic peak at 344.9°C (20 µV) as compared to the peak at 395.2°C (19 µV) in case of Flax-g-poly(MMA)-IA

is the evidence of the fact that most of the crystalline portion of the flax has been disturbed during the grafting process. Similar results have been found in case of graft copolymers prepared under pressure and under the influence of MWR.

3.3.4. X-ray diffraction (XRD) studies

It is evident from Table 3 that flax fiber, Flax-g-poly(MMA)-IA, Flax-g-poly(MMA)-UP and Flax-g-poly(MMA)-MWR showed 77, 64, 68 and 69% crystallinity, respectively. Crystallinity index of flax fiber, Flax-g-poly(MMA)-IA, Flax-g-poly (MMA)-UP and Flax-g-poly(MMA)-MWR has been observed to be 0.7005, 0.4477, 0.5207 and 0.5502, respectively.

The X-ray diffraction spectra of flax fiber and graft copolymers (Figure 6) were analyzed and it has been found that the spectrum of flax fiber is more convex than that of graft copolymers. In case of flax fiber, the incorporation of poly(MMA) chains to the back-bone of the flax back-bone had impaired the crystallinity of flax fiber. Therefore, on grafting %Cr decreases rapidly with reduction in its stiffness and hardness [24, 25]. Whereas, graft copolymers prepared under the influence of microwave radiations showed a fewer changes in the crystalline lattice in comparison to graft copolymers prepared in air and under pressure. This is due to the reason that optimum reaction time for grafting under MWR was very low and thus the fiber underwent a fewer changes in its crystal structure. On the other hand, a lower crystallinity index in case of graft copolymers prepared in air and under pressure indicates poor order of cellulose crystals in the grafted fibers. C.I. of Flax-g-poly(MMA)-MWR (0.5502) is higher than that of Flax-g-poly (MMA)-IA (0.4477) and Flax-g-poly(MMA)-UP (0.5207). Although C.I. gives a quantitative measure of the orientation of the cellulose crystals in fibers, X-ray diffraction patterns are visual indicators of the orientation of the cellulose crystals. The diffraction of flax fiber produces narrow and bright patterns that are characteristic of oriented crystals [26]. On the other hand, the diffraction pictures of Flax-g-poly(MMA)-IA, Flax-g-poly(MMA)-UP and Flax-g-poly(MMA)-MWR showed long diffracting arcs that end sharply. This is due to misorientation of the cellulose crystals to the fiber axis during grafting as indicated by the lower crystallinity index in Flax-g-poly(MMA)-IA, Flax-g-poly(MMA)-UP and Flax-g-poly(MMA)-MWR.

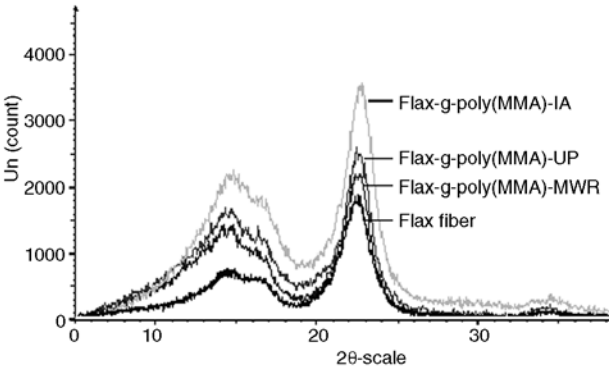

Figure 6. X-ray diffraction studies of Flax-g-copolymers vis-à-vis flax fiber

4. Conclusions

Grafting through micro-wave radiation technique is an effective method in terms of time consumption and cost effectiveness. Maximum percentage grafting has been observed in case of grafting carried-out in air followed by grafting under pressure and under the influence of microwave radiations. Flax faces less surface deformations during grafting process under the influence of microwave radiations as compared to grafting in air and under pressure, thereby retaining better crystalline structure.

Table 3. Percentage crystallinity (%Cr) and crystallinity index (C.I.) of flax fiber and graft copolymers prepared under different reaction conditions

Sr. No.	Sample	P_g	at 2θ scale		%Cr	C.I.
			I_{22}	I_{18}		
1.	Flax fiber	–	1780	533	77	0.7005
2.	Flax-g-poly(MMA)-IA	41.7	3348	1849	64	0.4477
3.	Flax-g-poly(MMA)-UP	36.4	2944	1411	68	0.5207
4.	Flax-g-poly(MMA)-MWR	24.6	2466	1109	69	0.5502

References

[1] Mishra M. K., Tripathy A. K.: Grafting vinyl monomers onto natural fibres. Graft copolymerization of methyl methacrylate onto wool and silk using peroxydiphosphate-tartaric acid redox system. European Polymer Journal, **17**, 1225–1226 (1981).

[2] Liu Y., Yang L., Shi Z., Li J.: Graft copolymerization of methyl acrylate onto cellulose initiated by potassium ditelluratoargentate(III). Polymer International, **53**, 1561–1566 (2004).

[3] Tiwari A., Singh V.: Synthesis and characterization of electrical conducting chitosan-graft-polyaniline. Express Polymer Letters, **1**, 308–317 (2007).

[4] Eromosele I. C., Hamagadu T. J.: Graft copolymerization of methylmethacrylate onto caesarweed fibers by the potassium permanganate-toluene redox system. Journal of Applied Polymer Science, **50**, 645–649 (1993).

[5] Bhattacharya A., Misra B. N.: Grafting: A versatile mean to modify polymers techniques, factors and applications. Progress in Polymer Science, **29**, 767–814 (2004).

[6] Bhattacharyya S. N., Maldas D.: Graft copolymerization onto cellulosics. Progress in Polymer Science, **10**, 171–270 (1983).

[7] Wielen L. C. V., Ragauskas A. J.: Grafting of acrylamide onto cellulosic fibers via dielectric-discharge. European Polymer Journal, **40**, 477–482 (2004).

[8] Margutti S., Vicini S., Proietti N., Capitani D., Conio G., Pedemonte E., Segre A. L.: Physical-chemical characterization of acrylic polymers grafted on cellulose. Polymer, **43**, 6183–6194 (2002).

[9] Sabaa M. W., Mokhtar S. M.: Chemically induced graft copolymerization of itaconic acid onto cellulose fibers. Polymer Testing, **21**, 337–343 (2002).

[10] Singh V., Tiwari A., Pandey S., Singh S. K.: Peroxydisulfate initiated synthesis of potato starch-graft-poly(acrylonitrile) under microwave irradiation. Express Polymer Letters, **1**, 51–58 (2007).

[11] Kaith B. S., Kumar K.: In air synthesis of Psy-cl-poly(AAm) network and its application in water-absorption from oil-water emulsions. Express Polymer Letters, **1**, 474–480 (2007).

[12] Princi E., Vicini S., Proietti N., Capitani D.: Grafting polymerization on cellulose based textiles: ^{13}C solid state NMR characterization. European Polymer Journal, **41**, 1196–1203 (2005).

[13] Tsukada M., Islam S., Arai T., Boschi A., Freddi G.: Microwave irradiation technique to enhance protein fibre properties. Autex Research Journal, **5**, 40–48 (2005).

[14] Wakelin J. H., Virgin H. S., Crystal E.: Development and comparison of two X-ray methods for determining the crystallinity of cotton cellulose. Journal of Applied Physics, **30**, 1654–1662 (1959).

[15] Mwaikambo L. Y., Ansell M. P.: Chemical modification of hemp, sisal, jute, and kapok fibers by alkalization. Journal of Applied Polymer Science, **84**, 2222–2234 (2002).

[16] Agrawal A. M., Manek R. V., Kolling W. M., Neau S. H.: Studies on the interaction of water with ethylcellulose: Effect of polymer particle size. AAPS PharmSciTech, **4**, 11 pages in Article 60 (2003).

[17] Reddy N., Yang Y.: Structure and properties of high quality natural cellulose fibers from cornstalks. Polymer, **46**, 5494–5500 (2005).

[18] Segal L. C., Creely J. J., Martin A. E., Conrad C. M.: An empirical method for estimating the degree of crystallinity of native cellulose using the X-ray diffractometer. Textile Research Journal, **29**, 786–794 (1959).

[19] Misra B. N., Chandel P. S., Dogra R.: Grafting onto wool. III. Graft copolymerization of poly(vinyl acetate) by use of Fenton's reagent as initiator. Journal of Polymer Science: Polymer Chemistry Edition, **16**, 1801–1805 (1978).

[20] Kaith B. S., Singha A. S., Kumar S., Misra B. N.: FAS-H_2O_2 initiated graft polymerization of methylmethacrylate onto flax and evaluation of some physical and chemical properties. Journal of Polymer Materials, **22**, 425–432 (2005).

[21] Kaith B. S., Kalia S.: Preparation of micro-wave radiation induced graft copolymers and their applications as reinforcing material in phenolic composites. Polymer Composites, In press (2008).

[22] Mackenzie R. C.: Nomenclature in thermal analysis, part IV. Journal of Thermal Analysis and Calorimetry, **13**, 387–392 (1978).

[23] Skoog D. A., Holler F. J., Nieman T. A.: Principles of instrumental analysis. Saunders Golden Sunburst Series, Philadelphia (2001).

[24] Billmeyer F. W. Jr.: Textbook of polymer sciences. Wiley and Sons, New York (1984).

[25] Morton E. W., Hearle J. W. S.: Physical properties of textile fibers. The Textile Institute, Manchester (1993).

[26] Cao J., Billows C. A.: Crystallinity determination of native and stretched wool by X-ray diffraction. Polymer International, **48**, 1027–1033 (1999).

eXPRESS Polymer Letters Vol.2, No.2 (2008) 101–110
Available online at www.expresspolymlett.com
DOI: 10.3144/expresspolymlett.2008.14

Hybrid inorganic-organic nano- and microcomposites based on silica sols and synthetic polyelectrolytes

S. E. Kudaibergenov[1,2,3], G. S. Tatykhanova[3], B. Zh. Arinov[2], S. K. Kozhakhmetov[2], V. O. Aseyev[4]*

[1]Institute of Polymer Materials and Technology, Almaty, 050004, Republic of Kazakhstan
[2]JSC Scientific-Production Center 'Ulba', National Atomic Company 'Kazatomprom', Ust-Kamenogorsk, 070005, Republic of Kazakhstan
[3]Semipalatinsk State Shakarim University, Semipalatinsk, Republic of Kazakhstan
[4]Helsinki University, Laboratory of Polymer Chemistry, Helsinki, Finland

Received 18 November 2007; accepted in revised form 25 December 2007

Abstract. Interaction between anionic (and cationic) colloidal particles of silica having the particles diameters 12 and 22 nm with synthetic cationic (and anionic) polyelectrolytes of various nature and structure was studied by potentiometric, conductimetric spectroturbidimetric and viscometric methods in aqueous solution. It was shown that the complexation of silica nanoparticles with linear polyelectrolytes leads to formation of mostly stoichiometric interpolyelectrolyte complexes (IPEC) which precipitate from aqueous solution. Casting of water-soluble IPEC followed by thermal treatment gives thin composite films insoluble in water while 'layer by layer' (LbL) deposition of polyelectrolyte components onto silica sols leads to formation of multilayered nano- and microcomposites. The possible mechanism of formation of LbL multilayers consisting of silica sol (SiO_2) 'cores' and polyethyeleneimine-polyacrylic acid (PEI-PAA) 'shells' was suggested. It was found that in diluted aqueous solution the radius of gyration, R_g and hydrodynamic radius, R_h^{mean} of LbL particles are independent on LbL concentration and smaller than 100 nm. The zeta potential values of LbL particles are arranged between –10 and –30 mV. The average size of LbL particles estimated by scanning electron microscopy (SEM) is in the range of 200–500 nm. Thermal treatment of LbL multilayers followed by etching of (SiO_2) 'core' by HF leads to formation of a series of spherical nanocavities and blob-like microcavities.

Keywords: *nanomaterials, silica nanoparticles, linear polyelectrolytes, interpolyelectrolyte complexes*

1. Introduction

Hybrid inorganic-organic nanocomposites comprising inorganic nanoparticles and functional polymers are novel and unique class of nanomaterials that synergistically combine and enhance the best properties of inorganic and organic polymers [1–4]. The potential application fields of such hybrids can include specialty coatings, membranes, sensors, biomaterials, drug delivery systems, catalysts etc. The most common principle concepts of incorporation of inorganic nanoparticles into polymer matrix and the resulting properties of such materials have been reviewed by authors [5–7]. Classification of polymer/silicate nanocomposites based on synthetic techniques was suggested in [8]. Although titanium [9, 10] and aluminum [11] oxides have been utilized as the inorganic components interacting with functional polymers, the colloid silica due to easy preparation by sol-gel technology [12] is one of the promising inorganic polymeric materials that interacts with polyelectrolytes and forms, so called interpolyelectrolyte complexes (IPEC) – products of interaction of two oppositely charged polyelectrolytes [13–17]. Mech-

*Corresponding author, e-mail: ipmt-kau@usa.net

anisms of formation, structure and properties of IPECs based on synthetic polyelectrolytes have been thoroughly investigated by Bixler and Michaelis [18], Tsuchida and Abe [19], Kabanov [17], Zezin and Kabanov [20], Bekturov and Bimendina [21], Philipp *et al.* [22]. Polyelectrolyte complex formation between strong polyanion and cationic nanogels was studied by Ogawa *et al*. [23]. Recently [24] the multilayered nanomaterials were developed on the basis of hydrogen-bonded complexes of polyacrylic acid and methylcellulose.

Ultrathin membranes with participation of colloidal particles and cationic polyelectrolytes [25], layered double hydroxide and anionic polyelectrolytes [26], and colloidal biocatalysts consisting of polystyrene-based colloid particles coated with glucose oxidase and hoseradish peroxidase [27] as well as polyelectrolyte composite films [28] and nanotubes [29] were assembled *via* the LbL self-assembling. Hybrid ternary organic-inorganic films consisting of chitosan, poly(monomethyl)itaconate and silica nanoparticles were designed by Martinez *et a*l. [30] and further the same authors [31] embedded the semiconductor CdS nanoparticles into organic-inorganic hybrid by *in situ* technique. Thus the understanding of the basic principles of fabrication of composite inorganic-organic nano- and micromaterials where one component phase is nanoparticle is a challenging task [32].

The present communication deals with studying of the formation and characterization of hybrid inorganic-organic nano- and microcomposites as a result of interpolyelectrolyte complexation between silica nanoparticles and linear polyelectrolytes.

2. Experimental

2.1. Materials

Colloidal particles of silica are commercial products purchased from Ludox (Grace GmbH & Co. KG, Worms, Germany) were abbreviated as HS-40, AS-40 and CL in dependence of surface charge, nature of counterions, particle size and surface area. Table 1 represents some physico-chemical characteristics of anionic and cationic nanoparticles of silica.

Table 1. Physico-chemical characteristics of colloidal silica nanoparticles

Characteristics	Type of colloidal particles		
	HS-40	**AS-40**	**CL**
Surface charge	–	–	+
Counterion	Na^+	NH_4^+	Cl^-
SiO_2 [wt%]	40	40	30
Na_2O [wt%]	0.41	0.05–0.08	–
Particles size [nm]	12	22	12
Surface area [m^2/g]	240	140	240
pH (25°C)	9.7	9.1	4.5

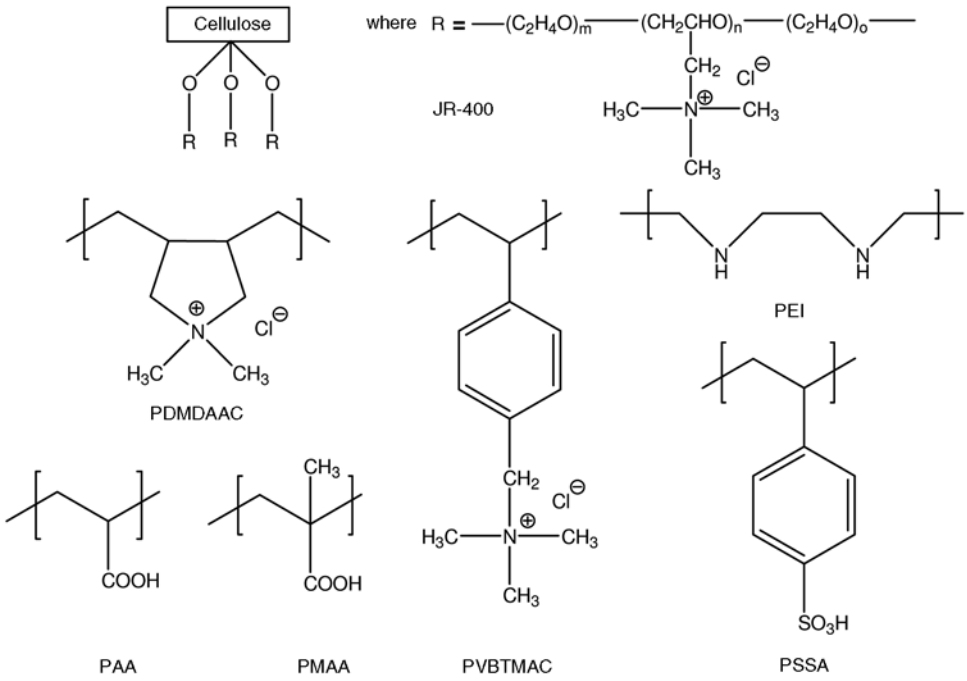

Figure 1. Structural formulas of linear polyelectrolytes

Table 2. Some of physico-chemical characteristics of linear polyelectrolytes

Characteristics	Linear polyelectrolytes						
	JR-400	**PDMDAAC**	**PVBTMAC**	**PEI**	**PSSA**	**PAA**	**PMAA**
Surface charge	+	+	+	+	–	–	–
Counterion	Cl^-	Cl^-	Cl^-	OH^-	H^+	H^+	H^+
M·10^{-3} [Dalton]	100–3000	219	100	25	500	450	250
pH (25°C)	5,66	4,90	5,48	8,37	8,01	3,00	3,40

As linear cationic and anionic polyelectrolytes the quaternized ammonium salts of cellulose derivatives (JR-400) [33], poly-N,N-dimethyl-N,N-diallylammonium chloride (PDMDAAC), poly-N-vinylbenzyl-N,N,N-trimethylammonium chloride (PVBTMAC), polyethyleneimine (PEI), polystyrenesulfonic acid (PSSA), polyacrylic (PAA) and polymethacrylic (PMAA) acids purchased from Polysciences, Inc. (Warrington, PA, USA) were used. Structural formulas of water-soluble polyelectrolytes and some of their physico-chemical characteristics are represented in Figure 1 and Table 2. In addition to linear polyelectrolytes, microgel of PDMDAAC with average diameters of particles 1–3 μm was used.

2.2. Methods

Potentiometric and conductimetric titrations were carried out with the help of combined pH/Conductometer 'Mettler-Toledo MPC-227' (Schweiz, Switzerland) at room temperature. Turbidity of solutions was measured by photoelectrocolorimeter 'FEK-56' (Moscow, Russia) at $\lambda = 340$ nm and room temperature. Viscometric measurements were carried out on Ubbelohde viscometer at 298 ± 0.1 K. Optical microscope of LOMO (Saint-Petersburg, Russia) was used for observation of thin powders and multilayered films structures.

Dynamic and static light scattering experiments were conducted with a Brookhaven Instruments (NY, USA) BI-200SM goniometer, a BI-Turbo-Corr digital auto/crosscorrelator, and a BI-Cross-Corr detector, including two BI-DS1 detectors. A Sapphire 488-100 CDRH laser from Coherent GmbH operating at the wavelength of $\lambda_0 = 488$ nm (vertically polarized) and the power adjusting from 10 to 50 mW was a light source. The scattering angles were varied in the range of $\theta = 30$–$150°$. In the DLS experiments, pseudo cross-correlation functions of the scattered light intensity, $G_2(t)$, were collected with the self-beating method [34]. The time average intensity of the scattered light, I_θ, was recorded simultaneously. The intensities measured in counts of photons per second, cps, were normalised with respect to the Rayleigh ratio of toluene. The temperature of the samples was controlled by means of a Lauda RC 6C thermostated water bath. For light scattering experiments the selected concentrations of LbL samples were $C_p = 0.121$, 0.605, and 12.1 mg/ml. Aqueous solutions were passed through the hydrophilic Millex-HV 0.45 μm pore size and 13 mm in diameter filters prior to measurements to remove dust particles.

Zeta-potential measurements were performed with a Nano-ZS Zetasizer ZEN3600 from Malvern Instruments (Malvern, UK) equipped with 4 mW He-Ne laser operating at $\lambda_0 = 633$ nm. Nano-ZS Zetasizer is based on the back scattering data detection ($\theta = 173°$). M3-PALS technique and Smoluchowski analysis is used to measure the zeta-potential. Size & Zeta-potential-DTS1060 folded capillary cell was employed for the simultaneous size and zeta-potential measurements. Temperature was stabilized with a Peltier temperature control.

SEM pictures were obtained for freeze-dried LbL samples using Hitachi S-4800 (Tokyo, Japan) instrument. Freeze-drying solution was deposited on a grid for SEM and quickly frozen under liquid nitrogen. The grid then was placed in vacuum to remove water.

2.3. Preparation of thin powders, composite films and layer-by-layer compositions of IPEC

Bidistilled water was used for preparation of colloidal particles and polyelectrolyte solutions. Aqueous solutions of polyelectrolytes (0.01 mol/l) were added dropwise to the aqueous solution of colloidal silica (0.01 mol/l) under stirring. The precipitated IPEC particles were separated from supernatant by preparative centrifuge 'T-62' (Warsaw,

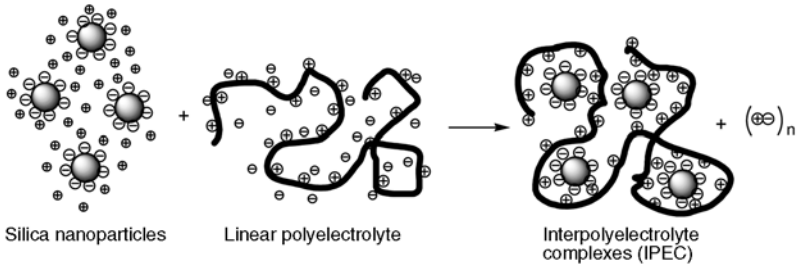

Figure 2. Scheme of IPEC formation between silica sols and linear polyelectrolytes

Poland) at 5000 rpm. They were then washed with acetone several times. After drying for one day in vacuum oven, the IPEC particles were obtained in the form of thin powder.

Since the IPEC obtained by mixing of aqueous solutions of HS-40 and JR-400 preserved in aqueous solution, by casting the equimolar mixture of HS-40 and JR-400 onto Teflon surface the thin films were fabricated. After thermal treatment of thin films at 100°C for one day they became insoluble but swellable in water. The LbL assembly process developed for planar solid substrates was adapted for silica sols. At first the dilute aqueous solutions of silica sols, PEI and PAA with concentration of C = 10^{-3} mol/l were prepared. To 1 ml of AS-40 1 ml of PEI was added under stirring during 5 min. Then 1 mL of PAA was added to 2 ml mixture of AS-40 and PEI. Sequential addition of PAA and PEI to AS-40/PEI was continuously repeated 10 times under constant stirring time 5 min for each stage. The obtained solution consisting of SiO_2 'core' and PEI-PAA 'shell' was abbreviated as $(SiO_2)/(PEI\text{-}PAA)_{10}$ (where 10 correspond to number of PEI-PAA multilayers). One drop of opalescent solution of $(SiO_2)/(PEI\text{-}PAA)_{10}$ was deposited onto the glass surface, dried in air and then heated in oven at 100°C during 6 h. Etching of SiO_2 from $(SiO_2)/(PEI\text{-}PAA)_{10}$ compositions was provided by dipping the glass surface into 0.01 mol/l HF during 1 min and rinsing with bidistilled water. This procedure was repeated the required times. Finally the multilayered coatings were dried in air.

3. Results and discussion

According to [13–16] the mechanism of interaction of silicate sols with linear polyelectrolytes can be considered as cooperative adsorption of negatively charged SiO_2 nanoparticles onto positively charged polyelectrolytes (Figure 2). The addition of a polycation to a solution of a silicate ions results in precipitation of IPEC.

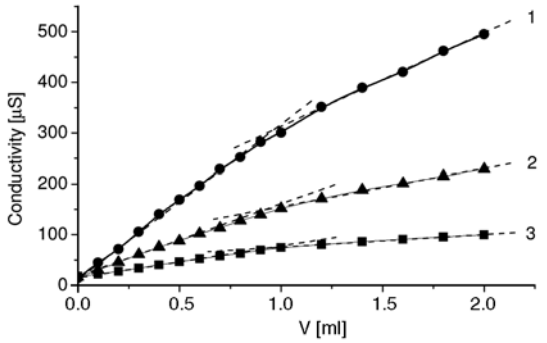

Figure 3. Conductimetric titration curves of colloidal dispersions of CL (1), AS-40 (2) and HS-40 (3) by PSSA (1), JR-400 (2) and PDMDAAC (3)

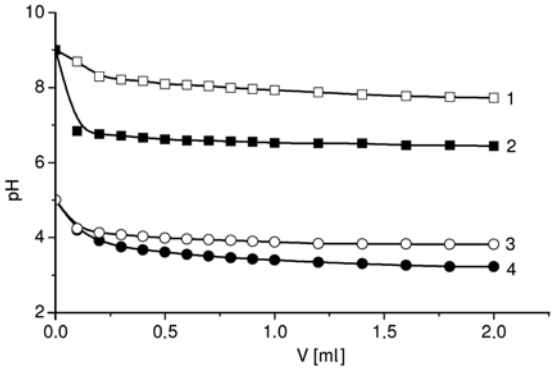

Figure. 4. Potentiometric titration curves of HS-40 (1, 2) and CL (3, 4) by PDMDAAC (1), JR-400 (2), PAA (3) and PMAA (4)

Figures 3 and 4 illustrate the conductometric and potentiometric titration curves of silicate sols by linear polyelectrolytes. Compositions of IPEC found from the inflection points are equal or close to equimolar ratio of interacting components (Table 3). Increasing of the optical density and viscosity of systems indicates an aggregation of IPEC particles (Figure 5).

Photos of colloidal silica, polyelectrolyte solution, precipitated IPEC, and IPEC powders are shown in Figure 6.

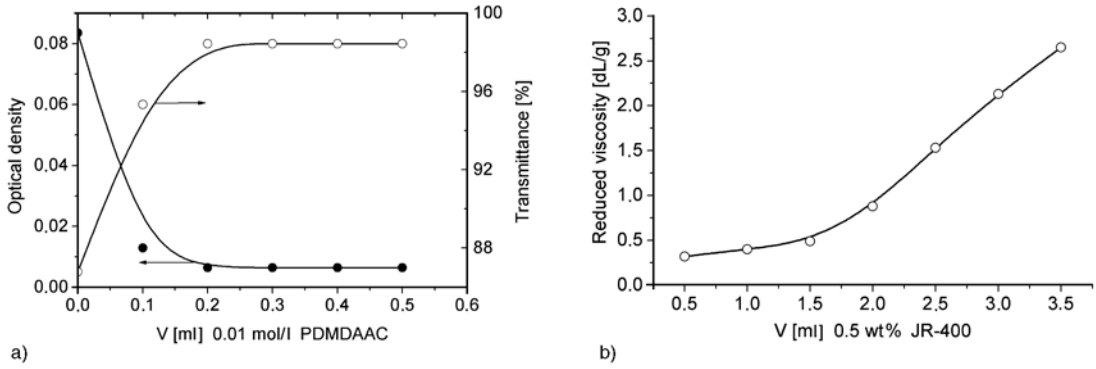

Figure 5. Spectroturbidimetric (a) and viscometric (b) titration curves of colloidal silica AS-40 by PVBTMAC (a) and JR-400 (b)

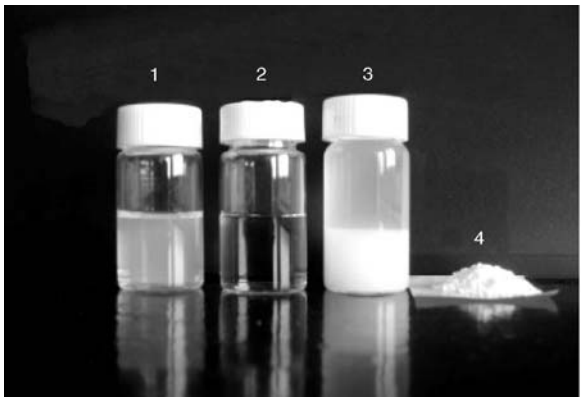

Figure 6. Photos of colloidal silica AS-40 (1), aqueous solution of JR-400 (2), precipitated IPEC (3), and IPEC thin powders (4)

Table 3. Compositions of IPEC determined from the inflection points of conductimetric and potentiometric titration curves

Polyelectrolytes	Composition of IPEC [mol/mol]		
	AS-40	HS-40	CL
JR-400	1 : 1.15	1 : 1	–
PDMDAAC	1 : 1.04	1 : 1.33	–
PVBTMAC	1 : 1.12	1 : 1	–
PEI	1 : 1.05	1 : 1	–
PSSA	–	–	1 : 1.2
PAA	–	–	1 : 1.1
PMAA	–	–	1 : 1
PDMDAAC microgel	1 : 1	1 : 1	–

Competition interpolyelectrolyte reactions between IPEC and strong polyelectrolytes are of great interest [17]. It is known that polyanions such as polyethylenesulfonate and polystyrenesulfonate are able to replace polycarboxylates, for instance PAA and PMAA, from the IPEC containing quaternized ammonium moieties as cationic polyelectrolytes. The driving force of competition reaction is specific, in addition to Coulomb forces, binding of sulfonate to quaternized ammonium groups. In this connection one can suppose that addition of aqueous solution of PSSA to IPEC based on AS-40 and JR-400 will lead to replacement of silica sols from the IPEC particles and formation of new IPEC between PSSA and JR-400. This is confirmed by conductometric titration of IPEC particles by aqueous solution of PSSA. The formation bigger flocs and the presence of inflection point on conductimetric curves at a molar ratio of [PSSA]:[JR-400] = 1:1 that coincides well with conductometric titration curves of JR-400 by PSSA and the appearance of SiO_2 particles in supernatant confirms the release of silica sols from the initial IPEC. Interpolyelectrolyte reaction of replacement at which

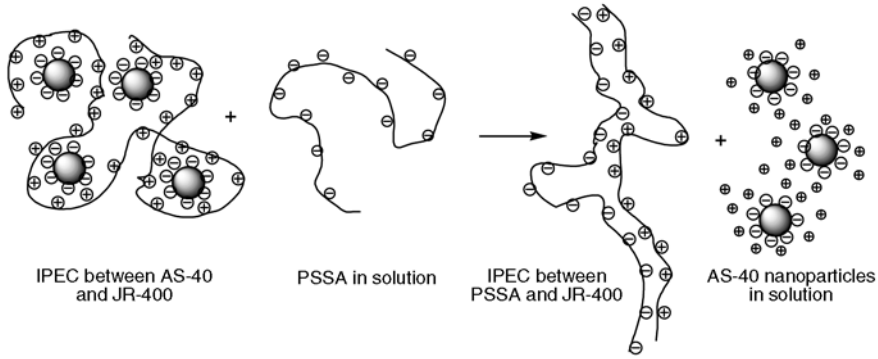

Figure 7. Release of silica sols from the IPEC as a result of competition reaction between IPEC and PSSA

Table 4. Dimensions of the $(SiO_2)/(PEI\text{-}PAA)_{10}$ LbL complex particles in water

LbL C_p [mg/ml]	Zimm		Guinier		CONTIN
	R_g^Z [nm]	R_g^Z/R_h^{mean}	R_g^G [nm]	R_g^G/R_h^{mean}	R_h^{mean} [nm]
$Cp \to 0$	72.4	0.76	88.8	0.92	96.4
0.121	70.7	0.74	82.9	0.87	95.7
0.605	72.2	0.73	83.1	0.84	99.3
12.1	74.5	0.81	89.6	0.97	92.4

SiO_2 particles are displaced by PSSA can schematically be represented by the following Figure 7.

Thus IPEC formation between silica sols and cationic polyelectrolytes and interpolyelectrolyte competition reactions with participation of strong polyelectrolytes can serve as preparative and technological basis for extraction and purification of SiO_2 nanoparticles.

The data of light scattering experiments for LbL consisting of $(SiO_2)/(PEI\text{-}PAA)_{10}$ are collected in Table 4. The main conclusion from these results is that the radius of gyration, R_g and hydrodynamic radius, R_h^{mean} of LbL particles calculated by using of Zimm and Guinier methods and of an inverse Laplace program CONTIN are independent on LbL concentration and smaller than 100 nm.

Following the LbL preparation procedure, the most expected conformation of (PEI-PAA)10 shell layer is a swollen sphere (or a thick-walled sphere). The R_g/R_h ratios listed in Table 4 support this model. The Zimm's method is typically used for structures, density of which increases towards the centre of gravity, e.g. a polymer coil. In this respect the Guinier's method should give more reliable value of R_g. We tried to estimate the geometrical parameters of such a thick-walled sphere. In this model the outer radius was taken as $R_1 = R_h^{mean} = 96.4$ nm, $R_g = R_g^G = 88.8$ nm, and the inner radius R_2 calculated from the Equation (1):

$$R_g^2 = \frac{3}{5} \cdot \frac{R_1^5 - R_2^5}{R_1^3 - R_2^3} \tag{1}$$

was equal to 80.0 nm.

It should be taken into account that measuring of the molar mass and R_g of $(SiO_2)/(PEI\text{-}PAA)_{10}$ by light scattering methods is not a straightforward task due to the difference in the refractive indexes of the polymers [35]. In this respect, the measured value of R_g might be somewhat underestimated, meaning that the actual wall thickness of the sphere is smaller. Feng *et al.* [36] fabricated hollow microcapsules having shells of polyelectrolyte complexes by polymerization of 4-vinylpyridine hydrochloride (VPy) in a solution containing surface-modified silica particles and poly(sodium 4-styrenesulfonate) (NaPSS), and followed by a core removal with HF. The continuous shells with a thickness of 5–15 nm on the silica particles were created by covalent linking of the NaPSS-PVPy complexes.

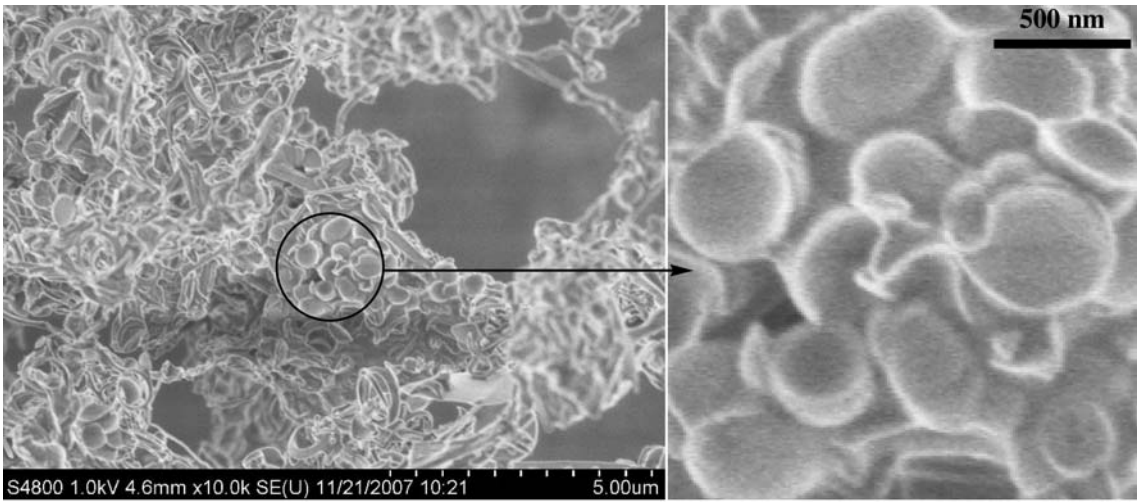

Figure 8. SEM picture of freeze-dried LbL particles of $(SiO_2)/(PEI\text{-}PAA)_{10}$. Arrow shows the enlarged area of circle

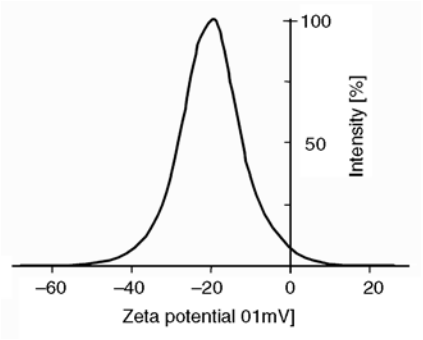

Figure 9. Zeta-potential measured for LbL of (SiO_2)/$(PEI\text{-}PAA)_{10}$ with C_p = 0.121 mg/ml

SEM picture of freeze-dried (SiO_2)/$(PEI\text{-}PAA)_{10}$ particles prepared from C_p = 12.1 mg/ml is depicted in Figure 8. In spite of the fact that during the freeze-drying process the ice crystals can damage the outer shells, the clones of ball-like particles are observed. The average size of such particles is in the range of 200–500 nm.

The zeta-potential of (SiO_2)/$(PEI\text{-}PAA)_{10}$ is shown in Figure 9. The mean peak value of the zeta-potential distributions fluctuates between –10 and –30 mV depending on the LbL concentration, which one could in principle be expected for salt-free aqueous solutions. The zeta-potential values and their sign agree well with the procedure of the complex preparation: the outer layer of the $(PEI\text{-}PAA)_{10}$ complex consists of PAA.

Microphotographs of thermally treated (SiO_2)/$(PEI\text{-}PAA)_{10}$ powder before and after etching of SiO_2 by HF are shown in Figure 10. Separate hollow spherical particles with different sizes and aggregated blob-like hollow particles bridged each other *via* hollow tubes are good seen. The mechanism of formation of LbL multilayers is probably multistage process (Figure 11). At first PEI chains may wrap one or several SiO_2 nanoparticles (Figure 11a). The added PAA chains are deposited onto SiO_2–PEI particles via electrostatic interactions (Figure 11b). Sequential adsorption of PEI and PAA to a single SiO_2 and/or aggregated SiO_2 nanoparticles can produce a spherical and/or cylindrical (SiO_2)/$(PEI\text{-}PAA)_{10}$ multilayers (Figure 11c, d). Here the dangled parts of PEI and PAA can participate in formation of IPEC particles and bridge the aggregated LbL particles (Figure 11d).

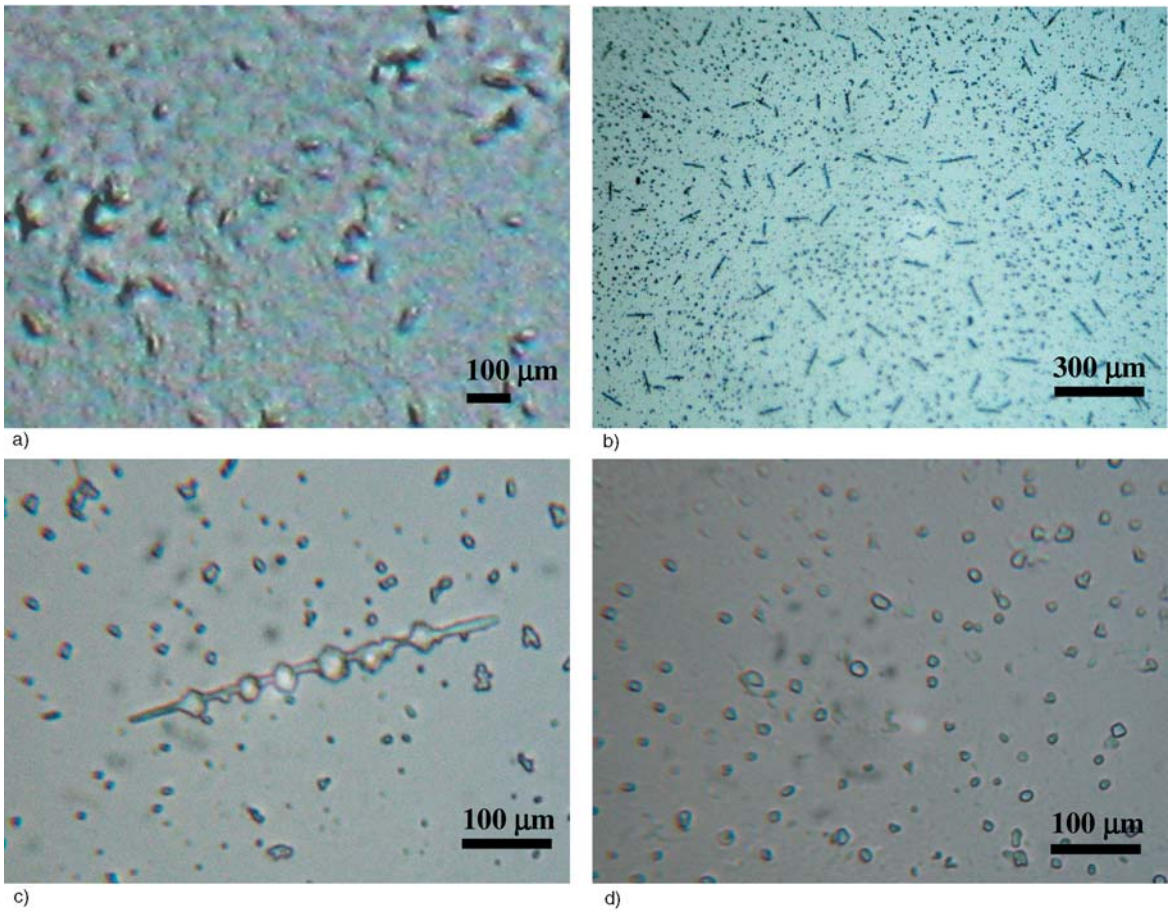

Figure 10. Microphotographs of (SiO_2)/$(PEI\text{-}PAA)_{10}$ after thermal treatment (a) and after etching by HF (b, c, d)

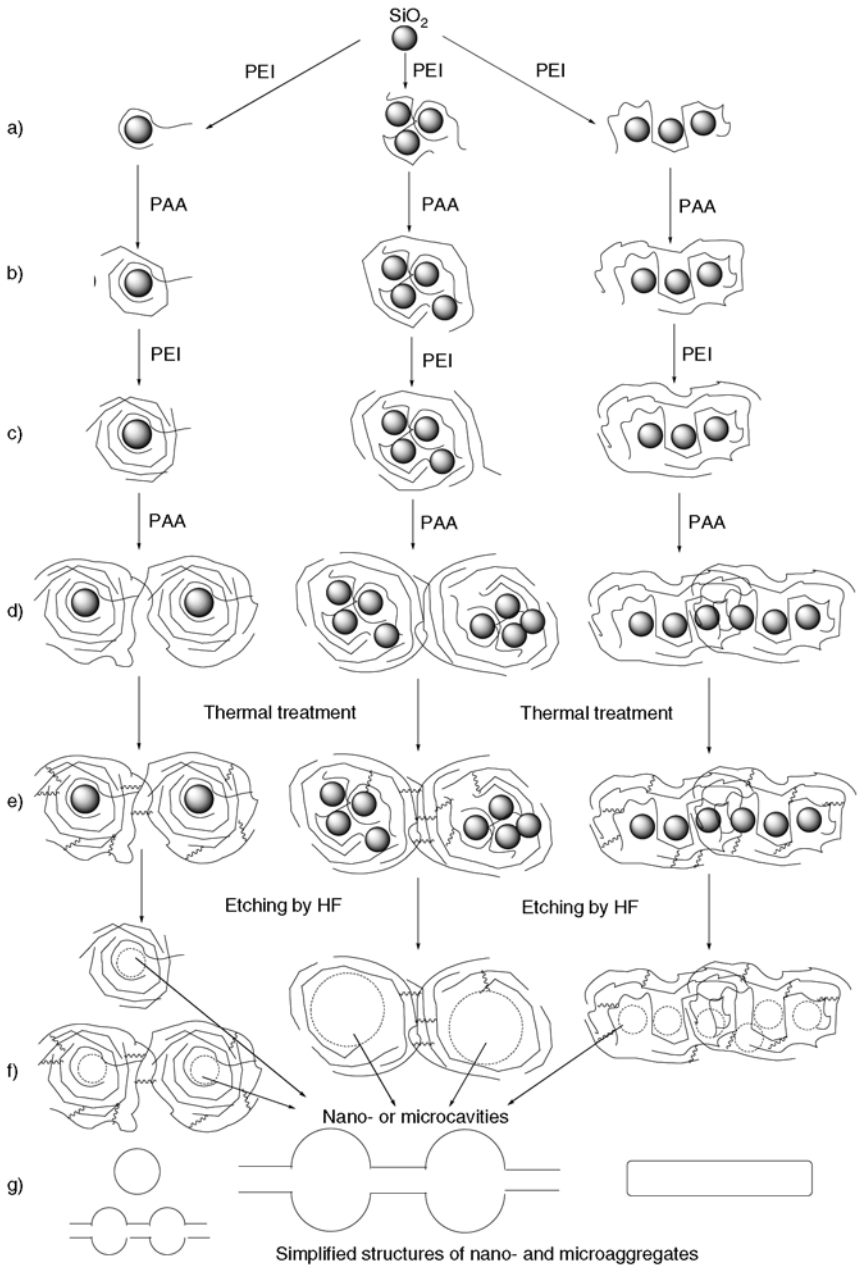

Figure 11. LbL multilayers assembled *via* interpolyelectrolyte reactions between silica sols and linear polyelectrolytes

The further thermal treatment of (SiO_2)/(PEI-PAA)$_{10}$ multilayers or aggregates converts the ionic bonds $–NH_3^+$ $^-OOC–$ on 'shell' layers to covalent amide bonds –NH–OC– analogous to amidization of PEI-PAA interpolyelectrolyte complexes (Figure 11e) [37]. Etching of SiO_2 'cores' from LbL multilayers leads to formation of nano- and microcavities, sizes of which corresponds to single or aggregated SiO_2 particles (Figure 11f). The simplified nano- and microparticles of (SiO_2)/(PEI-PAA)$_{10}$ can be represented as single or aggregated nanocavities, blob-like microparticles and even nano- and microturbes (Figure 11g). In the course of LbL multilayers the growth of a various combinations of nano- and microparticles leading to different nano- and microstructures are possible.

4. Conclusions

Nano- and microsized hybrid inorganic-organic composites were assembled between colloidal silica sols and synthetic polyelectrolytes as a result of interpolyelectrolyte reactions. The composition of precipitated interpolyelectrolyte complex (IPEC)

particles is mostly stoichiometric. Preparation of thin IPEC powders and composite films is demonstrated. Competition interpolyelectrolyte reactions between IPEC and strong polyelectrolytes, in particular polystyrenesulfonic acid (PSSA), can have technological importance for extraction and purification of SiO_2 nanoparticles. The probable mechanism of formation of 'layer-by-layer' (LbL) multilayers is suggested. The LbL technique followed by thermal treatment of IPEC and etching of silica nanoparticles with HF leads to formation of various kinds of nano- and microcavities.

Acknowledgements

Financial support from the Science Committee of the Ministry of Education and Science of the Republic of Kazakhstan (Contract No. 201) is greatly acknowledged. Authors thank Dr. M. Hahn from Fraunhofer Institute of Applied Polymers (Germany) for preparation of PDMDAAC microgel and PhD student M. Karesoja from Laboratory of Polymer Chemistry, Helsinki University (Finland) for SEM measurement.

References

[1] Mark J. E.: Some general trends in the area of organic-inorganic composites. In 'Hybrid Organic-Inorganic Composites' (eds.: Mark J. E., Lee C. Y-C., Bianconi P. A.) ACS Symposium Series, Washington, 1–4 (1995).

[2] Hay J. N., Shaw S. J.: Organic-inorganic hybrids – The best of both worlds? Europhysics News, **34**, 1–8 (2003).

[3] Saegusa T., Chujo Y.: Organic-inorganic polymer hybrids. Die Makromolekulare Chemie, Macromolecular Symposia, **64**, 1–9 (1992).

[4] Giannelis E. P.: Polymer layered silicate nanocomposites. Advanced Materials, **8**, 29–35 (1996).

[5] Giannelis E. P., Krishnamoorti R., Manias E.: Polymer-silicate nanocomposites: Model systems for confined polymers and polymer brushes. Advances in Polymer Science, **138**, 107–147 (1999).

[6] Kickelbick G.: Concepts for the incorporation of inorganic blocks into organic polymers on a nanoscale. Progress in Polymer Science, **28**, 83–114 (2003).

[7] Manne S., Aksay I. A.: Thin films and nanolaminates incorporating organic/inorganic interfaces. Current Opinion in Solid State and Material Science, **2**, 358–364 (1997).

[8] Harrup M. K., Wertsching A. K., Jones M. G.: Preparation and characterization of novel polymer/silicate nanocomposites. In: 'Functional Condensation Polymers' (eds.: Carraher C. E. Jr., Swift G. G.) Plenum Publishers, New York, 1–12 (2002).

[9] Cheng Y-J., Zhou S., Gutmann J. S.: Morphology transition in ultrathin titania films: From pores to lamellae. Macromolecular Rapid Communications, **28**, 1392–1396 (2007).

[10] Avvaru N. R., de Tacconi N. R., Rajeshwar K.: Compositional analysis of organic-inorganic semiconductor composites. Analyst, **123**, 113–116 (1998).

[11] Kurokawa Y., Sasaki M.: Complexation between polyions and hydrous inorganic oxides and adsorption properties of complex. Makromolekulare Chemie, **183**, 679–685 (1982).

[12] Brinker C. J., Scherer G. W.: Sol-gel science. Academic, New York (1990).

[13] Kasaikin V. A., Pavlova N. V., Zezin A. B., Kabanov V. A.: Flocculation and stabilization of colloid silica by linear polyelectrolytes is the result of cooperative reactions between complementary particles (in Russian). Doklady Academii Nauk SSSR, **281**, 888–892 (1985).

[14] Kasaikin V. A., Pavlova N. V., Ermakova L. N., Zezin A. B., Kabanov V. A.: Flocculation and stabilization of colloid silica by linear synthetic polyelectrolytes (in Russian). Journal of Colloids, **48**, 452–460 (1986).

[15] Ermakova L. N., Alexandrova T. A., Nuss P. V., Wasserman A. M., Kasaikin V. A., Zezin A. B., Kabanov V. A.: Conformation of ionic macromolecules adsorbed on the surface of polysilica acid sols (in Russian). Polymer Science, Series A, **27**, 1845–1851 (1985).

[16] Kalyuzhnaya R. I., Khulchaev Kh. Kh., Kasaikin V. A., Zezin A. B., Kabanov V. A.: Flocculation of polysilica acid sols by poly(dimethylaminoethylmethacrylate) (in Russian). Polymer Science, **36**, 257–263 (1994).

[17] Kabanov V. A.: Polyelectrolyte complexes in solution and condensed phase (in Russian). Russian Review in Chemistry, **74**, 3–20 (2005).

[18] Bixler H. J., Michaelis A. S.: Polyelectrolyte complexes. in 'Encyclopedia of Polymer Science and Technology' (eds.: Mark H. F., Gaylord N. G.) Interscience, New York, Vol. 10, 765–780 (1969).

[19] Tsuchida E., Abe K.: Interactions between macromolecules in solution and intermacromolecular complexes. Advances in Polymer Science, **45**, 1–119 (1982).

[20] Zezin A. B., Kabanov V. A.: Novel class of complex water-soluble polyelectrolytes (in Russian). Russian Review in Chemistry, **51**, 1447–1483 (1982).

[21] Bekturov E. A., Bimendina L. A.: Interpolymer complexes. Advances in Polymer Science, **41**, 99–148 (1981).

[22] Philipp B., Dautzenberg H., Linow K-J., Kötz J., Dawydoff W.: Polyelectrolyte complexes – recent developments and open problems. Progress in Polymer Science, **14**, 91–172 (1989).

[23] Ogawa K., Sato S., Kokufuta E.: Formation of intra- and inetrparticle polyelectrolyte complexes between cationic nanogel and strong polyanion. Langmuir, **21**, 4830–4836 (2005).

[24] Khutoryanskaya O. V., Williams A. C., Khutoryanskiy V. V.: pH-mediated interactions between poly(acrylic acid) and methylcellulose in the formation of ultrathin multilayered hydrogels and spherical nanoparticles. Macromolecules, **40**, 7707–7713 (2007).

[25] Donath E., Sukhrukov G., Caruso F., Davis S., Möhwald H.: Novel hollow polymer shells by colloid-templated assembly of polyelectrolytes. Angewandte Chemie, **37**, 2201–2205 (1998).

[26] Hornok V., Erdőhelyi A., Dékány I.: Preparation of ultrathin membranes by layer-by-layer deposition of layered double hydroxide (LDH) and polystyrene sulfonate (PSS). Colloid and Polymer Science, **283**, 1050–1055 (2005).

[27] Caruso F., Schüler C.: Enzyme multilayers on colloid particles: Assembly, stability, and enzymatic activity. Langmuir, **16**, 9595–9603 (2000).

[28] Kotov N. A., Dékány I., Fendler J. H.: Layer-by-layer self-assembly of polyelectrolyte-semiconductor nanoparticle composite films. Journal of Physical Chemistry, **99**, 13065–13069 (1995).

[29] Ai S., Lu G., He Q., Li J.: Highly flexible polyelectrolyte nanotubes. Journal of the American Chemical Society, **125**, 11140–11141 (2003).

[30] Martinez Y., Retuert J., Yazdani-Pedram M., Cölfen H.: Hybrid ternary organic-inorganic films based on interpolymer complexes of silica. Polymer, **45**, 3257–3265 (2004).

[31] Martinez Y., Retuert J., Yazdani-Pedram M., Cölfen H.: Transparent semiconductor-polymer hybrid films with tunable optical properties. Journal of Materials Chemistry, **17**, 1094–1101 (2007).

[32] Koetz J., Kosmella S.: Polyelectrolytes and nanopartciles. Springer Verlag, Berlin (2007).

[33] Su D. T.: Gels formed from anionic and cationic polymers. US Patent 4501834, USA (1985).

[34] Chu B.: Laser light scattering: Basic principles and practice. Dover Publications Inc., New York (2007).

[35] Kratochvil P.: Classical light scattering from polymer solution. Elsevier, Amsterdam (1987).

[36] Feng Z., Wang Z., Gao C., Shen J.: Hollow microcapsules with a complex polyelectrolyte shell structure fabricated by polymerization of 4-vinylpyridine in the presence of poly(sodium 4-styrenesulfonate) and silica particles. Materials Letters, **61**, 2560–2564 (2007).

[37] Rogacheva V. B., Grishina N. V., Zezin A. B., Kabanov V. A.: Intermacromolecular amidization in dilute aqueous solution of polyelectrolyte complex of polyacrylic acid and polyethylene imine (in Russian). Polymer Science, Series A, **25**, 1530–1535 (1983).

eXPRESS Polymer Letters Vol.2, No.2 (2008) 111–117
Available online at www.expresspolymlett.com
DOI: 10.3144/expresspolymlett.2008.15

Effect of mold temperature on short and long-term mechanical properties of PBT

*K. Banik**

Institute for Composite Materials (Institut für Verbundwerkstoffe GmbH), Technical University of Kaiserslautern, D-67663 Kaiserslautern, Germany

Received 11 September 2007; accepted in revised form 29 December 2007

Abstract. In this work, the effect of mold temperature variation on the short-term mechanical properties obtained from the tensile and Charpy impact tests, and the long-term mechanical properties obtained from dynamic mechanical loading and flexural creep of injection molded polybutylene terepthalate (PBT) are reported. It has been observed that the effect of changing the processing condition viz. mold temperature on the viscoelastic properties are more pronounced when their long-term behavior is tested. The tensile and impact properties showed only a negligible effect to the change in mold temperature. Further, analysis of the creep curves by applying a four-element Burger model presented a comprehensive understanding of their long-term viscoelastic behavior with respect to the change in mold temperature.

Keywords: *mechanical properties, mold temperature, polybutylene terepthalate, semicrystalline, molecular packing*

1. Introduction

With the increasing use of PBT in various engineering areas such as electrical, electronic, automotive, industrial and chemical sectors, a critical evaluation of the stress and deformation is needed to predict the reliability and failure behavior of such structures [1–4]. Material property determination is an important aspect of stress analysis. When compared to the conventional materials like steel, wood, etc., polymers exhibit lower strength and modulus. Their viscoelastic behavior reflects the combined effect of the viscous and elastic responses and determines the overall mechanical properties of the finished part. The deformation behavior of polymers is thus quite different from that of the elastic materials. The material response to the loading depends strongly on the timescale over which the perturbing force is applied, temperature and the speed at which they are deformed. This is exhibited in a set of processes like creep, stress relaxation rate or dynamical mechanical behaviour [5–9]. These are generally termed as long-term properties of a material and their testing time is considerably longer than the short-term tensile or impact tests. While accurate, creep has the obvious disadvantage of long test time, often years, and a large number of tests are required to characterize a material. The result is sparse data for polymers that is often difficult to compare and apply to design.

The viscoelastic properties of polymers are to a great extent depending on the thermomechanical history during processing. Generally, the commercial molding processes like injection molding, involve three extreme conditions – very high cooling rates, high pressure and shear and elongational flow while making a polymeric part. Thus the complex thermorheological situations that arise by varying the injection molding process parameters lead to different structural parameters like molecular orientation, residual stress, free volume and

*Corresponding author, e-mail: banik@hrz.tu-chemnitz.de

crystallinity (for a semicrystalline polymer) in the finished part varying along the flow direction as well as along the thickness direction. These can influence the viscoelastic properties of the molding significantly. An extensive review of the effect of processing and more specifically of thermal history on the properties of semicrystalline thermoplastics and its composites has been made by DePorter *et al.* [10].

This paper presents the results of a study of the effect of mold temperature on the short and long-term properties of injection molded PBT and demonstrates that the process-induced deformation behavior of the injection moldings can be better manifested when their long-term behavior is pursued.

2. Experimental

Unreinforced polybutylene terepthalate (Ultradur B 4500) used in this study was kindly supplied by BASF, Germany. Dumbbell-shaped tensile specimens of 4 mm thickness (Figure 1) were produced using Arburg Allrounder 320S (500–350) injection molding machine equipped with a mold temperature controller at three different mold temperatures, viz. 14, 40 and 60°C and are henceforth represented by PBT14, PBT40 and PBT60 respectively. All other processing parameters such as injection flow rate (20 cm^3/s), holding pressure (50 MPa) and holding time (15 s), rest cooling time (25 s), melt temperature (245°C) and pressure-to-switch over (40 MPa) were kept unaltered. Before injection molding, PBT granules were dried at 120°C for 3 hours.

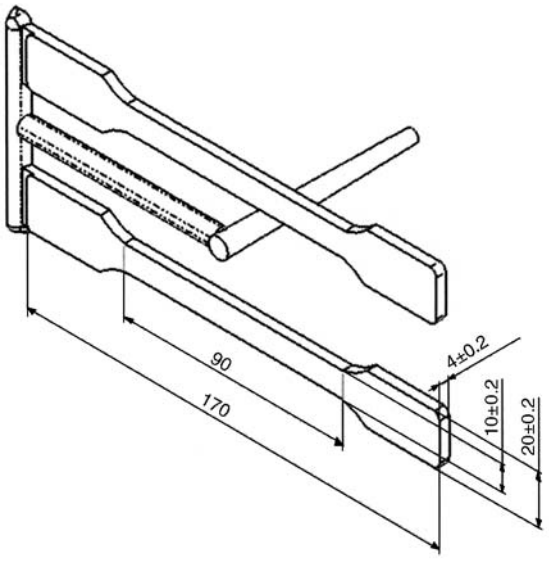

Figure 1. Schematic of the injection molded specimen (all dimensions are in mm)

Tensile tests were conducted according to DIN EN ISO 527 in a Zwick tensile testing machine. The deformation was measured by laser scanning technique using a cross-head speed of 5 mm/min. From these short-term tensile tests the characteristic values of tensile strength, elastic modulus and elongation at yield were determined and an average of five test specimens were reported.

Impact tests of the injection molded PBT were conducted in a CEAST impact tester. The notched Charpy impact strength was determined from 5 specimens of each type according to ISO 179.

Dynamic mechanical tests were performed on a DMA Q800 instrument (TA Instruments, USA) in a dual cantilever flexural mode. Specimen with dimensions of approximately 60×10×4 mm^3 (length × width × thickness) were used and the scannings were performed between 0–200°C at a heating rate of 3°C·min^{-1} at 1 Hz.

Flexural creep tests were performed using three-point bending mode at temperatures ranging from 30 to 80°C, in the same DMA Q800 apparatus. Isothermal tests were run on the specimens by increasing the temperature stepwise by 10°C. Prior to the creep measurement, the specimens were equilibrated for 5 min at each temperature and then the flexural creep behavior was tested for 15 min. All the tests were performed under a constant load of 7 MPa, which falls within the linear viscoelastic strain range determined by checking the proportionality condition [11, 12]. Test specimens of the same dimensions used for dynamic mechanical tests were employed for creep studies and the average of three statistically relevant creep and dynamic mechanical test data has been reported for each kind of specimen.

Differential scanning calorimetry (DSC) was done in a Netzsch 200 DSC instrument (Selb, Germany) to determine the crystallinity of the injection molded specimens. Calibrations were done using tin and all the scans were performed from 20 to 250°C at a heating rate of 20 K/min by constantly maintaining a nitrogen atmosphere inside the sample chamber. The amount of crystalline phase was determined by taking the ratio of the heat of fusion of the polymer against the heat of fusion for the 100% crystalline PBT assumed as 145 J/g [13]. In

order to determine the effect of thermomechanical history on the crystallinity content of the injection molded specimens, only the first heating scan was considered during thermal analysis.

The molecular packing (or the free volume) inside the injection molded parts was qualitatively characterized from the density measurements accomplished according to DIN 53479 (procedure A) at ambient temperature in a density measuring instrument provided by Sartorius AG (Goettingen, Germany). Ethanol was used for measuring the density of the samples. Then the specific volume was determined from the relation, specific volume, $v = 1/\rho$ where ρ is the density of the material. There exists a strong theoretical base relating the specific volume of polymers to the free volume available [5, 14, 15]. The advantage of density measurement is that it is comparatively simple and, depending upon the process also very small density variations can be dissolved.

3. Results and discussion

Figure 2 shows the DSC thermograms of PBT injection molded at three different mold temperatures. It shows that melting occurs between 227–228°C for PBT. An exotherm is observed around 210°C which can be identified as recrystallization followed by immediate melting [16]. An additional small exotherm (172–175°C) is also registered for PBT molded at 14°C ascribed to the melting of small and defective crystals. The DSC determined crystallinity was found to be 28.5, 30 and 31.1% for PBT processed at mold temperatures of 14, 40 and 60°C respectively. This is expected as during cooling from a higher melt temperature to a lower mold

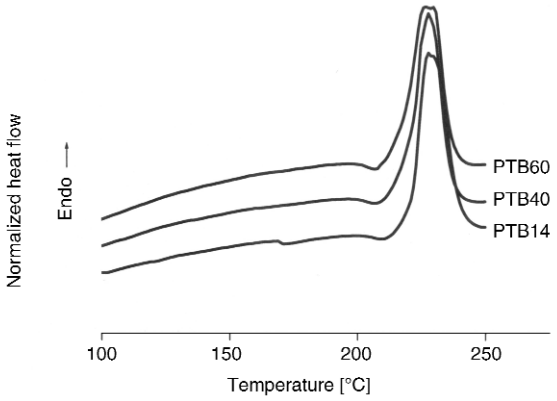

Figure 2. DSC thermograms of PBT injection molded at different mold temperatures

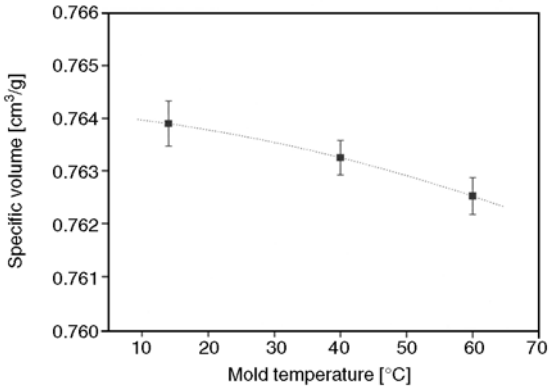

Figure 3. Influence of mold temperature on specific volume of injection molded PBT

temperature, the polymer passes through the crystallization temperature faster for a lower mold temperature than for a higher mold temperature, and so the polymer chains get less time to arrange themselves; contrariwise, slower cooling at higher mold temperature allows the macromolecules to adopt a more regular pattern. So they form bigger crystalline areas resulting in highly crystalline parts. Similar effect was also seen when the density measurements were accomplished. The specific volume was found to increase with the decrease in mold temperature due to the faster cooling at lower mold temperature that freezes-in higher free volume [5]. This has been shown in Figure 3, which clearly suggests higher molecular packing achievable with the PBT specimens processed at higher mold temperatures. Similar results have also been reported in the literature before [17].

Figure 4 shows the results of tensile tests of PBT produced by varying the mold temperature. It should be noted here that the stress-strain diagram of the PBT specimens (not shown here) exhibited a ductile fracture as the material showed yielding

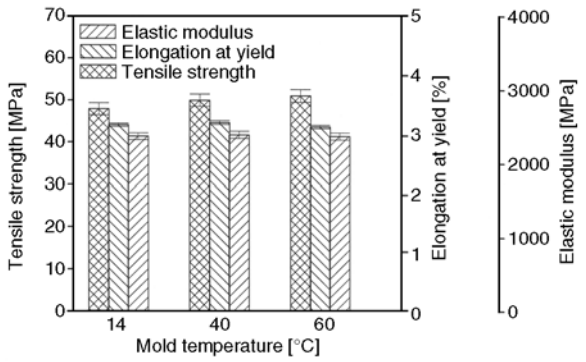

Figure 4. Short-term tensile properties of PBT processed at different mold temperatures

after which the stress remains fairly constant until it failed. However the results fail to show any significant effect of mold temperature variation on the tensile properties. The elastic modulus increased by only 2%, whereas the elongation at yield showed no remarkable effect when the mold temperature was raised from 14 to 60°C. Only the tensile strength showed an increase by 8% on raising the mold temperature. Similar results have also been reported before in the case of amorphous styrene-acrylonitrile (SAN) [18]. In the case of amorphous polymers, the deformation behavior depends to a large extent on the free volume or voids present inside the part. But for the semicrystalline polymers like PBT, the deformation process is quite complicated because of the presence of both amorphous and crystalline phases, and the semicrystalline morphology is so complicated that it is sometimes difficult to understand their effect on the deformation behavior as has been seen above. Generally, the short-term tensile tests are very common in practice for determining the mechanical properties of polymeric materials. During tensile testing, a large force acts over the cross-section of the injection molded part for a very short period of time, which is in fact much smaller in magnitude when compared to the average relaxation time of the polymer. So the effect of smaller change in the semicrystalline morphology or the molecular packing on the deformation process is weakly manifested unlike in creep, where the material deforms slowly with time. Hence the influence of mold temperature is little manifested in terms of tensile properties.

Similar effect can be seen from the results of the impact test. This is shown in Figure 5. It shows that with the increase in mold temperature from 14 to 40°C there is a little decrease in the impact strength, but no appreciable difference is observed when the mold temperature is changed from 40 to 60°C. This suggests that the deformation behavior of injection molded PBT is very complicated in the sense that sometimes it does not show any significant effect when the processing conditions are varied. Here we focused some of those results obtained for PBT processed at different mold temperatures.

The effect of mold temperature on the dynamic mechanical properties like storage modulus (E') and loss factor (tanδ) is shown in Figure 6. Figure 6a shows the plot of storage modulus as a function of temperature for PBT processed at three different mold temperatures. It shows that with the increase in mold temperature, storage modulus increases as a result of higher molecular packing when the mold temperature is raised. It also indicates that the storage modulus is significantly higher at lower temperatures corresponding to the higher stiffness in the glassy state and decreases with the increase in temperature as the stiffness is greatly reduced once the material passes the glass transition. However at higher temperatures PBT processed at different mold temperatures show similar stiffness. On the other hand, tanδ maxima decreased with the increase in the mold temperature (Figure 6b) indicating that the damping of the

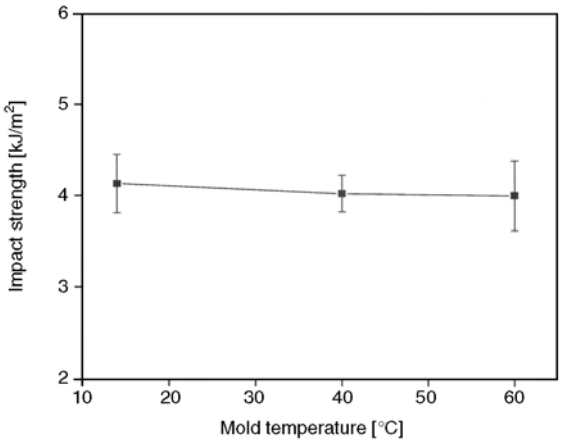

Figure 5. Results of impact test for PBT processed at different mold temperatures

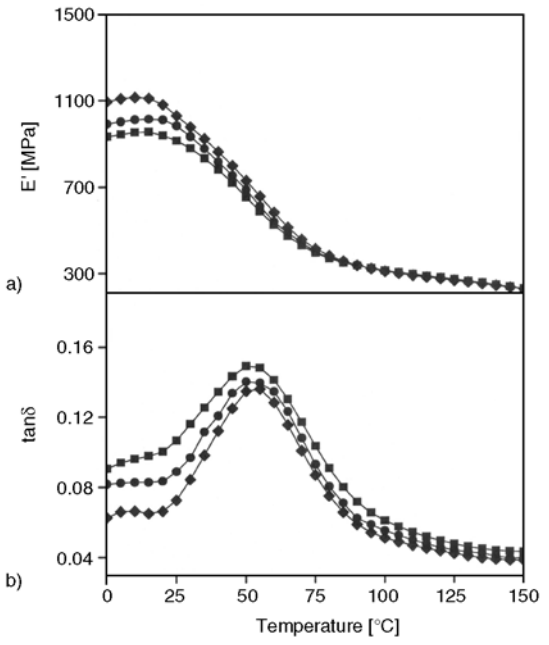

Figure 6. Effect of mold temperature on (a) dynamic storage modulus (E') and (b) tanδ of PBT.
(■ PBT14, ● PBT40, ♦ PBT60)

material increases when processed at lower mold temperature. The maximum tanδ value decreased by 10% (from 0.149 to 0.135) and the storage modulus at room temperature increased by about 13% (from 912 to 1028 MPa) when the mold temperature is increased from 14 to 60°C. Figure 6b further indicates that the glass transition temperature (temperature corresponding to the maxima in the tanδ vs. temperature plot) is slightly increased (about 2°C) as the mold temperature is raised. This is anticipated as processing at the higher mold temperature or slower cooling rate can lead to a closer packing of the molecular chains with more crystalline phase and less free volume. Hence more energy is required for the segmental mobility to occur.

The flexural creep behavior of PBT processed at different mold temperatures is shown in Figure 7 where the creep compliance is plotted as a function of time at room temperature (23 ± 1°C). The results show higher creep compliance for PBT processed at lower mold temperature indicating that an increase in the mold temperature tends to increase the creep resistance. The creep compliance at the end of the creep test thus showed an increase by about 9% when the mold temperature is decreased from 60 to 14°C. This indicates that the strain also increases by 9% during the creep test due to the decrease in mold temperature, which is hardly observed from the yield strain during tensile test. The difference in creep behavior arises from the difference in the thermal history (cooling rate) that the specimens experience while processing at different mold temperatures. A slower cooling rate at higher mold temperature tends to create more crystalline phase and less free volume that results in densely packed polymer chains and restricts the molecular mobility. This is manifested by lower compliance during the creep test. The observed creep behavior cannot be accomplished to the difference in frozen-in molecular orientation resulting from processing at different mold temperatures [17]. In comparison to the elastic modulus determined from the tensile tests, the variation in creep compliance is quite significant when the mold temperature is changed and can be much pronounced if the creep time is extended. But from the above results it is quite clear that even when the tensile tests do not exhibit any significant difference in terms of short-term mechanical properties on changing the mold temperature, but while considering their long-term behavior, they show a significant effect. Thus it can be suggested that the effect of varying the processing conditions can be better manifested when the long-term behavior of the molded part is tested. On the other hand, the problem of inadequate creep and dynamic data is especially acute for PBT with very little information available in the literature. Since these materials were specifically designed for precision moldings, knowledge of their time-dependent behavior is also essential.

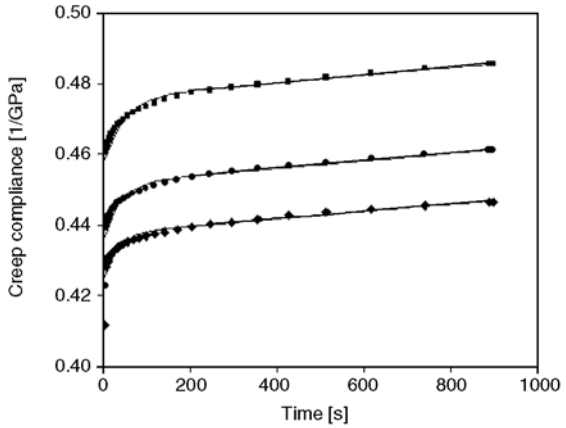

Figure 7. Dependence of creep compliance on the mold temperature of injection molded PBT at room temperature (■ PBT14, • PBT40, ♦ PBT60); solid lines indicate the Burger fit

Besides experimental observation, highly developed creep modeling can also be applied to PBT processed at different mold temperatures to develop comprehensive understanding of the creep deformation. In the past half-century, numerous creep models [11, 19–21] have been proposed and applied to describe the creep behavior of viscoelastic materials. Various materials of the same geometry may respond differently under identical external effects. Such differences in response are often attributed to the inherent constitution of the materials. Burger model is a series of combinations of Maxwell and Kelvin-Voigt models (Figure 8) and has been discussed in details in the literatures [22, 23]. According to this model, the total strain is given by the Equations (1) and (2):

$$\varepsilon = \varepsilon_1 + \varepsilon_2 + \varepsilon_3 \tag{1}$$

$$\frac{\varepsilon}{\sigma} = \frac{1}{E_1} + \frac{1}{E_2}\left[1 - \exp\left(-\frac{tE_2}{\eta_2}\right)\right] + \frac{t}{\eta_1} \tag{2}$$

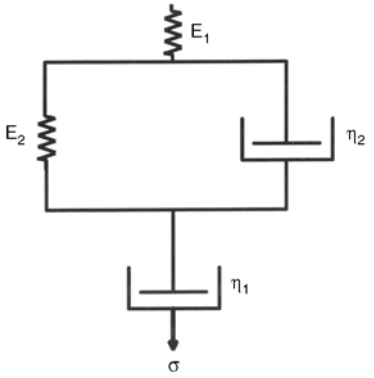

Figure 8. Schematic of the four-element Burger model

where ε_1 and ε_2 are the elastic and viscous strain represented by the Maxwell model and ε_3 is the viscoelastic strain represented by Kelvin-Voigt model, E_1 and E_2 are the elastic moduli, η_1 and η_2 represent the viscosity of the material, σ is the applied stress and t is the creep time.

The experimental and model plots are shown in Figure 7 for PBT processed at the mold temperatures of 14, 40 and 60°C. The first instantaneous deformation arises from the spring or the elastic element (E_1) and later time dependent deformation comes from the parallel spring and dashpot (η_2) and from the viscous dashpot flow (η_1). The model parameters E_1, E_2, η_1 and η_2 can be obtained by non-linear fitting of the experimental data and are shown in Table 1 for the PBT processed at different mold temperatures. According to this model, the modulus (E_1) of the Maxwell spring increases with the increase in the mold temperature, which can be attributed to the stiffening of the material when PBT is processed at higher mold temperature. The retardant elasticity (E_2) however showed a decrease with the increase in mold temperature. On the other hand, viscosity decreased with the decrease in the mold temperature as higher flow occurred in the spring and dashpot and permanent deformation increased. These can be correlated to the microstructure developed in the molded parts, i.e., higher crystallinity as well as molecular packing in the specimens processed at higher mold temperature of 60°C is expected to show up with an increase in the elastic modulus and viscosity that is manifested during the creep test with reduced tendency to creep. Thus the modeling parameters provide a comprehensive understanding of the creep of injection molded PBT and also provide a possible explanation of the internal structure to the viscoelastic property relationship with respect to the change in the mold temperature. Note that the effect of other processing conditions like melt temperature, flow rate and holding pressure on the creep behavior of injection molded PBT have also been studied before, but the results showed that they have only a very little effect on the long-term viscoelastic properties [17] and are hence not discussed in the present study.

Table 1. Parameters obtained from Burger model

Sample	E_1 [GPa]	E_2 [GPa]	η_1 [GPa·min]	η_2 [GPa·min]
PBT14	2.19	31.30	333.33	3.34
PBT40	2.30	27.73	362.32	3.64
PBT60	2.36	25.71	438.60	3.73

4. Conclusions

The effect of mold temperature variation on the short and long-term behavior of injection molded PBT were presented. The results indicated that the influence of mold temperature variation is little manifested from the tensile and impact properties of the molded PBT parts, but while considering their creep and dynamic mechanical behavior, they show a significant effect. This deformation behavior could be explained by the influence of processing conditions on the semicrystalline morphology, particularly crystallinity as well as molecular packing density of the molded PBT parts. Moreover, the modeling results provided a comprehensive understanding of the creep behavior. The parameter analysis based on the Burger model provided a possible explanation to the decrease in the creep response on increasing the mold temperature. The long-term properties thus showed more sensitivity to the internal structure than the short-term properties as the characteristic time is of the order of the molecular time. Hence it is suggested that the effect of processing conditions can be better characterized when the long-term mechanical properties of the molded parts are pursued.

Acknowledgements

A part of this work was conducted in the framework of a research project supported by the German Research Foundation (DFG Me 563/34-1/2). The author is grateful to Prof. Günter Mennig of Chemnitz University of Technology, Germany, for his invaluable suggestions during this study.

References

[1] Fakirov S.: Handbook of thermoplastic polyesters. Wiley-VCH, Weinheim (2002).

[2] Shibaya M., Ishihara H., Yamashita K., Yoshihara N., Nonomura C.: Effect of mold temperature on structure and property of PBT injection moldings in the thickness direction. International Polymer Processing, **XIX**, 303–307 (2004).

[3] Hashemi S.: Temperature dependence of work of fracture parameters in polybutylene terephthalate (PBT). Polymer Engineering and Science, **40**, 1435–1446 (2000).

[4] Hashemi S.: Deformation rate dependence of work of fracture parameters in polybutylene terephthalate (PBT). Polymer Engineering and Science, **40**, 132–138 (2000).

[5] Struik L. C. E.: Physical ageing in amorphous polymers and other materials. Elsevier, Amsterdam (1978).

[6] Crawford R. J.: Plastics engineering. Pergamon Press, Oxford (1987).

[7] Osswald T. A., Menges G.: Materials science of polymers for engineers. Hanser, Munich (1996).

[8] Pegoretti A., Gorigato A., Penati A.: Tensile mechanical response of polyethylene- clay nanocomposites. Express Polymer Letters, **1**, 123–131 (2007).

[9] Nagy P., Vas L. M.: Relationship between constant strain rates and stress relaxation behavior of polypropylene. Express Polymer Letters, **1**, 84–91 (2007).

[10] DePorter J. K., Baird D. G., Wilkes G. L.: The effects of thermal history on the properties of semicrystalline thermoplastic composites: A review of experimental and numerical investigations. Journal of Macromolecular Science, Part C: Reviews in Macromolecular Chemistry and Physics, **33**, 1–79 (1993).

[11] Findley W. N., Lai J. S., Onaran K.: Creep and relaxation of nonlinear viscoelastic materials. North-Holland Publishing Company, Toronto (1976).

[12] Nuñez A. J., Marcovich N. E., Aranguren M. I.: Analysis of the creep behavior of polypropylene-woodflour composites. Polymer Engineering and Science, **44**, 1594–1603 (2004).

[13] Moneke M.: Die Kristallisation von verstärkten Thermoplasten während der schnellen Abkühlung und unter Druck. Ph.D Thesis, Technische Universität Darmstadt, Germany (2001).

[14] Struik L. C. E.: Physical aging: Influence on the deformation behavior of amorphous polymers. in 'Failure of Plastics' (eds.: Brostow W., Corneliussen R. D.) Hanser, München 209–234 (1986).

[15] Engelsing K.: Einfluß des freien Volumens auf das verarbeitungsabhängige Deformationsverhalten spritzgegossener amorpher Thermoplaste. Ph.D Thesis, Technische Universität Chemnitz, Germany (2000).

[16] Di Lorenzo M. L., Righetti M. C.: Morphological analysis of poly(butylene terepthalate) spherulites during fusion. Polymer Bulletin, **53**, 53–62 (2004).

[17] Banik K., Mennig G.: Process-induced long-term deformation behavior of semicrystalline PBT. Polymer Engineering and Science, **46**, 882–888 (2006).

[18] Engelsing K., Mennig G.: Influence of the injection molding process on the free volume and its effect on the creep behavior of styrene-acronitrile copolymer. Mechanics of Time-Dependent Materials, **5**, 27–38 (2001).

[19] Ward I. M.: An introduction to the mechanical properties of solid polymers. John Wiley and Sons, West Sussex (1993).

[20] Kolarík J., Pegoretti A.: Non-linear tensile creep of polypropylene: Time-strain superposition and creep prediction. Polymer, **47**, 346–356 (2006).

[21] Betten J.: Creep mechanics. Springer, Berlin (2005).

[22] Menard K. P.: Dynamic mechanical analysis. CRC Press, Florida (1991).

[23] Houshyar S., Shanks R. A., Hodzic A.: Tensile creep behaviour of polypropylene fibre reinforced polypropylene composites. Polymer Testing, **24**, 257–264 (2005).

eXPRESS Polymer Letters Vol.2, No.2 (2008) 118–125
Available online at www.expresspolymlett.com
DOI: 10.3144/expresspolymlett.2008.16

Mechanical and dielectric properties of epoxy/dicyclopentadiene bisphenol cyanate ester/glass fabric composites

J. H. Wang, G. Z. Liang, H. X. Yan, S. B. He*

Department of Applied Chemistry, School of Science, Northwestern Polytechnical University, Xi'an Shaanxi 710072, China

Received 2 December 2007; accepted in revised form 29 December 2007

Abstract. The impact and flexural strengths of epoxy-dicyclopentadiene bisphenol cyanate ester (EP-DCPDCE) hybrid thermoset as well as the interlaminar shear strength (ILSS) and flexural strength of the composites consisting of the hybrid thermoset and glass fabric were studied. It is found that the addition of epoxy resin (EP-51) can improve the mechanical properties, particularly, the impact strength of DCPDCE matrix and the ILSS of glass fabric reinforced composites. The improvements of the mechanical properties were obvious when the content of EP-51 is from 15 to 30 wt%. The investigations of the interphase of composites by scanning electron microscope (SEM) and dynamic mechanical analysis (DMA) confirm the improvement of mechanical properties of the composites. However the addition of EP-51 has negative effects on the thermal and dielectric property of the composites.

Keywords: *polymer composites, cyanate ester, mechanical properties, interphase*

1. Introduction

The necessity of developing high speed computers has led to the exploration of new materials which can expend the electrical and mechanical performance limits of the presently available technology [1–4]. In the microelectronics industry low permittivity and dissipation factor, good mechanical and thermal properties are required for intermetal dielectrics, especially in printed circuit board (PCB) industry [5].

Polycyanurates are interesting polymers for low constant and dissipation dielectrics [6–8]. In the curing reaction three cyanate ester functional groups (–OCN groups) form a triazine ring (trimerization). Due to the high degree of symmetry in the triazine ring, where dipoles associated with the carbon-nitrogen and carbon-oxygen bonds are counterbalanced, polycyanurates have low relative permittivity in general (e.g., $\varepsilon < 3.2$ for trifunctional homopolymer networks) [9]. Dicyclopentadiene (DCPD) is a raw material for low dielectric polymers due to its low polarity and low moisture absorption. This hydrophobic nonpolar bridging group contributes to excellent moisture resistance and a dramatic reduction in the permittivity without determinately affecting thermal performance [10]. Dicyclopentadiene bisphenol cyanate ester (DCPDCE) introduces the DCPD structure into the backbone of bisphenol A cyanate ester. For the cured resin of DCPDCE, the cycloaliphatic character in the structure is effective in reducing permittivity and moisture absorption while the aromatic character maintains a high T_g [11]. It is a potential dielectric matrix for composites. But like other

*Corresponding author, e-mail: lgzheng@nwpu.edu.cn

cyanate esters, DCPDCE has high cross linkage which makes it fragile and limits its usage in some cases requiring good mechanical properties [12–14]. In this work, we used epoxy resin to modify DCPDCE and analyzed the influence of epoxy resin on the mechanical properties of neat resin and glass fabric reinforced composites.

2. Experimental

2.1. Materials

DCPDCE, containing 25% weigh fraction of butanone, was purchased from Shangyu Shengda Biochemical Company, Ltd. (located in Zhejiang, China), with a brand name of SD-3 and cyanate equivalent 215. Epoxy resin (EP-51) was provided by Xi'an Resin Company, Ltd. (located in Shaanxi, China), with the epoxy equivalent weight of 196. E-glass fabric (areal density: 210 ± 20 g/m^2, weave style: plain, yarn density: 2.55 g/cm^3) with a trademark of EW210 was supplied by Nanjing Fiber Co., (located in Nanjing China). Figure 1 gives the chemical structures of DCPDCE and EP-51.

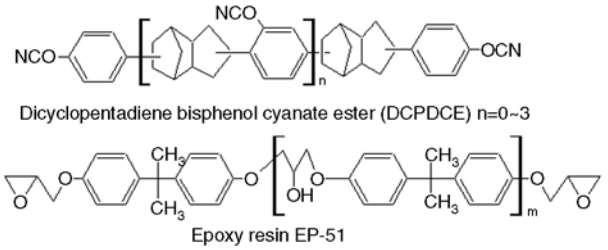

Figure 1. The chemical structures of DCPDCE and EP-51

2.2. Preparation of cured neat resin and glass fabric composite

The butanone in the DCPDCE was removed under vacuum at 80°C through distillation to obtain pure DCPDCE which was mixed with EP-51. The mixture was agitated about 5 min at 140°C until EP-51 and DCPDCE became homogeneous. The homogeneous mixture was poured into a pre-heated mould (150°C) with release agent on the inner walls, and then, the mould was degassed under vacuum for 25 min at 140°C, followed by the curing cycle and post-curing cycles:

Curing cycle: 170°C/2 h + 180°C/1 h + 200°C/1 h

Post-curing cycle: 220°C/2 h

Proper amount of EP-51 and about the same weight of solvent of acetone were added into the DCPDCE solution of butanone, and the mixture was agitated for about 5 min until they became homogeneous. The composites were fabricated by a hand lay up technique as follows: the above homogeneous mixture was painted on glass fabric (pre-dried at 200°C for 30 min before used) with brush, and the resulted prepreg was hung up at room temperature for at last 24 h to remove the solvents of acetone and butanone mostly. After that, the prepreg was cut to pieces of 300 mm×300 mm, and 14 sheets of cut prepreg were piled onto the mould. The prepreg in the mould was degassed under vacuum at 140°C for 30 min to remove the remained solvents and the trapped air, and then, the mould loaded with the prepreg was put into a machine which can provide pressure and heat at the same time. The mould was heated to 160°C at the rate of 2°C/min under contact pressure. Before gelation, while some silk could be drawn from the resin, a pressure of 0.7 MPa was applied for 15 min, and when the resin gelled, a pressure of 1.5 MPa was applied and maintained through the following process of 180°C/1 h + 200°C/1 h + 220°C/2 h. The pressure was released until the mould cooled to room temperature sponteneously. Some related parameters of the laminated boards are showed in Table 1.

2.3. Test methods and equipments

The flexural strength and impact strength of cured neat resin were measured according to GB2570-81 standard (resembling ASTM D 790-03, rectangular specimen: 80 mm×15 mm×4 mm, span/depth = 16) and GB2571-81 standard (resembling ASTM D

Table 1. Some related parameters of the laminated boards

Content of EP-51 [wt%]	Resin content [wt%]	Density of composites [g/cm^3]	Density of fiber [g/cm^3]	Fabric content [%volume]
0	37.6	1.75	2.55	42.8
5	41.2	1.68	2.55	38.7
15	37.1	1.73	2.55	42.7
30	38.7	1.71	2.55	41.1
50	40.3	1.70	2.55	39.8

256-97, rectangular specimen: 15 mm×10 mm× 4 mm, unnotched) of China, respectively. The flexural strength and the interlaminar shear strengths (ILSS) of the glass fabric reinforced composite were measured according to GB/T1449-83 standard (resembling ASTM D 790-03, rectangular specimen: 60 mm×15 mm×2.5 mm, span/depth = 16), and GB/T3357-82 standard (resembling ASTM D 2344, rectangular specimen: 20 mm× 6 mm×2.5 mm, span/depth = 5) of China, respectively. The content of resin and the content of glass fabric in composites were measured according to GB/T2577-05 standard of China.

Dynamic mechanical analysis (DMA) of the composite was performed with a TA Instrument (DMA Q800) at a frequency of 3 Hz and a heating rate of 3°C/min, and the testing mode was single cantilever. The morphology of the fracture of cured neat resins and composites was investigated by a scanning electron microscope (SEM, Quanta 200, FEI), scanning voltage was 15 kV. The permittivity and dissipation factor were tested on AS2853 impedance analyzer at 25°C.

3. Results and discussions

3.1. The mechanical properties of cured resins

Flexural strength and impact strength of various cured neat resins are represented in Figure 2. The curves of flexural strength and impact strength versus the content of EP-51 show approximately the same trend with the increase of EP-51 weight fraction. The flexural strength increased from 96.2 MPa of the pure DCPDCE resin to the peak at 120.3 MPa at 15 wt% of EP-51, increasing by 25%, and the

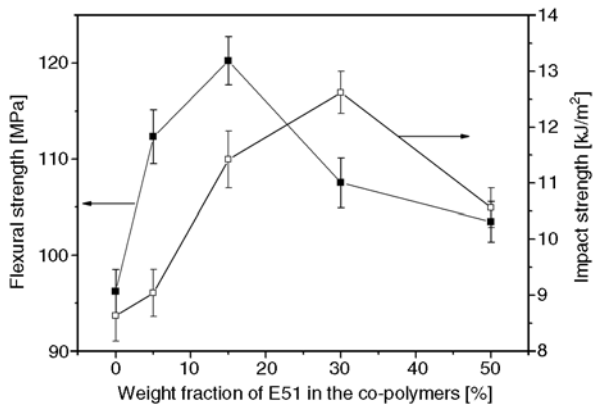

Figure 2. Flexural and impact strengths of various EP-51/DCPDCE hybrid thermosets

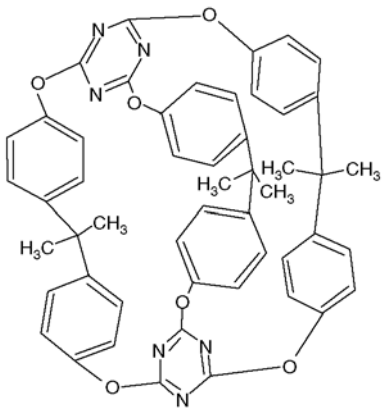

Figure 3. The cage compounds

impact strength increased from 8.63 kJ/m^2 of the pure DCPDCE resin to the maximum value of 12.62 kJ/m^2 at 30 wt% of EP-51, increasing by 46%. These results are explained as follows: firstly, the trimerization of pure cyanate ester results in high crosslink density of cyanurate network. Secondly, the presence of some non-network-buinding cage compounds (Figure 3) in cured cyanate ester resin and the decyanation of them contribute to defects in the cured resin [15, 16]. Both the high crosslink density and the defects weaken the mechanical properties of self-polymerized DCPDCE resin. The addition of EP-51 could reduce the crosslink density and repair the defects through co-reaction with DCPDCE (Figure 4) [17], which improve the mechanical properties of cured DCPDCE resin. However, the oxazolidinone rings forming in the co-reaction have lower mechanical properties than traizine rings, which make the mechanical properties drop from the maximum values. Figure 5 gives the morphology of fracture surface of impact samples. An obviously brittle fracture is shown for the pure DCPDCE resin (Figure 5a). On contrast, when the content of EP-51 is 30 wt%, there are a lot of tough whorls which indicate a tough fracture (Figure 5b). These SEM micrographs prove the above analysis of the mechanical properties partially.

Figure 6 shows the storage moduli of neat cured resins. It indicates that when the content of EP-51 is 30 or 15 wt% the glassy storage modulus of the cured resin is higher than that of the pure DCPDCE resin. While when the temperature increases, the higher the content of EP-51 is, the faster the storage modulus decreases, which confirms the reduction

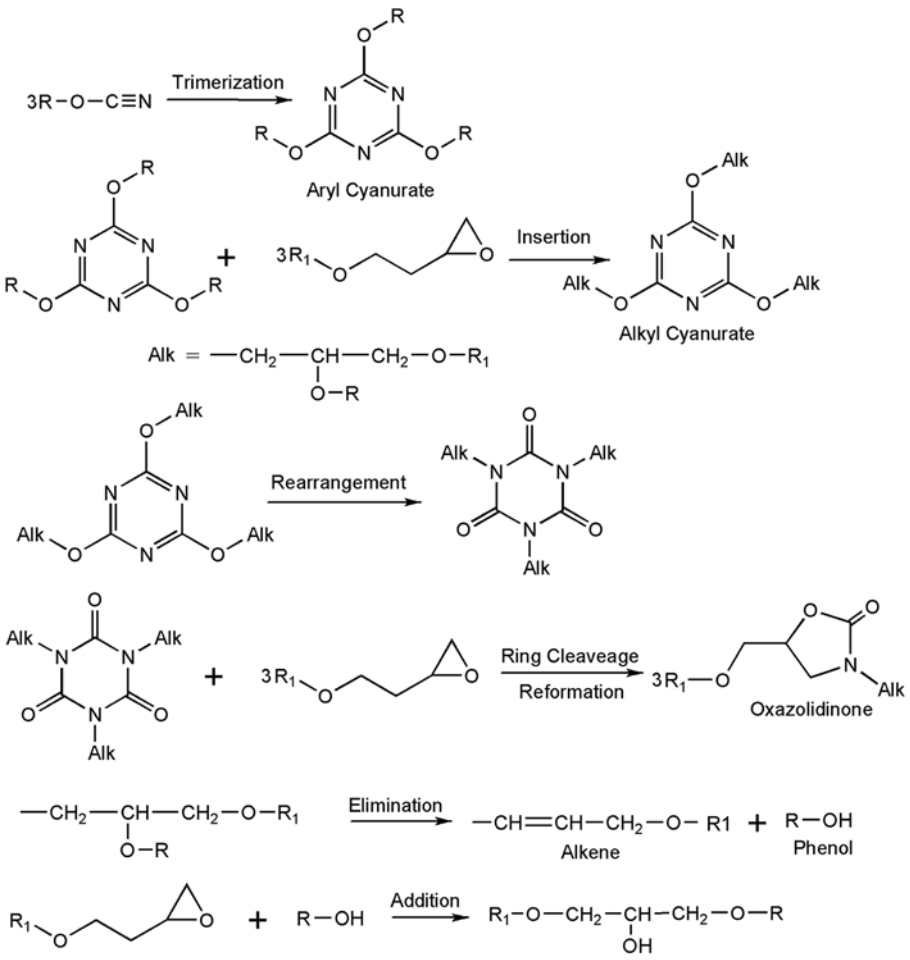

Figure 4. Reaction scheme for the co-reaction of cyanates with epoxies

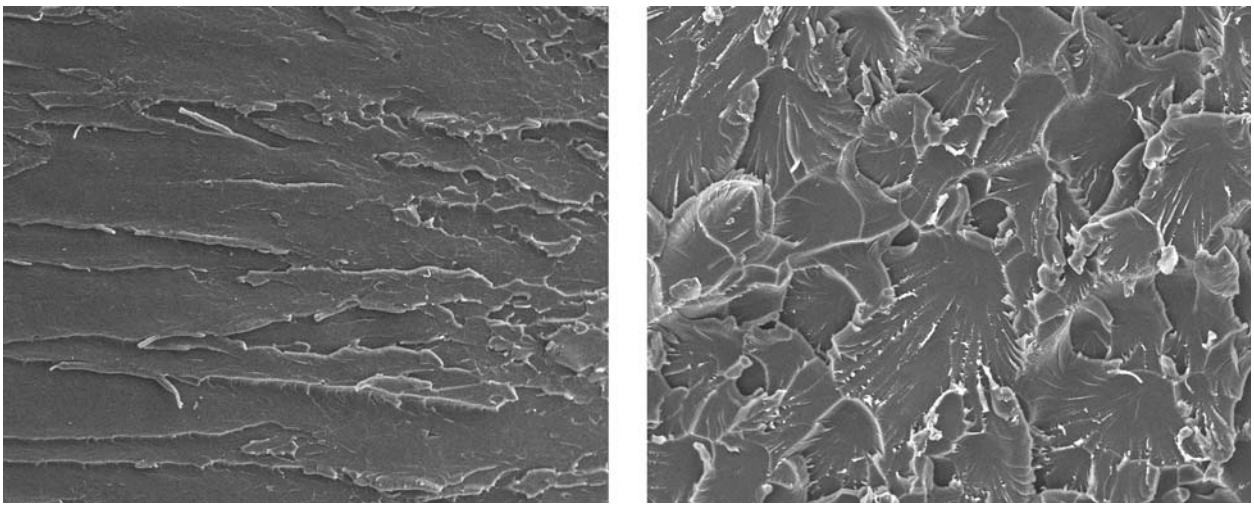

Figure 5. The morphology of the fracture surface of impact samples: (a) Pure DCPDCE, (b) EP-51/DCPDCE (30/70 by weight) hybrid thermoset

of the crosslink density in EP-DCPDCE hybrid thermoset.

3.2. The mechanical properties of glass fabric reinforced composites

ILSS mainly depends on the interfacial adhesion between fibers and matrix. If the adhesion between

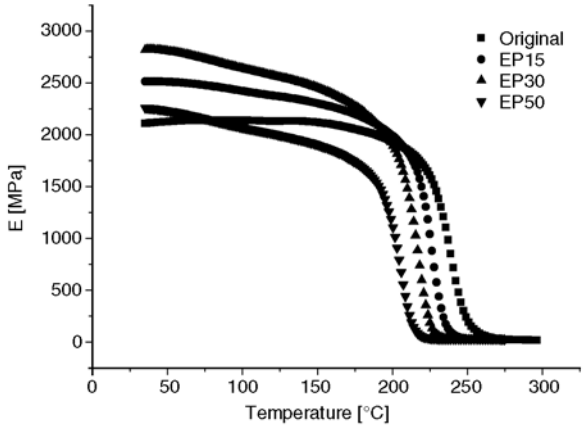

Figure 6. The storage modulus of neat resin

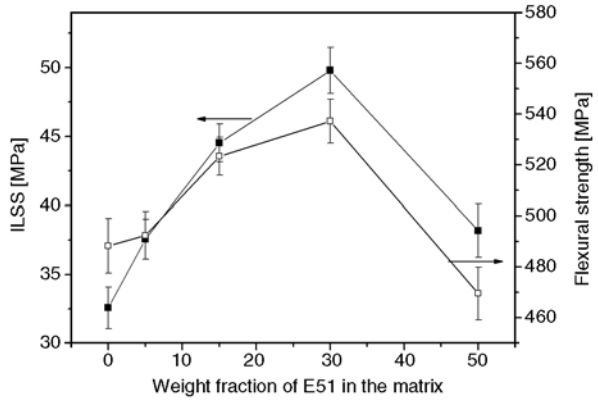

Figure 7. ILSS and flexural strength of glass fabric reinforced composites

fibers and matrix is strong enough, the mechanical property of the matrix has also influence on ILSS. Figure 7 shows the ILSS and flexural strength of the glass fabric reinforced composites versus EP-51 content in the matrix. At first, the ILSS increased with the content of EP-51 and when the content of EP-51 was 30 wt% the ILSS reached its maximum value, after that, the ILSS dropped from the maximum. These changes have their reasons. When DCPDCE cures, the –OCN groups take part in the trimerization reaction to form trimerization structure with very high crosslink density. The fragile nature of the trimerzation structure will result in premature failure in the interphase of the composites. When epoxy resin is added, the EP-51 can react with the triazine ring to form oxazolidinone structure which has higher polarity than trizaine ring and more probability to react and/or interact with glass fibers. Moreover, the decrease of the crosslink density improves the toughness of the matrix, which can release the residual strain forming in the processing of composite and stop microcrack propagating more effectively. All these effects reinforce the interfacial adhesion between the matrix and glass fibers, resulting in the increase of ILSS by 48%, from 32.6 to 48.2 MPa. Meanwhile the reason of the value of ILSS dropping from the maximum when the content of EP-51 is 50 wt% is not very clear. We surmise that the preferential adsorption of glass fibers to EP-51 makes the content of EP-51 in the interphase bigger than that in the bulk matrix and some EP-51 in the interphase can not cure completely under this curing cycle, which weakens the mechanical property of the interphase and reduces the value of ILSS.

Figure 7 also shows that the curve of flexural strength of the composites versus EP-51 content has similar trend with that of ILSS. It indicates that the stronger interfacial adhesion improves the transfer of load from matrix to fibers, consequently, enhancing the flexural strength of the composites.

3.3. The SEM analyses of the composites

The SEM micrograph of the fracture surface of samples after short-beam shear test can directly show whether the interfacial adhesion between the matrix and the fibers is good or not. Figure 8 gives the SEM micrographs of the fracture surface after short-beam shear test. Figure 8a is the micrograph of the original DCPDCE/glass fabric composite, and Figure 8b is the composite which has 30 wt% of EP-51 in the matrix. In Figure 8a, the fiber surface of the fracture samples is smooth and little resin adheres on the fibers, which indicates weak interfacial adhesion between the resin and the fibers. In contrast, an obvious resin coat covers the fibers tightly for the Epoxy/DCPDCE/glass fabric composite in Figure 8b. This resin coat illustrates that the fracture happens in the matrix instead of on the surface of fibers.

3.4. Dynamic mechanical analysis of the composites

Among numerous techniques for interface characterization, DMA has attracted ever more attention because it provides a sensitive and nondestructive detection of the interphase [18–20]. DMA detects the molecular motions through measuring two types of response to a low strain periodic deformation, an elastic (stiffness) term and a damping

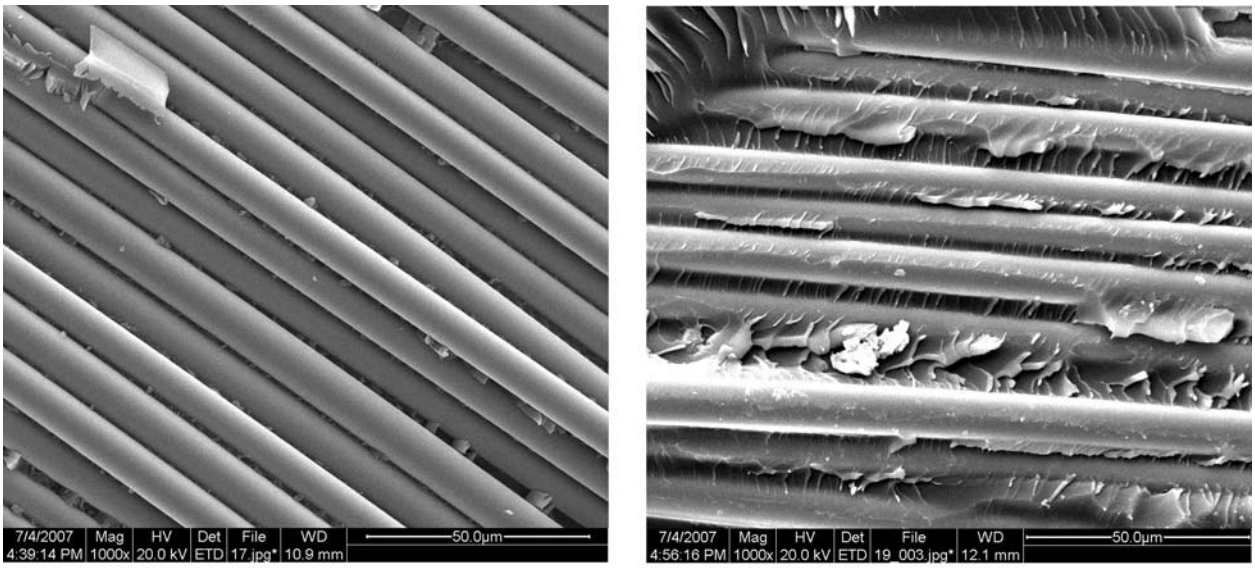

Figure 8. The SEM micrograph of the fracture surface of samples after short beam shear test: (a) Pure DCPDCE/glass fabric composite; (b) EP-51/DCPDCE (30/70 by weight)/glass fabric composite

Table 2. The values of relative parameters and the calculated parameter B

System	$\tan\delta_m$	$\tan\delta_c$	ϕ_f	ILSS	B
F/EP0/DCPDCE	0.761	0.285	0.428	32.57	1.46
F/EP15/DCPDCE	0.888	0.275	0.427	44.52	1.61
F/EP30/DCPDCE	0.879	0.239	0.411	49.80	1.77
F/EP50/DCPDCE	0.738	0.296	0.398	38.17	1.50

(energy dissipation) term, and the damping is a sensitive indicator of all kinds of molecular motions that are going on in a material. In composite, the molecular motions at the interphase contribute to the damping of the material. In summary, the damping of a composite depends greatly on the interfacial interactions. So we employed DMA and a parameter proposed by former researchers to investigate the interphase further.

The parameter *B* which was first introduced by Ziegel is described by Equation (1):

$$\tan\delta_c = (1 - B\phi_f)\cdot\tan\delta_m \quad (1)$$

The stronger the interfacial interaction is, the higher the value of parameter *B* [21]. Among many research works, parameter *B* which corrects the volume fraction of reinforcement because of the formation of a layer of immobilized interphase resulting from strong interactions at the interface is the particularly worth mentioning one conducted by Dong and Gauvin [22]. Therefore, we chose the parameter *B* to evaluate the interfacial adhesion between the fibers and matrix.

Table 2 gives the values of some relative parameters and the parameter *B* of the composites, in which *F* refers to fabric and EP_i stands for the matrix has *i* wt% of EP-51. A good relationship between the parameter *B* and the ILSS of the composite is found, that is, the higher parameter *B* is, the higher ILSS of composites will be.

Figure 9 shows the curves of DMA of the composites. From Figure 9a, we can see that the composites containing 30 wt% of EP-51 in the matrix has a higher storage modulus since the improvement of interfacial adhesion, while the thermal stabilities of the composites containing EP-51 decline for the poorer thermal property of oxazolidinone structure in the matrix.

3.5. The dielectric property of the composites

In order to understand the influence of epoxy resin on the dielectric property of the composites, the permittivity and dissipation factor of the composites were investigated. Figure 10a gives the changing of the permittivity and dissipation factor versus content of EP-51. It indicates that the addition of EP-51 has negative effect on the dielectric property

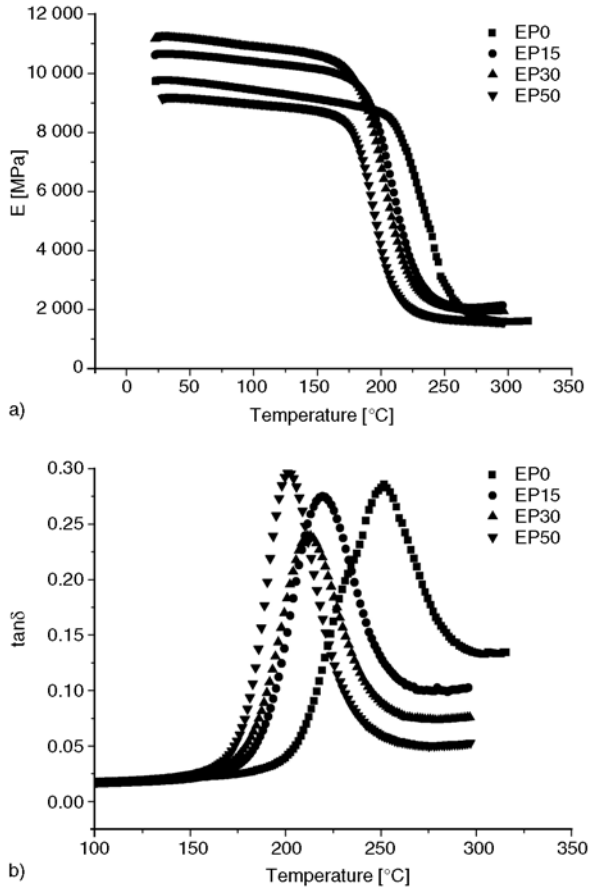

Figure 9. The DMA curves of the composites: (a) the comparison of storage modulus (b) the comparison of tanδ

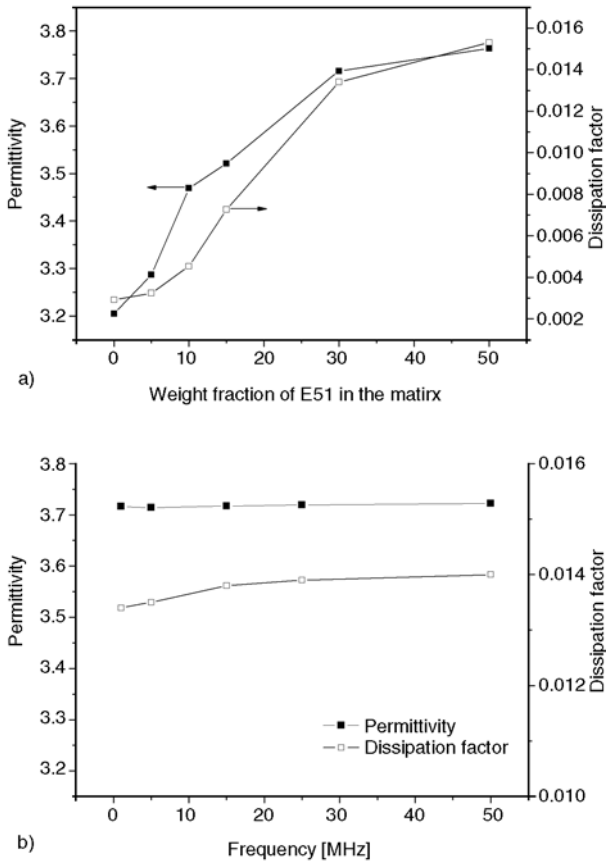

Figure 10. The dielectric property of the composites: (a) at the frequency of 1 MHz (b) in a boarder frequency rang

of the composites due to the bigger polarity of oxazolidinone structure. However, when the content of EP-51 is small the influence is not significant and when the content of EP-51 is over 30 wt% the increasing rates of permittivity and dissipation factor slow down. Figure 10b shows the influence of frequency on the dielectric property of the composite containing 30 wt% of EP-51 in the matrix. From this figure we can find that the influence of frequency on the permittivity and dissipation factor of the composites is small.

4. Conclusions

EP-51 can improve the flexural and impact strengths of DCPDCE because of the repairing of defects and the reducing of crosslink density of the cured resin. The ILSS of the fabric reinforced composites is enhanced resulted from the improvement of toughness of the matrix and the formation of polar structure of oxazolidinone which adheres to the fibers more easily. The enhancement of the interfacial adhesion hampers the microcrack propagating along the fiber/matrix interface. When the content of EP-51 in the matrix is 15~30 wt%, the improvements of the mechanical properties of the matrix and the composites are bigger than other range of EP-51 content.

The addition of EP-51 has negative effects on the thermal and dielectric property of the composites and the influence of frequency on the permittivity and dissipation factor of the composites is small.

Acknowledgements

This work was supported by a grant from the Ph.D. Programs Foundation of Ministry of Education of China (No. 20050699034).

References

[1] Kuntman A., Kuntman H.: A study on dielectric properties of a new polyimide film suitable for interlayer dielectric material in microelectronics applications. Microelectronic Journal, **31**, 629–634 (2000).

[2] Hu T., Juuti J., Jantunen H., Vilkman T.: Dielectric properties of BST/polymer composite. Journal of the European Ceramic Society, **27**, 3997–4001 (2007).
[3] Jiang L., Liu J., Wu D., Li H., Jin R.: A methodology for the preparation of nanoporous polyimide films with low dielectric constants. Thin Solid Films, **510**, 241–246 (2006).
[4] Homma T., Yamaguchi M., Kutsuzawa Y., Otsuka N.: Electrical stability of polyimide siloxane films for interlayer dielectrics in multilevel interconnections. Thin Solid Films, **340**, 237–241 (1999).
[5] Maier G.: Low dielectric constant polymers for microelectronics. Progress in Polymer Science, **26**, 3–65 (2001).
[6] Lin R-H., Lu W-H., Lin C-W.: Cure reactions in the blend of cyanate ester with maleimide. Polymer, **45**, 4423–4435 (2004).
[7] Hwang H-J., Wang C-S.: Thermal behavior and properties of naphthalene containing bismaleimide-triazine resins. Journal of Applied Polymer Science, **68**, 1199–1207 (1998).
[8] Shieh J-Y., Hwang H-J., Yang S-P., Wang C-S.:Synthesis and properties of a cyanate ester containing dicyclopentadiene(II). Journal of Polymer Science, Part A: Polymer Chemistry, **43**, 671–681 (2005).
[9] Schulze K., Schuldt U., Kahle O., Schulz S. E., Uhlig M., Uhlig C., Dreyer C., Bauer M., Gessner T.: Novel low-k polycyanurates for integrated circuit (IC) metallization. Microelectronic Engineering, **82**, 356–361 (2005).
[10] Hwang H-J., Li C-H., Wang C-S.: Dielectric and thermal properties of dicyclopentadiene containing bismaleimide and cyanate ester. Part IV. Polymer, **47**, 1291–1299 (2006).
[11] Hamerton I.: Chemistry and technology of cyanate ester resins. Chapman and Hall, London (1994).
[12] Srinivasan S. A., McGrath J. E.: Amorphous phenolphthalein-based poly(arylene ether) modified cyanate ester networks: 1. Effect of molecular weight and backbone chemistry on morphology and toughenability. Polymer, **39**, 2415–2427 (1998).
[13] Chang J. Y., Hong J. L.: Morphology of poly(ether sulfone)-modified polycyanurates. Journal of Polymer Research, **4**, 203–211 (1997).
[14] Tao Q., Gan W., Yu Y., Wang M., Tang X., Li S.: Viscoelastic effects on the phase separation in thermoplastics modified cyanate ester resin. Polymer, **45**, 3505–3510 (2004).
[15] Fang T., Shimp D. A.: Polycyanate esters: Science and application. Progress in Polymer Science, **20**, 61–118 (1995).
[16] Hayashi T., Nakamura H., Suzuki T.: Characterization of the curing behaviour of cyanic ester by a positron-annihilation lifetime technique. Polymer, **40**, 1053–1056 (1999).
[17] Martin M. D., Ormaetxea M., Harismendy I., Remiro P. M., Mondragon I.: Cure chemo-rheology of mixtures based on epoxy resins and ester cyanates. European Polymer Journal, **35**, 57–68 (1999).
[18] Thomason J. L.: Investigation of composite interphase using dynamic mechanical analysis: artifacts and reality. Polymer Composites, **11**, 105–113 (1990).
[19] Mallarino S., Chailan J. F., Vernet J. L.: Glass fibre sizing effect on dynamic mechanical properties of cyanate ester composites I. Single frequency investigations. European Polymer Journal, **41**, 1804–1811 (2005).
[20] Komalan C., George K. E., Kumar P. A. S., Varughese K. T., Thomas S.: Dynamic mechanical analysis of binary and ternary polymer blends based on nylon copolymer/EPDM rubber and EPM grafted maleic anhydride compatibilizer. Express Polymer Letters, **1**, 641–653 (2007).
[21] Ashida M., Noguchi T., Mashimo S.: Effect of matrix's type on the dynamic properties for short fiber-elastomer composite. Journal of Applied Polymer Science, **30**, 1011–1021 (1985).
[22] Dong S., Gauvin R.: Application of dynamic mechanical analysis for the study of the interfacial region in carbon fiber/epoxy materials. Polymer Composites, **14**, 414–420 (1993).

eXPRESS Polymer Letters Vol.2, No.2 (2008) 126–132
Available online at www.expresspolymlett.com
DOI: 10.3144/expresspolymlett.2008.17

Fire retardancy and environmental assessment of rubbery blends of recycled polymers

*Sz. Matkó, I. Répási, A. Szabó, B. Bodzay, P. Anna, Gy. Marosi**

Budapest University of Technology and Economics, Department of Organic Chemistry and Technology, Budafoki út 8., H-1111 Budapest, Hungary

Received 24 October 2007; accepted in revised form 3 January 2008

Abstract. Flame retarded thermoplastic polymer compounds were prepared containing recycled rubber tyres, low density polyethylene, ethylene vinyl acetate copolymer and an intumescent additive system consisting of waste polyurethane foam and ammonium polyphosphate. The effect of the additives on the combustion properties was characterised by Limiting Oxygen Index, UL 94 and mass loss calorimetric measurements. The environmental impact was estimated by determining the gas components of CO_2 and CO evolving from the compounds during the burning process using a gas analyser system constructed by coupling an FTIR unit to a mass loss calorimeter. The new material forms a thermoplastic rubber of excellent processability making it suitable for application in construction industry.

Keywords: *recycling, rubber waste, intumescent flame retardant, evolved gas analysis, polyurethane*

1. Introduction

There are over 2.5 million tonnes of waste tyres arising in Europe each year. This high amount initiated the commencement of the 2000/53/EC directive of the European Parliament and of the Council [1], which prescribes the recovery, reuse and recycling of the end-of life vehicles including rubber tyres. Since July 2006, waste tyres have been totally banned from landfills.

Utilizing options of waste rubber vulcanizates are incineration, pyrolysis [2, 3], gasification [4–6], devulcanization (e.g. chemical [7], mechanochemical [8, 9], supercritical [10, 11], ultrasonic [12, 13]), or blending either in thermoset [14–16] or in thermoplastic [17–19] polymer matrices. In this work we selected the last mentioned option combining it with upgrading that is to transform the rubber waste containing compound to a special flame retardant material.

There are known many ways to obtain flame retardant rubbers (synthetic or natural) or rubber containing composites by incorporation of flame retardant additive. E.g. ammonium polyphosphate/aluminium trihydroxide system [20], ammonium polyphosphate [21], ethylene-diamine phosphate [21] or nanoparticles (e.g. nanoclays [22], nano-calcium sulphate [23], nano-magnesium hydroxide [24–26]) are suitable flame retardants.

In our work we used ammonium polyphosphate/polyurethane intumescent additive system. This system proved to be an effective flame retardant in ethylene propylene rubber [27], polypropylene [28] and ethylene vinyl acetate copolymer matrices [29, 30]. Bugajny *et al.* pointed out that the chemical reaction taking place between ammonium polyphosphate and thermoplastic polyurethane leads to the formation of an intumescent shield and provides improved thermal stability for the material [31].

*Corresponding author, e-mail: gmarosi@mail.bme.hu

Carbon dioxide/carbon monoxide yield ratio and toxicity of fires can be evaluated from small scale tests such as cone calorimeter or tube furnace (Purser furnace) methods [32, 33]. However the results obtained from these tests may differ because of the varying test conditions (e.g. vitiated combustion, rapid quenching of the fire gases, less- or well-ventilated conditions etc).

This work focuses on the flame retardant effect of APP/PU intumescent additive system in LDPE/EVA based polymer matrix containing rubber waste, and on the environmental effect of the additive by analysing the evolved gases during combustion. The flammability was tested by LOI, UL 94 and mass loss calorimeter and the gas analysis was performed by FTIR attached in line to the mass loss calorimeter.

2. Experimental

2.1. Materials

Low density polyethylene (*LDPE*): Tipolen AE 2016 (TVK Rt. Hungary). *Ethylene vinyl acetate copolymer* (*EVA*): Ibucell K-100 (H. B. Fuller, Germany). *Recycled rubber* (*RUB*): the 200–600 μm fraction of a rubber powder prepared by an ultra high pressure water jet cutting process [34] (Regum Kft. Hungary). *Ammonium polyphosphate* (*APP*): Exolit AP 422 (Clariant Ltd. Germany). *Recycled polyurethane foam* (*PU*): ground, freon free waste polyurethane foam recovered from fridges (Amatech-Polycel Inc. Germany). *Glycerol monostearate* (*GMS*): commercial product (Chemiplast Kft. Hungary).

2.2. Preparation of samples

Compounding: the components were homogenised in a Brabender Plasti Corder PL 2000 apparatus, at 150°C, with a rotor speed of 50 rpm, for 10 min. *Test sheets:* the blends were compressed in a Collin P 200 E laboratory compression moulding machine at 150°C, with 10 bar, for 10 min.

2.3. Methods of evaluation

UL 94 flammability and *Limiting Oxygen Index* (*LOI*) *according to the standards* [35, 36]. *Mass loss calorimetry* with heat flux of 50 kW (this value corresponds to the heat generated in a well-developed fire [38]), without direct ignition according to the standard [37]. *Infrared gas analysis* (*FTIR*): the gas evolving from the samples being exposed to 50 kW/m^2 radiation in the mass loss calorimeter was analysed by a Bruker Tensor 37 FTIR. The mass loss calorimeter was connected (at atmospheric pressure) with the infrared spectrometer according to Figure 1, by interface elements con-

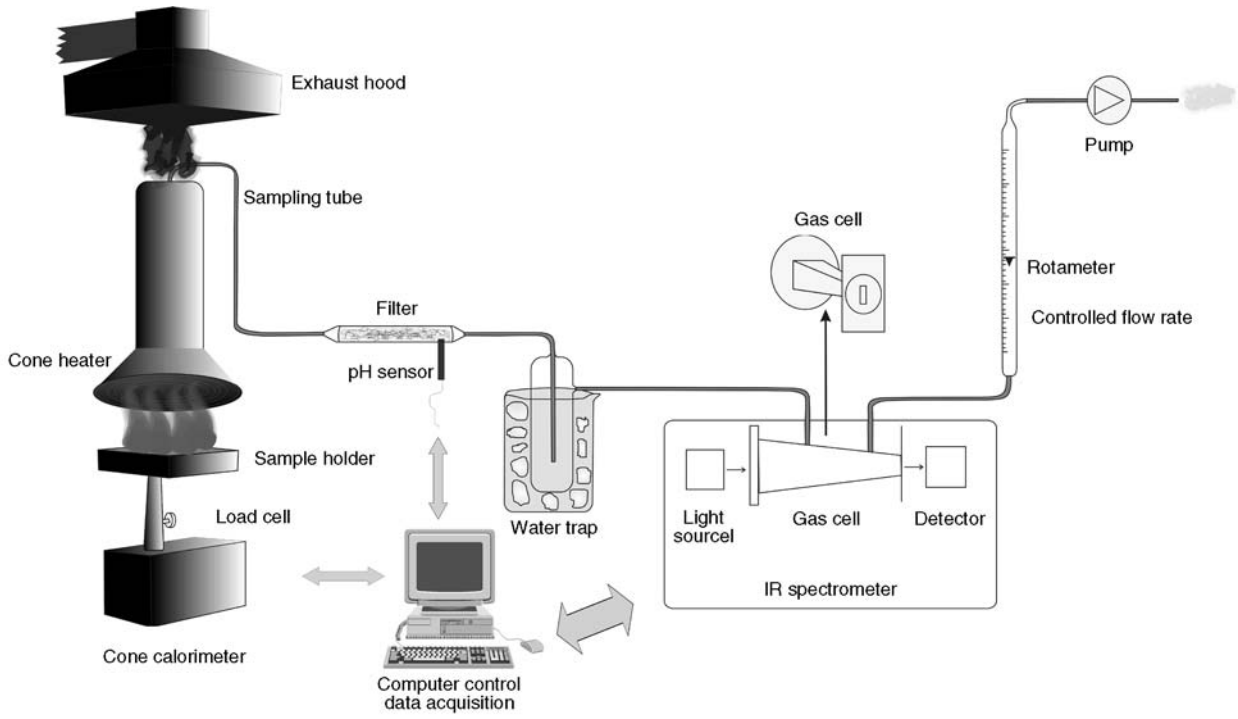

Figure 1. Scheme of gas analyzer consisting of the mass loss calorimeter, FTIR spectrometer and interface elements

sisting of glass sampling tube, glass-wool filled filter and condenser, in order to detect the evolved gases. The pathlength of the single pass gas cell was 100 mm made of stainless steel. As the gas cell contains a NaCl window, which is sensitive to water, the evolved water vapour was condensed in a trap cooled by the mixture of water and ice. The spectra recorded throughout the test were evaluated by Opus 5.5 software in the range of 650–4000 cm^{-1}. Among the toxic products we focused on CO and CO_2 with characteristic bands at (2171 and 2118 cm^{-1}) and (2363, 2341 and 2336 cm^{-1}) and identified by using Reference [39].

Mechanical properties: tensile properties (tensile strength, relative elongation at break and tensile modulus) were measured according to the standard [40] by a Zwick Z020 testing machine. The measurements were evaluated by TestXpert V10.11 software.

3. Results and discussion

3.1. Flammability

The compositions of the Reference, of the compounds containing APP/PU intumescent additive system (Samples 1–3) and of the compound containing APP/PU/RUB additive system (Sample 4) are given in Table 1. The APP/PU weight ratio was 1/1 in all cases. The LDPE/EVA weight ratio was also constant in all samples. Table 1 contains also the results of UL 94 and LOI flammability tests and the characteristic values could be evaluated from the Heat release rate (Figure 2) and Mass loss curves (Figure 3) of mass loss calorimetric measurements.

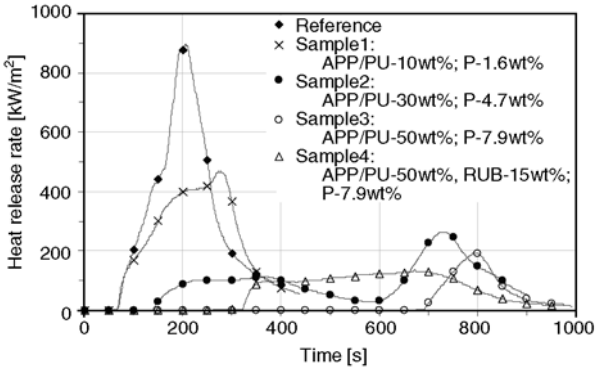

Figure 2. Heat release rate (HRR) vs. Time in mass loss calorimetric measurement of the compounds

Comparing the characteristics of Reference and Sample 1, it can be seen that phosphorus content of 1.6 wt% does not lead to improvement in either UL 94 grade, LOI or t_{ign}. Both Reference and Sam-

Table 1. Composition in wt% and flame-retardant characteristics of Reference and Sample 1, 2, 3 and 4

Components	Reference	1	2	3	4
LDPE	26.6	23.9	18.5	13.1	9.1
EVA	72.4	65.1	50.5	35.9	24.9
APP	–	5.0	15.0	25.0	25.0
PU	–	5.0	15.0	25.0	25.0
RUB	–	–	–	–	15.0
GMS	1.0	1.0	1.0	1.0	1.0
Total	100.0	100.0	100.0	100.0	100.0
Characteristics					
Phosphorus content [wt%]	0.0	1.6	4.7	7.9	7.9
UL 94 measurement					
Horizontal burning					
Flame velocity [mm/min]	37.2 ± 2.8	35.0 ± 1.0	extinguish	extinguish	extinguish
Dripping	yes	yes	no	no	no
Vertical burning					
Dripping	yes	yes	yes	no	no
Grade	H-B	H-B	V-2	V-0	V-0
LOI, (V/V) [%]	22	22	26	30	29
Mass loss calorimetric measurement					
Time to ignition (t_{ign}) [s]	70	70	140	695	325
Peak of Heat Release Rate (HRR_{max}) [kW/m^2]	900	475	275	190	135
Time to HRR_{max} ($t_{HRR_{max}}$) [s]	205	275	730	795	670
Final residue (*res*) [wt%]	0	3	13	23	32
Time to final residue (t_{res}) [s]	250	310	860	830	850
Average Mass Loss Rate (MLR = 60·(100–res)/t_{res}) [wt%/min]*	24.0	18.8	6.1	5.6	4.8

*Equal to the average slope of the Residual mass vs. Time curve multiplied by (–1)

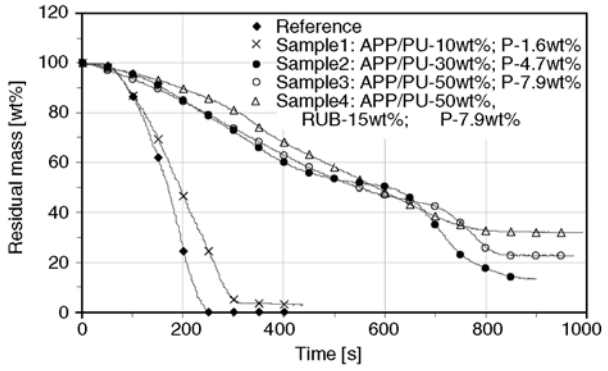

Figure 3. Residual Mass vs. Time in mass loss calorimetric measurement of the compounds

ple 1 was dripping and burnt away completely (see values of *res*). However the HRR_{max} dropped by approx. 50%, the reduction of *MLR* exceeded 20% and $t_{HRR_{max}}$ increased moderately, by 70 s. The flame velocity at horizontal burning reduced moderately, by approx. 6%.

The increase of phosphorus content (Sample 1–3) led to a direct improvement in both UL 94 (up to V-0 grade) and LOI (up to 30). Values of t_{ign} and *res* increased tendentiously. At the same time HRR_{max} and *MLR* decreased significantly. Comparing to Sample 1, $t_{HRR_{max}}$ shifted towards the higher ranges, by 455 s (Sample 2) and 520 s (Sample 3). This means an extremely extended term available for escape in case of building or vehicle fire where the interior plastic parts are made of these compounds. Expressive drop of *MLR* values, to approx. a fourth that of Reference could be observed.

The introduction of rubber powder to the compound, containing the APP/PU flame retardant additive system 50.0 wt% on the expense of LDPE/EVA matrix (Sample 4) affected the burning properties quite variously compared to the Sample 3, containing the same amount of APP/PU system. The alteration in the LOI value was negligible. The UL 94 grade kept its value. On the other hand the HRR_{max} decreased by approx. 30%. HRR_{max} being less than a sixth that of the Reference and $t_{HRR_{max}}$ being more than 10 minutes, provides increased chance of escape in case of fire. The amount of *res* increased by 9 wt%, while a 15% decrease in *MLR* was realized.

3.2. Gas emission

Knowledge about the products of combustion process, mainly about the gases emitted from materials to be applied in the interior of buildings, is important. Even if a material basically is flame-retardant under forced burning conditions it will more or less decompose.

The forced burning can be modelled either by oxygen consumption cone [41] or mass loss calorimeter. The evolved gases can be piped in the measuring cell of an FTIR spectrometer and analysed in line throughout the burning process. The scheme of such a construction is demonstrated in Figure 1. The 3D FTIR spectra of the Reference and Sample 1, 3 and 4 can be seen in Figure 4.

The reference and flame retarded samples differ largely, especially in respect of the maximum absorbance in the wavenumber region characteristic for the CO_2 and CO gas components.

The relative amount of the evolved gases was calculated by integration of the 3D FTIR spectra. The integrals for CO_2 and CO and the CO_2/CO yield ratios are presented in Table 2.

Introduction of 10% APP/PU system reduced the amount of evolved CO_2 and CO by 15 and 19%, respectively (Reference and Sample 1).

The amount of CO_2 and CO decreased with increasing APP/PU content (Sample 1–3). Comparing Sample 1 and 3, a 70 and a 60% decrease in the amount of CO_2 and CO was realized, respectively. Comparing Sample 2 and 3, the drastic cutback in the amount of CO_2 to a value of less than a third resulted in the decrease of CO_2/CO yield ratio to approx. a half.

Sample 4, prepared by incorporation of rubber powder in the composition Sample 3 on expense of LDPE/EVA, gives an increased amount of both CO_2 and CO, compared to the Sample 3. These values, even so, are approx. 50 and 60% those of Reference, respectively.

Table 2. Relative amount of the evolved CO_2 and CO gases. CO_2/CO yield ratios for Reference and Sample 1, 2, 3 and 4

Values evaluated from the FTIR spectra	Reference	1	2	3	4
Relative amount of evolved CO_2 [–]	12590	10762	9020	2930	6707
Relative amount of evolved CO [–]	83	67	39	26	51
CO_2/CO yield ratio [–]	151.7	160.6	231.3	112.7	131.5

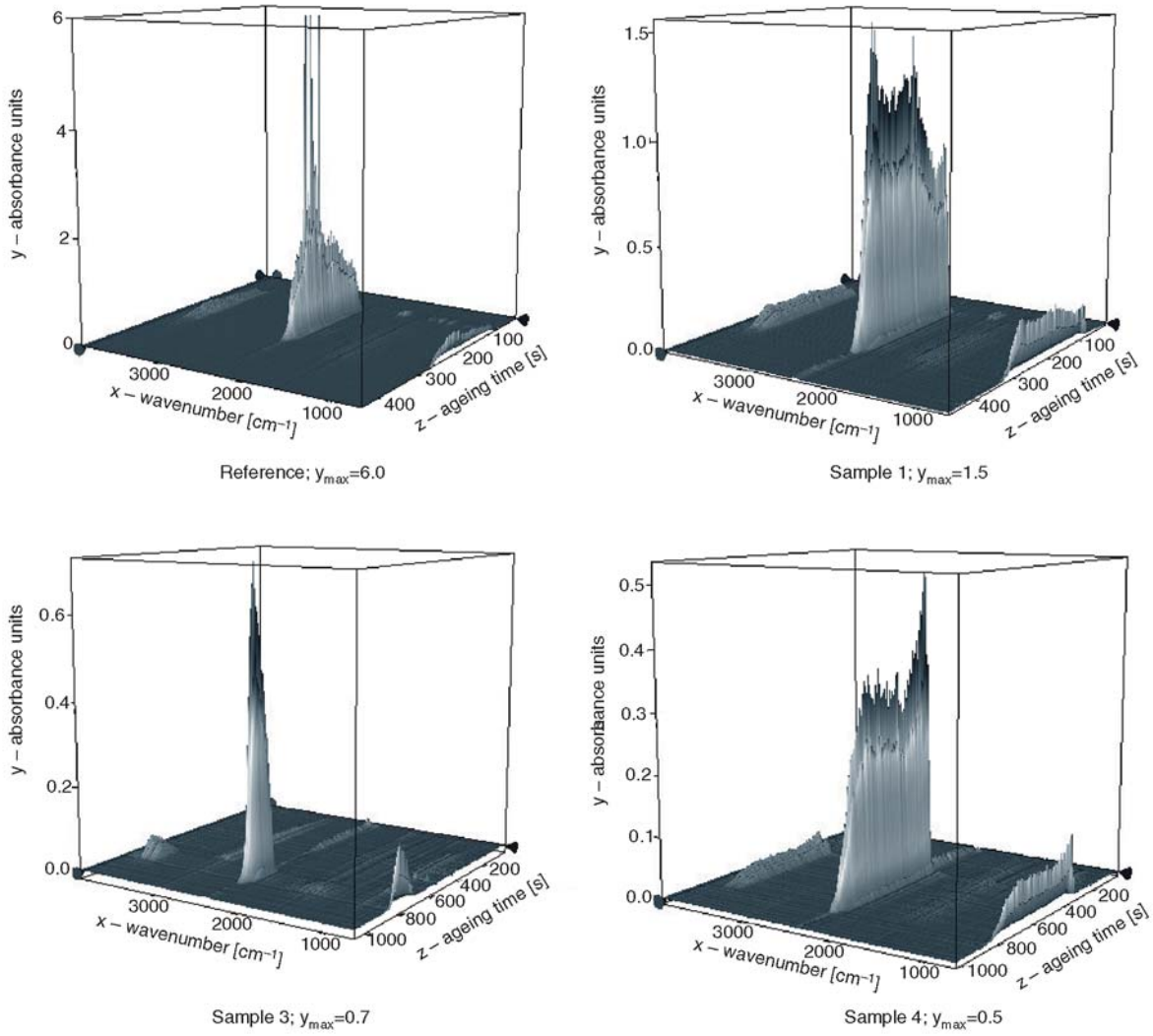

Figure 4. The 3D FTIR spectra of the gases releasing from Reference and Sample 1, 3 and 4, where y = absorbance, x = vawenumber (0–4000 cm^{-1}), z = ageing time (0–350 s)

3.3. Mechanical properties

The values of tensile strength, relative elongation at break, tensile modulus and deviations are shown in Table 3.

Both APP/PU and APP/PU/RUB systems reduce the tensile strength of the compounds, as it was expected, proportional to the amount of the additive. The decrease of relative elongation at break of the compounds with increasing amount of additive is more drastic. It has to be remarked that the introduction of RUB prevents the strong reduction of elongation at break. The addition of both APP/PU and APP/PU/RUB systems to the LDPE/EVA matrix led to an increase in stiffness. The higher the APP/PU additive content, the higher the tensile modulus (Sample 1–3). Comparing Samples 1 and 3, it increased to a value of more than three times. Preserving the content of the APP/PU system the same (50.0 wt%), addition of rubber powder resulted in a decrease by more than 10% (Sample 3 and 4). The mechanical properties of the compounds suggest, the APP/PU and APP/PU/RUB

Table 3. Values of tensile strength [MPa], relative elongation [%], tensile modulus [MPa] and deviations for Reference and Sample 1, 2, 3 and 4

Tensile properties	Reference	1	2	3	4
Tensile strength [MPa]	11.2 ± 0.6	5.8 ± 0.4	3.7 ± 0.2	2.3 ± 0.1	1.6 ± 0
Relative elongation [%]	1124 ± 23	505 ± 55	185 ± 27	6 ± 0	32 ± 4
Tensile modulus [MPa]	24.7 ± 1.9	27.7 ± 1.9	58.7 ± 0.9	82.3 ± 5.1	70.6 ± 3.4

flame retardant compounds can be used in such applications, where not tensile but compression strength is required from the products prepared from the compounds.

4. Conclusions

Flame retarded LDPE/EVA based polymeric compounds can be formulated by incorporation of an intumescent flame retardant system, consisting of waste polyurethane and ammonium polyphosphate. This system could be applied for utilization of waste rubber as well. The compound containing 40 wt% waste polyurethane and rubber powder as a whole, shows fire retardancy, low HRR_{max} and high of $t_{HRR_{max}}$, which provides chance of escape in case of fire.

The environmental impact of the compounds was detected by IR analysis of the evolved gases during the mass loss calorimetric measurements. The amount of CO_2 and CO decreased with increasing APP/PU content. The rubber powder containing compound had also a considerably reduced CO_2 and CO emission compared to Reference. The APP/PU and APP/PU/RUB systems reduced the tensile strength proportionally to the additive content. The relative elongation at break decreased by the additives more drastically; however, the RUB additive partly inhibited this effect. The introduction of additives led to an increase in modulus.

The processability of compounds containing recycled materials is excellent and applicable as fire retarded thermoplastic rubbery material for engineering purposes such as floor covering or interior panel in construction of buildings.

Acknowledgements

This work was supported by the Hungarian Ministry of Education (Multirec Project, GVOP 3.1.1.-2004-05-0531/3.0), EU 6 Nanofire project (NMP3-CT 2004-505637) and Hungarian Research Found (OTKA T049121). BUTE Natural- and Sport Scientific Assoc.

References

[1] Directive 2000/53/EC of the European Parliament and of the Council of 18 September 2000 on end-of life vehicles. Official Journal of the European Communities, **L 269**, 34–42 (2000).

[2] Zabaniotou A. A., Stavropoulos G.: Pyrolysis of used automobile tires and residual char utilization. Journal of Analytical and Applied Pyrolysis, **70**, 711–722 (2003).

[3] Barbooti M. M., Mohamed T. J., Hussain A. A., Abas F. O.: Optimization of pyrolysis conditions of scrap tires under inert gas atmosphere. Journal of Analytical and Applied Pyrolysis, **72**, 165–170 (2004).

[4] Wu W., Yoshikawa K.: R & D on micro-pyrolyzer for solid wastes using high temperature steam and air. JSME International Journal, Series B: Fluids and Thermal Engineering, **45**, 487–491 (2002).

[5] Conesa J. A., Martín-Gullón I., Font R., Jauhiainen J.: Complete study of the pyrolysis and gasification of scrap tires in a pilot plant reactor. Environmental Science and Technology, **38**, 3189–3194 (2004).

[6] Bébar L., Stehlík P., Havlen L., Oral J.: Analysis of using gasification and incineration for thermal processing of wastes. Applied Thermal Engineering, **25**, 1045–1055 (2005).

[7] Rios R. R. V. A., Gontijo M., Ferraz V. P., Lago R. M., Araujo M. H.: Devulcanization of styrenebutadiene (SBR) waste tire by controlled oxidation. Journal of the Brazilian Chemical Society, **17**, 603–608 (2006).

[8] Jana G. K., Das C. K.: Devulcanization of natural rubber vulcanizates by mechanochemical process. Polymer-Plastics Technology and Engineering, **44**, 1399–1412 (2005).

[9] Jana G. K., Das C. K.: Recycling natural rubber vulcanizates through mechanochemical devulcanization. Macromolecular Research, **13**, 30–38 (2005).

[10] Kojima M., Tosaka M., Ikeda Y.: Chemical recycling of sulfur-cured natural rubber using supercritical carbon dioxide. Green Chemistry, **6**, 84–89 (2004).

[11] Kojima M., Tosaka M., Ikeda Y., Kohjiya S.: Devulcanization of carbon black filled natural rubber using supercritical carbon dioxide. Journal of Applied Polymer Science, **95**, 137–143 (2005).

[12] Feng W., Isayev A. I.: Recycling of tire-curing bladder by ultrasonic devulcanization. Polymer Engineering and Science, **46**, 8–18 (2006).

[13] Ghose S., Isayev A. I.: Ultrasonic devulcanization of unfilled polyurethane rubber using coaxial and grooved barrel reactors: A comparative study. Journal of Polymer Engineering, **25**, 331–343 (2005).

[14] Lee D., Kim J. H.: Failure analysis on rubber-modified epoxy resin under various loading speed conditions. Key Engineering Materials, **297–300**, 1907–1912 (2005).

[15] Unnikrishnan K. P., Thachil E. T.: Toughening of epoxy resins. Designed Monomers and Polymers, **9**, 129–152 (2006).

[16] Kim N. H., Kim H. S.: Interaction of toughening mechanisms in a hybrid epoxy system. Journal of Applied Polymer Science, **100**, 4470–4475 (2006).

[17] Nakason C., Pechurai W., Sahakaro K., Kaesaman A.: Rheological, mechanical and morphological properties of thermoplastic vulcanizates based on NR-g-PMMA/PMMA blends. Polymers for Advanced Technologies, **16**, 592–599 (2005).

[18] Nakason C., Wannavilai P., Kaesaman A.: Thermoplastic vulcanizates based on epoxidized natural rubber/polypropylene blends: Effect of compatibilizers and reactive blending. Journal of Applied Polymer Science, **100**, 4729–4740 (2006).

[19] Nair M. N. R., Nair M. R. G.: Compatibility studies and characterisation of a PVC/NR blend system using NR/PU block copolymer. Polymer Bulletin, **56**, 619–631 (2006).

[20] Castrovinci A., Camino G., Drevelle C., Duquesne S., Magniez C., Vouters M.: Ammonium polyphosphate-aluminum trihydroxide antagonism in fire retarded butadiene-styrene block copolymer. European Polymer Journal, **41**, 2023–2033 (2005).

[21] Pal K., Rastogi J. N.: Development of halogen-free flame-retardant thermoplastic elastomer polymer blend. Journal of Applied Polymer Science, **94**, 407–415 (2004).

[22] Li B., Liu L., Luo H., Luo Y., Jia D.: Studies on flame retadancy of the organoclay/natural rubber nanocomposites (in Chinese). Acta Phytotaxonomica Sinica, **5**, 456–461 (2007).

[23] Mishra S., Shimpi N. G.: Effect of the variation in the weight percentage of the loading and the reduction in the nanosizes of $CaSO_4$ on the mechanical and thermal properties of styrene-butadiene rubber. Journal of Applied Polymer Science, **104**, 2018–2026 (2007).

[24] Gui H., Zhang X. H., Liu Y. Q., Dong W. F., Wang Q. G., Gao J. M., Song Z. H., Lai J. M., Qiao J. L.: Effect of dispersion of nano-magnesium hydroxide on the flammability of flame retardant ternary composites. Composites Science and Technology, **67**, 974–980 (2007).

[25] Gui H., Zhang X. H., Dong W. F., Wang Q. G., Gao J. M., Song Z. H., Lai J. M., Liu Y. Q., Huang F., Qiao J. L.: Flame retardant synergism of rubber and Mg(OH)(2) in EVA composites. Polymer, **48**, 2537–2541 (2007).

[26] Gui H., Zhang X., Dong F., Gao M., Song Z., Lai J., Liu Y., Huang F., Qiao J., Wang Q.: Effect of rubbers on the flame retardancy of EVA/ultrafine fully vulcanized powdered rubber/nanomagnesium hydroxide ternary composites. Polymer Composites, **28**, 479–483 (2007).

[27] Bugajny M., Le Bras M., Bourbigot S., Delobel R.: Thermal behaviour of ethylene-propylene rubber/polyurethane/ammonium polyphosphate intumescent formulations – a kinetic study. Polymer Degradation and Stability, **64**, 157–163 (1999).

[28] Bugajny M., Le Bras M., Bourbigot S., Poutch F., Lefebvre J-M.: Thermoplastic polyurethanes as carbonization agents in intumescent blends. Part 1: Fire retardancy of polypropylene/thermoplastic polyurethane/ammonium polyphosphate blends. Journal of Fire Sciences, **17**, 494–513 (1999).

[29] Duquesne S., Le Bras M., Delobel R., Camino G., Gengembre L.: X-ray photoelectron spectroscopy study of the ammonium polyphosphate-polyurethane system used as fire-retardant additive in EVA. Journal of Fire Sciences, **21**, 89–115 (2003).

[30] Bourbigot S., Le Bras M., Duquesne S., Rochery M.: Recent advances for intumescent polymers. Macromolecular Materials and Engineering, **289**, 499–511 (2004).

[31] Bugajny M., Le Bras M., Bourbigot S.: Thermoplastic polyurethanes as carbonization agents in intumescent blends. Part 2: Thermal behavior of polypropylene/thermoplastic polyurethane/ammonium polyphosphate blends. Journal of Fire Sciences, **18**, 7–27 (2000).

[32] Hull T. R., Wills C. L., Artingstall T., Price D., Milnes G. J.: Mechanism of smoke and CO suppression from EVA composites. in 'Fire Retardancy of Polymers – New Applications of Mineral Fillers' (eds.: Le Bras M., Wilkie C. A., Bourbigot S., Duquesne S., Jama C.) The Royal Society of Chemistry, Cambridge, 372–385 (2005).

[33] Wills C. L., Arotsky J., Hull T. R., Price D., Purser D. A., Purser J.: Products of incomplete combustion from fire studies in the Purser furnace. in 'Fire Retardancy of Polymers – New Applications of Mineral Fillers' (eds.: Le Bras M., Wilkie C. A., Bourbigot S., Duquesne S., Jama C.) The Royal Society of Chemistry, Cambridge, 386–398 (2005).

[34] Balikó L., Veres G., Vékony S.: Method of selective recovering components from multi-component elastic waste material and apparatus for producing fine-grained rubber powder. WO/2001/053053, Hungary (2001).

[35] UL 94: Tests for flammability of plastic materials for parts in devices and appliances (1996).

[36] ASTM D 2863-06a: Standard test method for measuring the minimum oxygen concentration to support candle-like combustion of plastics (Oxygen Index) (1996).

[37] ISO 13927: Plastics. Simple heat release test using a conical radiant heater and a thermopile detector (2001).

[38] Babrauskas V.: Development of the cone calorimeter. A bench-scale heat release rate apparatus based on oxygen consumption. Fire and Materials, **8**, 81–95 (1984).

[39] Socrates G.: Infrared and Raman characteristic group frequencies: Tables and charts. Wiley and Sons, New York (2004).

[40] ISO 527-2: Plastics. Determination of tensile properties. Part 2: Test conditions for moulding and extrusion plastics (1993).

[41] Zhang F., Zhang J., Wang Y.: Modeling study on the combustion of intumescent fire-retardant polypropylene. Express Polymer Letters, **1**, 157–165 (2007).

eXPRESS Polymer Letters Vol.2, No.2 (2008) 133–146
Available online at www.expresspolymlett.com
DOI: 10.3144/expresspolymlett.2008.18

Non-isothermal degradation kinetics of filled with rise husk ash polypropene composites

S. Ch. Turmanova[1*], *S. D. Genieva*[2], *A. S. Dimitrova*[1], *L. T. Vlaev*[2]

[1]Department of Materials Science, Assen Zlatarov University, 8010 Bourgas, Bulgaria
[2]Department of Physical Chemistry, Assen Zlatarov University, 8010 Bourgas, Bulgaria

Received 16 November 2007; accepted in revised form 10 January 2008

Abstract. The thermal stability and kinetics of non-isothermal degradation of polypropene and polypropene composites filled with 20 mass% vigorously grounded and mixed raw rice husks (RRH), black rice husks ash (BRHA), white rice husks ash (WRHA) and Aerosil Degussa (AR) were studied. The calculation procedures of Coats – Redfern, Madhysudanan *et al*., Tang *et al*., Wanjun *et al*. and 27 model kinetic equations were used. The kinetics of thermal degradation were found to be best described by kinetic equations of *n*-th order (F_n mechanism). The kinetic parameters E, A, $\Delta S^{\neq}$, $\Delta H^{\neq}$ and $\Delta G^{\neq}$ for all the samples studied were calculated. The highest values of n, E and A were obtained for the composites filled with WRHA and AR. A linear dependence between ln$A$ and E was observed, known also as kinetic compensation effect. The results obtained were considered enough to conclude that the cheap RRH and the products of its thermal degradation BRHA and WRHA, after vigorously grounding and mixing, could successfully be used as fillers for polypropene instead of the much more expensive synthetic material Aerosil to prepare various polypropene composites.

Keywords: *polymer composites, rice husks, thermal properties, non-isothermal degradation, kinetics*

1. Introduction

Polypropene (PP) is a major thermoplastic stereoregular polymer, widely used in many industries – construction, automotive, computer components, wire and cable, home appliances, food packing, medical bags, etc. [1–5]. The versatility of polypropene is due to its good chemical resistance, low density and a relatively high melting point, so it is useful for storing hot liquids. This polymer represents nowadays about 22 mass% of the demand for thermoplastics in the world, with a strong increase tendency [5, 6].

The thermal stability, thermal and oxidative degradation of virgin and filled polypropene composites is important from different points of view. On one hand, in a number of cases, it is necessary to increase its heat resistance by introducing certain reinforcing additives. On another hand, introduced reinforcing additives lead to an increase of the tensile strength of the composite with respect to the polymer matrix, but depending on the fillers nature the thermal stability of the composites may increase or decrease.

Incorporation of rigid inorganic particles is a promising approach to improve both stiffness and toughness of plastics simultaneously [3]. For example, polypropene composites used for insulation of electrical power distribution and transmission cables operating at temperatures higher than 70°C and under high electric field must be heat resistant, because the excess of the temperature rise in the cable is one of the main causes of dielectric failure [7]. On the other hand, polypropene constitutes are the main components of plastic waste from indus-

*Corresponding author, e-mail: sturmanova@btu.bg

trial and domestic refuse. In order to recycle plastic waste to obtain energy or low molecular hydrocarbons, other additives, for example solids, contained Lewis and Brønsted acid centers, are used to decrease the thermal stability of the composites [8–10]. Therefore, comprehension of the kinetics of its thermal degradation is of great interest for both theory and practice.

Polypropene is usually used in industry in the form of composites containing ingredients different by nature and in quantity, which improve its thermal and physico-mechanical properties, rather than in pure form. The addition of fillers to the polymer matrix is a fast and cheap method to modify the properties of the base polymer. Among the mineral fillers for PP calcium carbonate, talc, mica, silica, zinc oxide, glass, carbon black and carbon fibers are the most often used [10, 11]. Each filler adds its own characteristics to the matrix and, as a consequence, changes the properties of the composite. In the recent years, natural fibers and flours have been widely used as reinforcing fillers in thermoplastic polymer composite materials [12, 13]. These composites have several advantages, such as low cost, renewability, biodegradability and absence of associated health hazards. Agricultural residues such as rice husks; bagasse and wood chips are particularly important natural resources. Rice husks are an agricultural industrial residue produced as by-products during the rice-milling process. According to FAO statistical data [13], the annual world rice production was approximately 600 million tons in 2000, 20% of which was wasted as rice husks. Raw rice husks contain cellulose 35%, hemicellulose 25%, lignin 20%, ash 17% (94% silica) and moisture about 3% by weight [14]. Most of the rice husks are either used as a bedding material for animals and burned or used for landfilling. Therefore, the use of rice husks and its derivates in the manufacturing of thermoplastic polymer composites is attracting much attention. The rice husks ash, which is produced by burning of raw rice husks, has a high content of silica and may be used as a filler of different thermoplastics. Depending on the procedure employed during burning, two types of ashes are produced, i.e. white (WRHA) and black rice husks ash (BRHA). Much work [14–16] has been done to study the potential of raw rice husks flour RRHF, WRHA or BRHA as a filler of polyethylene or polypropene composites.

The disposal of waste polymers and particularly polypropene is a major environmental problem. Because they are not easily biologically degradable and because of their weight-to-volume ratios which creates problems of disposal, the plastics are not appropriate candidates for landfilling [8, 9, 12, 17]. Nowadays, incineration is the more widely used way to eliminate solid residues and it is also used for generation of electric and calorific energy at the same time. Uncontrolled incineration, however, can produce serious air pollution, environmental and health problems due to the possible emission of toxic flue gases (dioxins, furans), acid gases and heavy metals [5, 6, 18]. For this reason, the search for different recycling alternatives (thermal or oxidative degradation) is more and more necessary [19, 20]. One of the possible ways to treat this waste is thermal decomposition – a process yielding both energy and gaseous and liquid products, which can be further used in various ways. A recently reported alternative is to transform the polymer waste into hydrocarbons in order to produce low molecular mass chemicals, clean hydrocarbon, chemical resources, fuels, gasoline, or other valuable products such as lubricants by thermal or catalytic degradation. The thermal degradation (pyrolysis) of the polymer macromolecules in the absence of oxygen or under vacuum at elevated temperatures gives a mixture of hydrocarbons [5, 6, 8, 12, 18, 21]. According to the data from the gas chromatography/mass spectrometry analyses (GC/MS), the thermal degradation of polypropene in nitrogen medium gives dienes, alkanes, and alkenes up to C_{31} hydrocarbons [17]. However, this degradation requires a considerable quantity of energy due to its endothermic character and the low thermal conductivities of the plastic materials throughout the process. Alternatively, some solid catalysts have been proposed to decrease degradation temperature and reduce this energy requirement [22, 23]. On the other hand, solid catalysts used in the process of thermal degradation of plastics increase the yield of liquid products. Catalytic degradation requires lower temperatures, and the chemical distribution of the product is narrower than in thermal degradation, leading to the production of more valuable products. Typical catalysts used for polymer degradation are acidic solids like amorphous alumina, silica-aluminas, clays, synthetic or natural zeolites (clinoptilolite, montmorillonite, atta-

pulgite), mesoporous materials and activated carbon [3, 5, 6,1 8, 23–25]. Their behaviors may be due to the presence of Brønsted and Lewis strong acid sites, which can promote polymer chain cracking. In all these cases, the use of a catalyst reduces the energetic demand of the process and improves, from the economic point of view, the product distribution by increasing the yield of more volatile products and lowering the yield of subproducts. An important feature of catalytic degradation is the need for proper contact between the polymer and the catalyst to minimize degradation residues. However, all these catalysts are expensive and, at the moment, there are no useful ways to improve their short life and difficult recycling, so their use involves increased cost of the operational process.

Thermogravimetric analysis (TGA) is one of the thermal analysis techniques used to measure the mass change, thermal decomposition and thermal stability of composite materials. Overall kinetics can be easily obtained by measuring the change in mass of a sample with time based on isothermal or non-isothermal thermogravimetric data [2, 4, 8, 19, 26–29]. Some valuable parameters, such as apparent activation energy E, pre-exponential factor A, and reaction order n can be calculated from a thermogravimetric curve. Knowledge of the kinetic parameters associated with thermal degradation constitutes and important tool in estimating the thermal behavior of composites under dynamic conditions.

The purpose of this study is to evaluate the thermal stability of polypropene composites filled with 20 mass% raw rice husks, black or white rice husks ash, as well as establish the most appropriate mechanism of the thermal degradation and calculate the kinetic parameters characterizing this process.

2. Experimental part

2.1. Materials and measurements

The thermoplastic polymer polypropene (PP) 'Buplen' grade 6531, commercial product of Lukoil-Nephtochim (Bourgas, Bulgaria) with melt index 3–5 g/10 min (230°C/2160 g) was used as matrix for the preparation of the composites. The fillers used were raw rice husks (RRH), black rice husks ash (BRHA), white rice husks ash (WRHA) and, for comparison, Aerosil A200 (AR), product of Degussa AG (Germany).

Rice husks were obtained from suburb areas of Thrace (Pazardjik, Bulgaria). Before use, the rice husks were thoroughly washed – two times with tap water followed by three times with deionised water to remove adhering soil, clay and dust and finally dried at 102 ± 2°C overnight. The dried husks were ground in rotary cutting mill and sieved manually with 0.63–0.12 mm sieves. This starting material was used for thermal decomposition in air or nitrogen atmosphere. The thermal treatment of the rice husk fraction was carried out in quartz vertical tube, equipped with perforated quartz diaphragm at its lower end. The electrical heater used was wound around the quartz tube and insulated by asbestos sleeve. During the thermal treatment, nitrogen (or air) was flown below the quartz diaphragm into the lower end of the tube (100 $cm^3 \cdot min^{-1}$) through the treated material. In the case of thermal treatment of raw rice husks in nitrogen medium, black rice husks ash (BRHA) was obtained and in air atmosphere – white rice husks ash (WRHA), respectively. The controlled increase of the temperature was performed using electronic thermal regulator Zeitplansollwertgeber, (Germany) at heating rate of 2°C·min^{-1} up to 700°C, maintained for 2 hours, after which the ash was quenched in nitrogen or air medium and used for further experiments. All the samples were stored in plastic sealer containers and used after vigorous grinding.

Polypropene composites with 20 mass% different fillers (RRH, BRHA, WRHA and AR) were prepared. The polymer and the filler were mixed with laboratory mixing rolls at 170°C for 5 min. The compositions obtained were pressed on an electrically heated hydraulic laboratory press PHI (England) as a slab with thickness of 1 mm. The slab was first cut into chips less than 1 mm long and then used for the thermogravimetric measurements. These samples were studied in a dynamic flow of air at a rate of 30 $cm^3 \cdot min^{-1}$ under non-isothermal conditions in a derivatograph system Paulik-Paulik-Erdey (MOM, Hungary) at heating rate of 10 K·min^{-1} in the temperature region 25–600°C. Samples of 50 mg were weighted into a alumina crucible and put in it without pressing. α-Alumina calcined up to 1100°C was used as a standard reference material. The TG, DTA and DTG curves were recorded graphically with 1 mg sensitivity. The test was performed at least twice for each sample to ensure its reproducibility.

2.2. Theoretical approach and calculation procedures

The kinetics of thermal degradation reactions is described by various equations taking into account the special features of their mechanisms. The reaction rate can be expressed through the degree of conversion α according to the Equation (1):

$$\alpha = \frac{m_0 - m_i}{m_0 - m_f} \tag{1}$$

where m_0, m_f and m_i are initial, final and current sample mass at the moment t, respectively. Generally, the kinetic equation of the process can be written as Equation (2) [2, 27–30]:

$$\frac{\mathrm{d}\alpha}{\mathrm{d}t} = k(T) f(\alpha) \tag{2}$$

where $f(\alpha)$ is the conversion function and $k(T)$ is the temperature function respectively. The temperature dependence of the rate constant k for the process is described by the Arrhenius equation (3):

$$k = A \exp\left(-\frac{E}{RT}\right) \tag{3}$$

where A is the pre-exponential factor, T is the absolute temperature, R is the universal gas constant, and E is the apparent activation energy of the process. Substitution of Equation (3) in (2) gives the Equation (4):

$$\frac{\mathrm{d}\alpha}{\mathrm{d}t} = A \exp\left(-\frac{E}{RT}\right) f(\alpha) \tag{4}$$

When the temperature increases at a constant rate (Equation (5)):

$$\frac{\mathrm{d}T}{\mathrm{d}t} = q = \text{constant} \tag{5}$$

therefore Equation (6):

$$\frac{\mathrm{d}\alpha}{\mathrm{d}T} = \frac{A}{q} \exp\left(-\frac{E}{RT}\right) f(\alpha) \tag{6}$$

The conversion function $f(\alpha)$ for a solid-state reaction depends on the reaction mechanism and can generally be considered to be as Equation (7):

$$f(\alpha) = \alpha^m (1-\alpha)^n [-\ln(1-\alpha)]^p \tag{7}$$

where m, n and p are empirically obtained exponent factors, one of them always being zero [30, 31].

After substitution in Equation (6), separation of variables and integration, the following general equation (8) was obtained:

$$\int_0^{\alpha} \frac{\mathrm{d}\alpha}{\alpha^{\mathrm{m}}(1-\alpha)^{\mathrm{n}}[-\ln(1-\alpha)]^{\mathrm{p}}} = \frac{A}{q} \int_0^{T} \exp\left(-\frac{E}{RT}\right) \mathrm{d}T \tag{8}$$

The solutions of the left hand side integral depend on the explicit expression of the function $f(\alpha)$ and are denoted as $g(\alpha)$. Algebraic expressions of functions of the most common reaction mechanisms operating in solid-state reactions are summarized and presented in Table 1 [2, 4, 26, 30].

The right hand side integral in Equation (8) has no exact analytical solution and, after making some variable substitution, is expressed by the fourth Senum and Yang approximation (Equations (9) and (10)) [32, 33], which gives an accuracy better than 10^{-5}% for $x = E/RT \geq 20$.

$$\frac{A}{q} \int_0^{T} \exp\left(-\frac{E}{RT}\right) \mathrm{d}T = \frac{AE}{qR} \frac{\exp(-x)}{x^2} h(x) \tag{9}$$

$$h(x) = \frac{x^4 + 18x^3 + 86x^2 + 86x}{x^4 + 20x^3 + 120x^2 + 240x + 120} \tag{10}$$

The approximate expression was therefore used in the discussion of error of the activation energy estimated by the Coats and Redfern calculation procedure [34].

For Equation (4), considering the maximum reaction rate, leads to Equation (11):

$$-\frac{1}{\frac{\mathrm{d}f(\alpha)}{\mathrm{d}\alpha}} = -\frac{1}{f'(\alpha_{\max})} = \frac{A}{q} \frac{RT_{\max}^2}{E} \exp\left(-\frac{E}{RT_{\max}}\right) \tag{11}$$

The subscript 'max' denotes the variables at the maximum reaction rate. Furthermore, combining Equation (8) with Equation (11) gives the Equation (12):

$$g(\alpha_{\max}) \cdot f'(\alpha_{\max}) = -h\left(\frac{E}{RT_{\max}}\right) \tag{12}$$

Equation (12) indicates that $\alpha_{\max}$ value depends only on $E/RT_{\max}$ value for a definite kinetic model. This quantitative relation can be applied to estimate the limits of $\alpha_{\max}$ for various kinetic models and

Table 1. Algebraic expressions of functions $f(\alpha)$ and $g(\alpha)$ and its corresponding mechanism [2, 4, 26, 30]

No.	Mecha-nism	Name of the function	g(α)	f(α)	Rate-determining mechanism
1. Chemical process or mechanism non-invoking equations					
1.	$F_{1/3}$	One-third order	$1-(1-\alpha)^{2/3}$	$(3/2)(1-\alpha)^{1/3}$	Chemical reaction
2.	$F_{3/4}$	Three-quarters order	$1-(1-\alpha)^{1/4}$	$4(1-\alpha)^{3/4}$	Chemical reaction
3.	$F_{3/2}$	One and a half order	$(1-\alpha)^{-1/2}-1$	$2(1-\alpha)^{3/2}$	Chemical reaction
4.	F_2	Second order	$(1-\alpha)^{-1}-1$	$(1-\alpha)^2$	Chemical reaction
5.	F_3	Third order	$(1-\alpha)^{-2}-1$	$(1/2)(1-\alpha)^3$	Chemical reaction
2. Acceleratory rate equations					
6.	$P_{3/2}$	Mampel power law	$\alpha^{3/2}$	$(2/3)\alpha^{-1/2}$	Nucleation
7.	$P_{1/2}$	Mampel power law	$\alpha^{1/2}$	$2\alpha^{1/2}$	Nucleation
8.	$P_{1/3}$	Mampel power law	$\alpha^{1/3}$	$3\alpha^{2/3}$	Nucleation
9.	$P_{1/4}$	Mampel power law	$\alpha^{1/4}$	$4\alpha^{3/4}$	Nucleation
10.	E_1	Exponential law	$\ln\alpha$	α	Nucleation
3. Sigmoidl rate equations or random nucleation and subsequent growth					
11.	A_1, F_1	Avrami-Erofeev eq.	$-\ln(1-\alpha)$	$1-\alpha$	Assumed random nucleation and its subsequent growth, $n = 1$
12.	$A_{3/2}$	Avrami-Erofeev eq.	$[-\ln(1-\alpha)]^{2/3}$	$(3/2)(1-\alpha)[-\ln(1-\alpha)]^{1/3}$	Assumed random nucleation and its subsequent growth, $n = 1.5$
13.	A_2	Avrami-Erofeev eq.	$[-\ln(1-\alpha)]^{1/2}$	$2(1-\alpha)[-\ln(1-\alpha)]^{1/2}$	Assumed random nucleation and its subsequent growth, $n = 2$
14.	A_3	Avrami-Erofeev eq.	$[-\ln(1-\alpha)]^{1/3}$	$3(1-\alpha)[-\ln(1-\alpha)]^{2/3}$	Assumed random nucleation and its subsequent growth, $n = 3$
15.	A_4	Avrami-Erofeev eq.	$[-\ln(1-\alpha)]^{1/4}$	$4(1-\alpha)[-\ln(1-\alpha)]^{3/4}$	Assumed random nucleation and its subsequent growth, $n = 4$
16.	A_u	Prout-Tomkins eq.	$\ln[\alpha/(1-\alpha)]$	$\alpha(1-\alpha)$	Branching nuclei
4. Deceleratory rate equations **4.1. Phase boundary reaction**					
17.	R_1, F_0, P_1	Power law	α	$(1-\alpha)^0$	Contracting disk
18.	R_2, $F_{1/2}$	Power law	$1-(1-\alpha)^{1/2}$	$2(1-\alpha)^{1/2}$	Contracting cylinder (cylindrical symmetry)
19.	R_3, $F_{2/3}$	Power law	$1-(1-\alpha)^{1/3}$	$3(1-\alpha)^{2/3}$	Contracting sphere (spherical symmetry)
4.2. Based on the diffusion mechanism					
20.	D_1	Parabola low	α^2	$1/2\alpha$	One-dimensional diffusion
21.	D_2	Valensi eq.	$\alpha+(1-\alpha)\ln(1-\alpha)$	$[-\ln(1-\alpha)]^{-1}$	Two-dimensional diffusion
22.	D_3	Jander eq.	$[1-(1-\alpha)^{1/3}]^2$	$(3/2)(1-\alpha)^{2/3}[1-(1-\alpha)^{1/3}]^{-1}$	Three-dimensional diffusion, spherical symmetry
23.	D_4	Ginstling-Brounstein eq.	$1-2\alpha/3-(1-\alpha)^{2/3}$	$(3/2)[(1-\alpha)^{-1/3}-1]^{-1}$	Three-dimensional diffusion, cylindrical symmetry
24.	D_5	Zhuravlev, Lesokin, Tempelman eq.	$[(1-\alpha)^{-1/3}-1]^2$	$(3/2)(1-\alpha)^{4/3}[(1-\alpha)^{-1/3}-1]^{-1}$	Three-dimensional diffusion
25.	D_6	anti-Jander eq.	$[(1+\alpha)^{1/3}-1]^2$	$(3/2)(1+\alpha)^{2/3}[(1+\alpha)^{1/3}-1]^{-1}$	Three-dimensional diffusion
26.		anti-Ginstling-Brounstein eq.	$1+2\alpha/3-(1+\alpha)^{2/3}$	$(3/2)[(1+\alpha)^{-1/3}-1]^{-1}$	Three-dimensional diffusion
27.		anti-Zhuravlev, Lesokin, Tempelman eq.	$[(1+\alpha)^{-1/3}-1]^2$	$(3/2)(1+)^{4/3}[(1+\alpha)^{-1/3}-1]^{-1}$	Three-dimensional diffusion

then classify the kinetic models by the magnitude of α_{max}. This is because ordinary reactions have $E/RT = 15–70$, correspondingly $h(E/RT) = 0.8879–0.9726$. For n-th order reactions $f(\alpha) = (1–\alpha)^n$, Equation (12) thus turns into Equations (13) and (14).

$$1-\alpha_{max}=\left[1-\frac{n-1}{n}h\left(\frac{E}{RT_{max}}\right)\right]^{1/(n-1)} \quad \text{for} \quad n\neq 1 \tag{13}$$

and

$$-\ln(1-\alpha_{max})=h\left(\frac{E}{RT_{max}}\right) \quad \text{for } n=1 \tag{14}$$

Based on Equations (13) and (14), the limits of α_{max} at various n values are estimated and listed in Table 2, which is useful to determine the reaction order from experimental α_{max} value [32, 33].

For the present study, the calculation procedure of Coats and Redfern [34] was used. Data from TG and DTG curves in the decomposition range 0.1–0.9 were used to determinate the kinetic parameters of the process. The kinetic parameters can be derived using a modified Coats and Redfern equation (15):

$$\ln\frac{g(\alpha)}{T^2}=\ln\frac{AR}{qE}-\frac{E}{RT} \tag{15}$$

where $g(\alpha)$ is a function, the expression of which depends on the kinetic model of the occurring reaction. If the correct $g(\alpha)$ is used, a plot of $\ln[g(\alpha)/T^2]$ against $1/T$ should give a straight line from which the values of the activation energy E and the pre-exponential factor A in Arrhenius equation can be calculated. The formal expressions of the functions $g(\alpha)$ depend on the conversion mechanism and its mathematical model [2, 27–30]. The latter usually represents the limiting stage of the reaction – the chemical reactions; random nucleation and nuclei growth; phase boundary reaction or diffusion. For the correct $g(\alpha)$ (Table 1), the corresponding linear dependence should give the highest correlation coefficient at the linear regression analysis.

Later, a number of authors [35–36] suggested different solutions for the temperature integral in Equation (8), insisting that they increase the accuracy with which the kinetic parameters are calculated. For instance, Madhysudanan – Krishnan – Ninan [35] suggested the Equation (16):

$$\ln\left[\frac{g(\alpha)}{T^{1.921503}}\right]=\left[\ln\frac{AR}{qR}+3.772050-1.921503\ln E\right]-0.120394\frac{E}{T} \tag{16}$$

Tang *et al.* [36] offered another kinetic equation (17):

$$\ln\left[\frac{g(\alpha)}{T^{1.894661}}\right]=\left[\ln\frac{AR}{qR}+3.63504095-1.894661\ln E\right]-0.00145033\frac{E}{T} \tag{17}$$

and Wanjun *et al.* [37] used the Equation (18):

$$\ln\left[\frac{g(\alpha)}{T^2}\right]=\left[\ln\frac{AE}{q(1.00198882E+1.87391198RT_p)}\right]-\frac{E}{RT} \tag{18}$$

Equations (15–18) suggest certain differences between the calculated values of the apparent activation energy E and pre-exponential factor A even when the same $g(\alpha)$ function is used. To estimate which of these four calculation procedures would be most adequate for the computations, the maximum value of the linear regression correlation coefficient R^2 was used. Concerning the calculations of the kinetic parameters, a computer program was developed for all the data manipulations.

The values of the pre-exponential factor A in Arrhenius equation for solid phase reactions are expected to be in wide range (six or seven orders of magnitude), even after the effect of surface area is corrected for [28, 30]. Empirical first order pre-expo-

Table 2. The theoretical limits* of α_{max} of n-th order reactions at various n values

α_{max}	n	α_{max}	n
0.913–0.920	0.1	0.569–0.604	1.1
0.850–0.862	0.2	0.551–0.587	1.2
0.799–0.816	0.3	0.534–0.571	1.3
0.756–0.777	0.4	0.519–0.557	1.4
0.719–0.743	0.5	0.504–0.543	1.5
0.687–0.713	0.6	0.491–0.531	1.6
0.659–0.687	0.7	0.478–0.519	1.7
0.633–0.663	0.8	0.466–0.507	1.8
0.610–0.642	0.9	0.455–0.496	1.9
0.588–0.622	1.0	0.444–0.486	2.0

*Corresponding to $E/RT = 15\div70$

nential factors may vary from 10^4 to 10^{18} s^{-1}. The low factors will often indicate a surface reaction, but if the reactions are not dependent on surface area, the low factor may indicate a 'tight' complex. The high factors will usually indicate a 'loose' complex. Even higher factors (after correction of surface area) can be obtained if the complexes have free translation on the surface. Since the concentrations in the solid are not controllable in many cases, it would have been convenient if the magnitude of the pre-exponential gave an indication of the molecularity. This appears to be true only for nonsurface-controlled reactions having low ($<10^9$ s^{-1}) pre-exponential factors. Such reactions (if elementary) can only be bimolecular.

From the theory of the activated complex (transition state) of Eyring [27–30], it is known that (Equation (19)):

$$A = \frac{e\chi k_B T_p}{h} \exp\left(\frac{\Delta S^{\neq}}{R}\right) \tag{19}$$

where e = 2.7183 is the Neper number; χ – transmission factor, which is unity for monomolecular reactions; k_B – Boltzmann constant; h – Plank constant, and T_p is the peak temperature of the DTA curve. The change of entropy $\Delta S^{\neq}$ may be calculated according to the Equations (20) and (21) [28, 30]:

$$\Delta S^{\neq} = R \ln \frac{Ah}{e\chi k_B T_p} \tag{20}$$

Since

$$\Delta H^{\neq} = E - RT_p \tag{21}$$

the changes of the enthalpy $\Delta H^{\neq}$ and Gibbs free energy $\Delta G^{\neq}$ for the activated complex formation from the reagent can be calculated using the well known thermodynamic equation (22):

$$\Delta G^{\neq} = \Delta H^{\neq} - T_p \Delta S^{\neq} \tag{22}$$

When studying the kinetics of reactions of the same type using the correct $g(\alpha)$ function, the straight lines characterizing the kinetics of these reactions usually cross at a point with co-ordinates $\ln k_{iso}$ and $1/T_{iso}$. This point corresponds to the so-called isokinetic temperature T_{iso}, at which the rate constants of the reactions have the same value – k_{iso}. This means that at temperatures higher than T_{iso}, the reactions occurring at higher E would have higher rate (higher rate constants) than these with lower activation energies. It turned out that the following linear dependence exists between $\ln A$ and E in these cases (Equation (23)):

$$\ln A = \ln k_{iso} + \frac{E}{RT_{iso}} \tag{23}$$

which is known also as kinetic compensation effect, isokinetic effect, or θ – rule [28, 38, 39–41]. Besides, linear dependence between E and $\Delta S^{\neq}$ can also be observed [38].

3. Results and discussion

The controlled burning of the raw rice husks in air atmosphere lead to production of white rice husk ash (WRHA) or so-called 'white ash', which contained almost pure (≥ 95%) silica in a hydrated amorphous form, similar to silica gel, with high porosity and reactivity and about 5 mass% inorganic impurities as an aluminium, calcium, magnesium and iron oxides. The controlled pyrolysis of the raw rice husks in nitrogen medium leads to production of black rice husk ash (BRHA) or so-called 'black ash', which contained 45 mass% carbon, 50 mass% silica and about 5 mass% inorganic impurities. According to the data from X-ray analysis, all the fillers used were amorphous. The physicochemical characteristics of the fillers used are shown in Table 3.

Table 3. Physicochemical characteristics of the RRH, WRHA, BRHA and AR

Parameter	RRH	WRHA	BRHA	AR
SiO_2 [mass%]	20.2	94.2	54.0	100
Moisture [mass%]	7.1	<0.5	<0.5	<0.5
Mean particle size [μm]	80	50	60	20
Surface area [$m^2 \cdot g^{-1}$]	<1	228	141	273
True density [$g \cdot cm^{-3}$]	1.47	2.2	1.8	2.2

3.1. Kinetic studies

The thermogravimetric curves of pure polypropene and polypropene filled with 20 mass% different by nature fillers measured at heating rate of 10 $K \cdot min^{-1}$ are presented in Figure 1. As it can be seen from the figure, the shapes of the TG curves are quite different. As far as the polymer is concerned, its degrada-

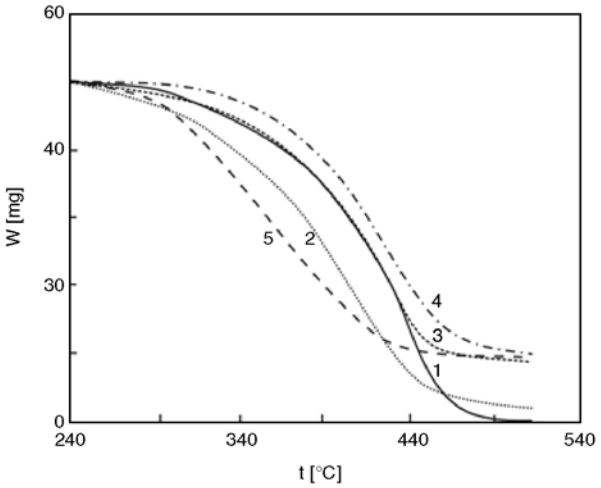

Figure 1. TG curves of pure polypropene – 1, polypropene filled with 20 mass% RRH – 2, BRHA – 3, WRHA – 4 and AR –5

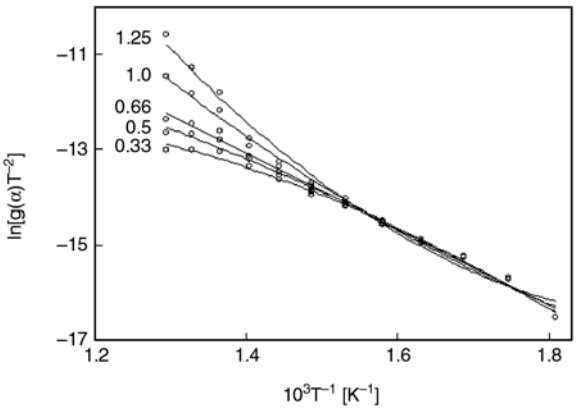

Figure 2. Dependence of $\ln[g(\alpha)/T^2]$ against $1/T$ for pure polypropene at different values of n

tion process obeys generally the sigmoidal or deceleration functions [2]. Pure polypropene decomposes without formation of solid residue (curve 1) while the other samples produce various amounts of solid residue of amorphous SiO_2 depending on the nature of the filler used (curves 2–5). Besides, the TG curves are shifted to different extents vs. that of the pure polypropene. For example, the TG-curve for polypropene filled with AR (curve 5) is shifted toward lower temperatures and the thermal degradation is complete at temperatures up to 440°C, obtaining solid residue of about 20 mass%. It may be concluded; therefore, that Aerosil as a filler of polypropene decreases its thermal stability most probably due to the monolayer distribution of PP on the filler and the presence of certain acidic centers on its surface [23]. The TG curve of polypropene filled with RRH (curve 2) is shifted towards lower temperature *vs.* that of the pure polypropene because the organic part of the raw rice husks started to decompose at temperature lower than that of pure polypropene [27]. The TG curve of polypropene filled with BRHA (curve 3) is practically the same as that for pure polypropene (curve 1). It was attributed to the carbon coating formed on the surface of the amorphous SiO_2, which makes it more compatible with the polymer matrix. For the characterization of polypropene composites thermal stability, two divergences among the studies are obvious: the first is the choice of kinetic models used to describe the pyrolysis kinetics, and the second is the calculation of the kinetic parameters obtained on the basis of the chosen model.

Using the calculation procedures of Coats and Redfern [34], all $g(\alpha)$ functions presented in Table 1 were first substituted into Equation (15) and the plot of the left side of this equation against $1/T$ was fitted by computer to calculate the correlation coefficient of linear regression R^2. This procedure was repeated until the best R^2 value was obtained. For the thermal degradation of the samples studied, single heating rate plots, $\ln[g(\alpha)/T^2]$ against $1/T$, were calculated according to Equation (15). It should be noted for all the samples studied that the highest values of R^2 were obtained when kinetic equations for the F_n mechanism (Table 1) with different values of n were used. In this respect, the kinetic curves of thermal degradation of pure polypropene with different values of n are presented in Figure 2 for illustration.

Figure 2 shows that the shapes of the kinetic curves strongly depend on the value of the parameter n. The same is true also for the other four-polypropene composites. To find the value of n with which the highest value of R^2 is obtained, the dependence $R^2 = f(n)$ was drawn. For comparison, the corresponding curves for pure polypropene (curve 1) and polypropene composite filled with 20 mass% Aerosil (curve 2) are presented in Figure 3.

The curves presented in Figure 3 can be described well with empiric polynomials of second order. Differentiating these polynomials vs. n and assuming their value to be zero, the value of n at which R^2 has maximum value could be calculated. For the first curve, the maximum of R^2 was obtained at $n = 0.66$,

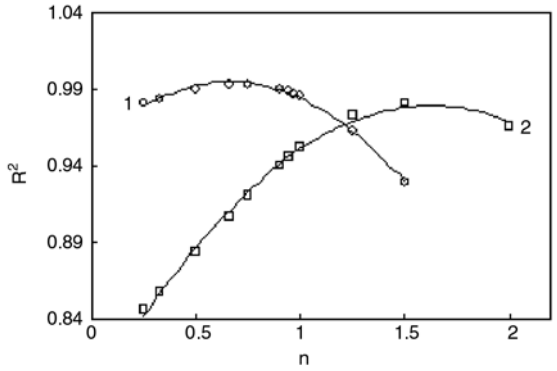

Figure 3. Dependence of the coefficient of linear regression R^2 on the values of n for thermal degradation of: pure polypropene – 1 and polypropene filled with 20 mass% Aerosil – 2

while for the second curve at $n = 1.63$. Similar procedure was used also to find the optimal value of n for the other composites. Subsequently, the apparent activation energy E and the pre-exponential factor A can be calculated from the slope and intercept of the fitted straight line. The same method was used to process the data from the TG curves of the composites studied, using the calculation procedures of Madhysudanan *et al.* [35], Tang *et al*. [36] and Wanjun *et al*.[37]. The results obtained are summarized in Table 4.

As can be seen from Table 4, the value of n varied from 0.66 to 1.63, depending on filler nature. The higher values were observed for the samples filled with WRHA or AR, which are pure SiO_2, by nature. The practically equal values of the kinetic parameters characterizing the thermal degradation of pure polypropene and polypropene filled with BRHA, as well as the same form of the kinetic equation ($n = 0.66$) confirmed the full compatibility of this filler with the matrix. In our opinion, the almost twice lower value of the activation energy of thermal destruction of the PP-BRHA sample compared to that of the PP-WRHA sample was due to the significant amount of porous carbon in BRHA. This porous carbon easily burns in oxidative medium (air) and facilitates the thermal degradation of the polypropene matrix. This is sustained by the lower activation energy of thermal destruction of PP-BRHA sample compared to pure polypropene, despite that the decomposition mechanism is the same ($n = 0.66$).

Since the values of E and A calculated using the four calculation procedures were quite close, they can be averaged. On this basis, the values of $\Delta S^{\neq}$, $\Delta H^{\neq}$ and $\Delta G^{\neq}$ were calculated at $T = T_p$, since this temperature characterizes the highest rate of the process, and therefore, is its important parameter. The change of Gibbs free energy $\Delta G^{\neq}$ reflects the total energy increase of the system at the approach of the reagents and the formation of the activated complex. This energy is influenced by two thermodynamic properties, the changes of enthalpy $\Delta H^{\neq}$

Table 4. Kinetic parameters of non-isothermal degradation of filled with different fillers (20 mass%) polypropene composites

Parameter	Sample				
	PP	**PP-RRH**	**PP-BRHA**	**PP-WRHA**	**PP-AR**
Coats – Redfern					
n	0.66	1.05	0.66	1.28	1.63
R^2	0.9976	0.9968	0.9973	0.9982	0.9978
E [kJ·mol^{-1}]	66.7	71.3	63.3	108.0	112.6
A [min^{-1}]	$1.26\cdot10^4$	$6.78\cdot10^4$	$7.99\cdot10^3$	$3.95\cdot10^7$	$7.20\cdot10^8$
Madhysudanan – Krishnan – Ninan					
E [kJ·mol^{-1}]	66.7	71.5	63.6	109.7	112.7
A [min^{-1}]	$1.5\cdot10^4$	$8.08\cdot10^4$	$9.81\cdot10^3$	$5.57\cdot10^7$	$8.28\cdot10^8$
Tang – Liu – Zang – Wang					
E [kJ·mol^{-1}]	66.8	71.9	63.7	109.2	112.8
A [min^{-1}]	$1.57\cdot10^4$	$8.41\cdot10^4$	$1.03\cdot10^4$	$5.69\cdot10^7$	$8.48\cdot10^8$
Wanjun – Yuwen – Hen – Zhiyong – Cunxin					
E [kJ·mol^{-1}]	66.7	71.3	63.3	108.0	112.56
A [min^{-1}]	$1.47\cdot10^4$	$6.81\cdot10^4$	$9.46\cdot10^3$	$4.35\cdot10^7$	$1.36\cdot10^8$
Average values					
E [kJ·mol^{-1}]	66.7	71.5	63.5	108.7	112.7
A [min^{-1}]	$1.45\cdot10^4$	$7.52\cdot10^4$	$9.39\cdot10^3$	$4.89\cdot10^7$	$6.33\cdot10^8$
$-\Delta S^{\neq}$ [J·mol^{-1}·K^{-1}]	214.9	200.9	218.4	147.3	125.1
$\Delta H^{\neq}$ [kJ·mol^{-1}]	60.7	65.8	57.6	102.8	107.4
$\Delta G^{\neq}$ [kJ·mol^{-1}]	216.1	205.0	212.2	207.8	187.2

and entropy $\Delta S^{\neq}$ of activated complex formation. The change of activation enthalpy shows the energy differences between the activated complex and the reagents. If this difference is small, the formation of activated complex is favored, because the potential energy barrier is low. The change of reaction entropy reflects how near the system is to its own thermodynamic equilibrium. Low activation entropy means that the material has just passed through some kind of physical or chemical aging process, bringing it to a state near its own thermodynamic equilibrium. In this situation, the material shows little reactivity, increasing the time taken to form the activated complex. On the other hand, when high activation entropy values are observed, the material is far from its own thermodynamic equilibrium. In this case, the reactivity is high and the system can react faster to produce the activated complex, which resulted in the short reaction times observed [38].

The thermal degradation of pure polypropene has been described as occurring by a random scission mechanism or two-third-order kinetics model when the number of chain scission is measured to estimate the change in the degree of polymerization. In the cases of filled composites, however, when random scission degradation is measured by weight loss, the kinetics will probably deviate from a two-third-order model. Since not every broken bond leads to evaporation of products, only product fragments which are small enough to evaporate will actually evaporate and thus lead to a decrease in the sample mass. For this reason, deviation of kinetics of random scission degradation from a two-third-order reaction model may be observed for filled composites. Another reason for which the kinetic of the thermal degradation of filled composites may differ from the two-third order kinetics model (n = 1.05) is that the degradation of PP in the samples filled with RRH was preceded by degradation of the organic component of the raw rice husks. For polypropene composites filled with WRHA or Aerosil, the kinetic model of decomposition is F_n, where n = 1.28 and 1.63 respectively. This can be explained with the high specific area of the fillers and the possibility for adsorption of the polypropene decomposition products on their surface. The comparison of R^2 values obtained according to the different calculation procedures used showed that the results obtained by Coats – Redfern best

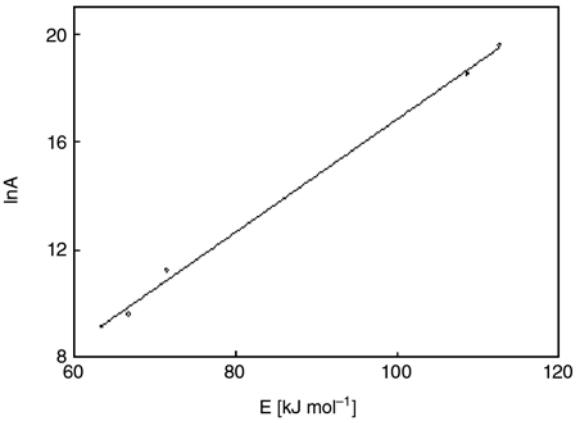

Figure 4. Compensation plot for the thermal decomposition of polypropene, filled with 20 mass% different fillers

describe the process of thermal decomposition reactions in pure and filled with different fillers polypropene.

On Figure 4 is presented the ccompensation plot for the thermal decomposition of polypropene, filled with 20 mass% different fillers.

As can be seen in Figure 4, there is a linear dependence between ln$A$ and E, which indicates for the existence of isokinetic relationship or kinetic compensation effect. It means that the most probable kinetic equations found describe correctly the mechanism of thermal destruction of the samples. The iso-kinetic rate constant k_{iso} was calculated to be equal to $1.61 \cdot 10^{-2}$ min^{-1} and the iso-kinetic temperature T_{iso} = 574.4 K. Above this temperature, the decomposition rate for the samples characterized by higher activation energy E becomes higher than that of the samples decomposing at lower activation energy. Besides, linear dependence was

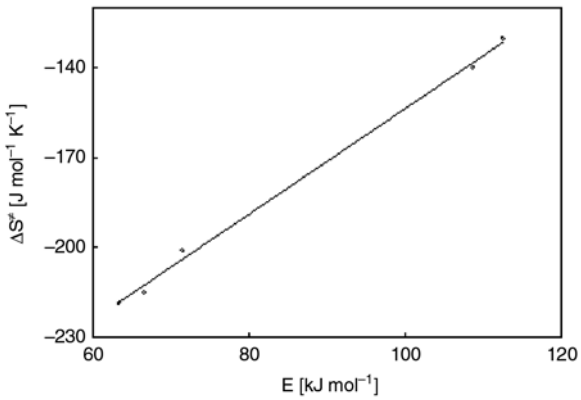

Figure 5. Plots of $\Delta S^{\neq}$ *vs.* E values for thermal decomposition of polypropene, filled with 20 mass% different fillers

observed also between the change of the entropy for the formation of the activated complex $\Delta S^{\neq}$ and the activation energy E of the samples studied (Figure 5).

Figure 5 shows that the increase of the value of E resulted in linear increase of the values of $\Delta S^{\neq}$, although remaining negative. It means that lower values of the entropy member correspond to higher values of the activation energy in the equation of Eyring, or the rearrangement of the initial structure of the composite during the formation of the activated complex was accompanied by smaller decrease of entropy. This effect was most evident for the samples filled with Aerosil and white rice husk ash, which are almost identical by chemical composition (pure SiO_2) and so exert the same effect on the thermal stability of the filled composite materials.

3.2. Mechanism of pyrolysis of polypropene

A variety of reactions are possible in the thermal degradation of polypropene. According to some authors [42–46], the degradation may be described by the following reactions:

Thermal degradation

$$P \rightarrow R_r^{\bullet} + R_{n-r}^{\bullet} \quad \text{(I)}$$

Hydrogen abstraction

$$P_n + R^{\bullet} \rightarrow B_n^{\bullet} + RH \quad \text{(II)}$$

Chain scission (β-scission)

$$B_n^{\bullet} \rightarrow R_r^{\bullet} + P_{n-r} \quad \text{(III)}$$

Chain end-radical transfer

$$P_n + R_r^{\bullet} \rightarrow P_r + B_n^{\bullet} \quad \text{(IV)}$$

Termination by combination with primary radical

$$R^{\bullet} + B_n^{\bullet} \rightarrow P_i$$

$$R^{\bullet} + R^{\bullet} \rightarrow P_i \quad \text{(V)}$$

Termination by disproportionation

$$R_r^{\bullet} + R_n^{\bullet} \rightarrow P_r + P_n \quad \text{(VI)}$$

This scheme showed that chain scission is not instantaneous. A practical consequence of this assumption is the formation of radicals with active center located along the backbone ($B^{\bullet}$) due to the abstraction of hydrogen. These radicals can undergo scission to generate polymer species with activity on the chain end ($P^{\bullet}$). It is also possible that combination between polymer radicals ($B^{\bullet}$ and $P^{\bullet}$) and the primary radicals ($R^{\bullet}$) occur, producing inactive polymer chains (P). The subscript i, n and r represent the chain lengths of the polymer species.

According to Simha-Wall model [32, 33], the mechanism of the thermal degradation of polypropene has been described as occurring by a random scission mechanism, in terms of first-order kinetics when the number of chain scissions is measured by the change in the degree of depolymerization. The main advantage of this model is the accurate description of the pyrolysis reaction in great detail. However, when random scission degradation is measured by weight loss, the kinetics will probably deviate from a first-order model [32, 46, 47]. By using apparatus such as TGA in kinetic studies, in fact the evaporation rate of products is determined and not the intrinsic chemical reaction rate, since not every broken bond leads to the evaporation of products but only product fragments which are small enough to evaporate will actually evaporate and thus lead to a decrease in the sample mass. Some authors proposed that zero-order kinetic model is appropriate at low degree of conversion ($0 < \alpha < 0.2$), but at higher degree of conversion ($0.7 < \alpha < 0.9$) the more correct approach is to use first-order kinetic equation. As a consequence, the kinetic constants differ significantly over the conversion range [46, 48]. According to Gao *et al.* [32, 33], it would be better to use fractional n-th order kinetic model to describe the pyrolysis kinetics of polypropene.

According to the random chain dissociation (RCD) model described in [46, 47], the pyrolysis process is a random process where each bond of the same type has an equal probability for cleavage, with a rate description according to a first order kinetic model (Figure 6).

Because of the differences in the stabilities of chains bonds caused by attached functional groups or radicals, a separate kinetic constant must be introduced for each type of bond. The model accounts for the fact that both physical and chemical processes play important roles during the pyrolysis of polymers. In this model, the mass of the polymer sample decreases due to evaporation of chains shorter than a certain 'evaporable' chain length. This parameter is a function of temperature and its value can be estimated from the boiling tem-

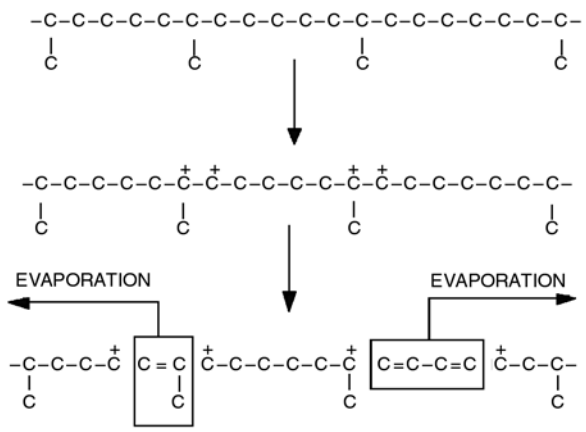

Figure 6. Schematic representation of pyrolysis process incorporated in the random chain dissociation (RCD) model

peratures of *n*-alkanes and *n*-alkenes. This approach implies that cleavage of the first bonds will not immediately result in evaporation of the degraded chains and, thus, this model predicts an initiation period with a comparatively low conversion rate. Following this initiation period, the conversion rate first increases until it reaches a maximum and then decreases due to a decrease of the available number of bonds. Due to the complex nature of this degradation mechanism of the polypropene, its kinetics is not possible to be described with zero, first or second order kinetics equations. By using apparatus as a TGA in kinetic studies, in fact the evaporation rate of products is determined and not the intrinsic chemical reaction rate, since not every broken bond in the polymer chain leads to the evaporation of products. Only product fragments which are small enough to evaporate will actually evaporate at given reaction temperature and thus lead to a decrease of the polymer mass [46]. This implies that both physical and chemical processes influence the measured rate of change of polymer mass and hence the observed pyrolysis kinetics. Incorporation of the influence of different types of chemical bonds and evaporation of the volatile products obtained through melted polypropene into the model complicate the establishing of the true kinetic mechanism of the pyrolysis process. Only computer simulations using different calculation procedures and kinetic equations (random nucleation, phase boundary reactions or diffusion) could possibly give the most probably kinetic parameters of the conversion process [2, 8, 49–51].

The thermal degradation of polypropene and polypropene composites begins in a melt with varying viscosity. Indeed, the presence of fillers increases significantly the viscosity of the molten polymer and filled polymer does not show Newtonian plateau at very low shear rate [52].

4. Conclusions

The thermal oxidative degradation kinetics of pure polypropene and polypropene filled with 20 mass% different fillers was analyzed using Coats – Redfern, Madhysudanan *et al.*, Tang *et al.*, Wanjun *et al.* calculation procedures and 27 model kinetic equations. The kinetic parameters E, A, $\Delta S^{\neq}$, $\Delta H^{\neq}$ and $\Delta G^{\neq}$ for all studied samples were calculated. The main results obtained in this article were summarized as follows.

(1) The results obtained on the basis of the four calculation procedures used were quite similar which implies that their average value could be taken.

(2) The kinetic of non-isothermal degradation of the samples studied was best described by kinetic equations of n-th order (F_n mechanism).

(3) Depending on the nature of the filler used, the values of n varied from 0.66 to 1.63.

(4) The highest values of n, E and A were observed for the composites filled with WRHA and Aerosil which have the same chemical composition (SiO_2) and porous structure.

(5) A linear dependence was found between ln$A$ and E of the samples studied, known also as kinetic compensation effect.

The results obtained were considered enough to conclude that the cheap raw rice husks (RRH) and the products of its thermal degradation (BRHA and WRHA), after vigorously grounding and mixing, cab successfully be used as fillers for polypropene to replace the expensive synthetic additive Aerosil in the preparation of different polypropene composites.

References

[1] Chen X., Yu B., Guo S.: Thermal oxidative degradation kinetics of PP and PP/$Mg(OH)_2$ flame-retarded composites. Journal of Applied Polymer Science, **103**, 1978–1984 (2007).

[2] Chen Y., Wang Q.: Thermal oxidative degradation kinetics of flame-retarded polypropylene with intumescent flame-retardant master batches in situ prepared in twin-screw extruder. Polymer Degradation and Stability, **92**, 280–291 (2007).

[3] Wang L., Sheng J.: A kinetic study on the thermal degradation of polypropylene/attapulgite nanocomposites. Journal of Macromolecular Science, Part B: Physics, **45**, 1–11 (2006).

[4] Zhang F., Zhang J., Wang Y.: Modeling study on the combustion of intumescent fire-retardant polypropylene. Express Polymer Letters, **1**, 157–165 (2007).

[5] Marcilla A., Gómez A., Reyes-Labarta J. A., Giner A., Hernandez F.: Kinetic study of polypropylene pyrolysis using ZSM-5 and an equilibrium fluid catalytic cracking catalyst. Journal of Analytical and Applied Pyrolysis, **68–69**, 467–480 (2003).

[6] Filho J. G. A. P., Graciliano E. C., Silva A. O. S., Souza M. J. B., Araujo A. S.: Thermo gravimetric kinetics of polypropylene degradation of ZSM-12 and ZSM-5 catalysts. Catalysis Today, **107–108**, 507–512 (2005).

[7] Kim S-W., Cho Y-S., Shim M-J.: Thermal degradation kinetics of PE by the Kissinger equation. Materials Chemistry and Physics, **52**, 94–97 (1998).

[8] Kim H. T., Oh S. C.: Kinetics of thermal degradation of waste polypropylene and high-density polyethylene. Journal of Industrial Engineering Chemistry, **11**, 648–656 (2005).

[9] Gersten J., Fanberg V., Hetsroni G., Shindler Y.: Kinetic study of the thermal decomposition of polypropylene, oil shale, and their mixture. Fuel, **79**, 1679–1686 (2000).

[10] Pehlivan H., Özmihçi F., Tihminlioglu T., Balköse D., Ülkü S.: Water and water wapor sorption studies in polypropylene-zeolite composites. Journal of Applied Polymer Science, **90**, 3069–3075 (2003).

[11] Ismail H., Mohamad Z., Bakar A. A.: A comparative study of processing, mechanical properties, thermo-oxidative aging, water adsorption and morphology of rice husk powder and silica fillers in polystyrene/styrene butadiene rubber blends. Polymer-Plastics Technology and Engineering, **42**, 81–103 (2003).

[12] Kaci M., Djidjelli H., Boukerrou A., Zaidi L.: Effect of wood filler treatment and EBAGMA compatibilizer on morphology and mechanical properties of low density polyethylene/olive husk flour composites. Express Polymer Letters, **1**, 467–473 (2007).

[13] Kim H. S., Yang H. S., Kim H. J., Park H. J.: Thermogravimetric analysis of rice husk flour filled thermoplastic polymer composites. Journal of Thermal Analysis and Calorymetry, **76**, 395–404 (2004).

[14] Razavi-Nouri M., Jafarzadeh-Dogouri F., Oromiehie A. R., Langroudi A. E.: Mechanical properties and water adsorption behaviour of chopped rice husk filled polypropylene composites. Iranian Polymer Journal, **15**, 757–766 (2006).

[15] Chaudhary D. S., Jollands M. C., Cser F.: Understanding rice hull ash as fillers in polymers: A review. Silicon Chemistry, **1**, 281–289 (2002).

[16] Panthapulakkal S., Law S., Sain M.: Enhancement of processability of rice husk filled high-density polyethylene composite profiles. Journal of Thermoplastics Composites Materials, **18**, 445–458 (2005).

[17] Ballice L., Reimert R.: Classification of volatile products from the temperature-programmed pyrolysis of polypropylene (PP), atactic-polypropylene (APP) and thermogravimetrically derived kinetics of pyrolysis. Chemical Engineering Processing, **41**, 289–296 (2002).

[18] Durmuş A., Koç S. N., Pozan G. S., Kaşgöz A.: Thermal-catalytic degradation kinetics of polypropylene over BEA, ZSM-5 and MOR zeolites. Applied Catalysis, Part B: Environmental, **61**, 316–322 (2005).

[19] Peterson D. J., Vyazovkin S., Wight C. A.: Kinetics of the thermal and thermo-oxidative degradation of polystirene, polyethylene and poly(propylene). Macromolecular Chemistry and Physics, **202**, 775–784 (2001).

[20] Song R., Jiang Z., Bi W., Cheng W., Lu J., Huang B., Tang T.: The combinated catalytic action on solid acids with nickel for the transformation of polypropylene into carbon nanotubes by pyrolysis. Chemistry-A European Journal, **13**, 3234–3240 (2007).

[21] Kruse T. M., Wong H-W., Broadbelt L. J.: Mechanistic modeling of polymer pyrolysis: polypropylene. Macromolecules, **6**, 9594–9607 (2003).

[22] Dawood A., Miura K.: Pyrolysis kinetics of γ-irradiated polypropylene. Polymer Degradation and Stability, **73**, 347–354 (2001).

[23] Carniti P., Gervasini A.: Thermogravimetric study of the kinetics of degradation of polypropylene with solid catalysts. Thermochimica Acta, **379**, 51–58 (2001).

[24] Tihminlioglu F., Pehlivan H., Balköse D., Ülkü S.: Effect of the zeolite filler on the thermal degradation kinetics of polypropylene. Oxidation Communications, **29**, 193–203 (2006).

[25] Marcilla A., Gomez A., Reyes-Labarta J. A., Giner A.: Catalytic pyrolysis of polypropylene using MCM-41: Kinetic model. Polymer Degradation and Stability, **80**, 233–240 (2003).

[26] Ramis X., Cadenato A., Salla J. M., Morancho J. M., Valles A., Contat L., Ribes A.: Thermal degradation of polypropylene/starch-based materials with enhanced biodegradability. Polymer Degradation and Stability, **86**, 483–491 (2004).

[27] Vlaev L. T., Markovska I. G., Lyubchev L. A.: Non-isothermal kinetics of pyrolysis of rice husk. Thermochimica Acta, **406**, 1–7 (2003).

[28] Albano C. L., Sciamanna E. S., Aquno T., Martinez J. J.: Metodology to evaluate thermogravimetric data using computational techniques in the polymer field. European Congress on Computational Methods in Applied Science and Engineering, ECCOMAS 2000, Barcelona, Spain 11–14 Sept., pp. 1–18 (2000).

[29] Roy P. K., Surekha P., Rajagopal C., Choudhary V.: Thermal degradation studies of LDPE containing cobalt stearate as pro-oxidant. Express Polymer Letters, **1**, 208–216 (2007).
[30] Vlaev L., Georgieva V., Genieva S.: Products and kinetics of non-isothermal decomposition of vanadium(IV) oxide compounds. Journal of Thermal Analysis and Calorymetry, **88**, 805–812 (2007).
[31] Šestak J., Berggren G.: Study of the kinetics of the mechanism of solid-state reactions at increasing temperatures. Thermochimica Acta, **3**, 1–12 (1971).
[32] Gao Z., Kaneko T., Amasaki I., Nakada M.: A kinetic study of thermal degradation of polypropylene. Polymer Degradation and Stability, **80**, 269–274 (2003).
[33] Gao Z., Amasaki I., Nakada M.: A thermogravimetric study on thermal degradation of polyethylene. Journal of Analytical and Applied Pyrolysis, **67**, 1–9 (2003).
[34] Coats W., Redfern J. P.: Kinetic parameters for thermogravimetric data. Nature, **201**, 68–69 (1964).
[35] Madhysudanan P. M., Krishnan K., Ninan K. N.: New equations for kinetic analysis of non-isothermal reactions. Thermochimica Acta, **221**, 13–21 (1993).
[36] Tang W., Liu Y., Zang H., Wang C.: New approximate formula for Arrhenius temperature integral. Thermochimica Acta, **408**, 39–43 (2003).
[37] Wanjun T., Yuwen L., Hen Z., Zhiyong W., Cunxin W.: New temperature integral approximate formula for non-isothermal kinetic analysis. Journal of Thermal Analysis and Calolimetry, **74**, 309–315 (2003).
[38] Ruvolo-Filho A., Curti P. S.: Chemical kinetic model and thermodynamic compensation effect of alkaline hydrolysis of waste poly(ethylene terepftalate) in non-aqueous ethylene glycol solution. Industrial Engineering Chemistry Research, **45**, 7985–7996 (2006).
[39] Nikolaev A. V., Logvinenko V. A., Gorbatchov V. M., Miachina L. I.: Thermal analysis. in 'Proceedings of the Fourth ICTA, Budapest Hungary' vol. 1, 47 (1974).
[40] Zmijewski T., Pysiak J.: Thermal analysis. in 'Proceedings of the Fourth ICTA, Budapest Hungary' vol. 1, 205 (1974).
[41] Vlaev L. T., Georgieva V. G., Genieva S. D.: Use of the ion polarization theory to interpret certain regularities of changes in characteristics and properties of inorganic compounds. Journal of Structural Chemistry, **47**, 813–822 (2006).
[42] Nakatani H., Suzuki S., Tanaka T., Terano M.: New kinetic aspects on the mechanism of thermal oxidative degradation of polypropylenes with various tacticities. Polymer, **46**, 12366–12371 (2005).
[43] Oliveira J. A., Biscaia E. C. Jr., Pinto J. C.: Analysis of kinetic models proposed for the controlled degradation of poly(propylene)-presentation of a general and analytical solution. Macromolecular Theory and Simulation, **12**, 696–704 (2003).
[44] Bockhorn H., Hornung A., Hornung U., Schawaller D.: Kinetic study on the thermal degradation of polypropylene and polyethylene. Journal of Analysis and Applied Pyrolysis, **48**, 93–109 (1999).
[45] Chan J. H., Balke S. T.: The thermal degradation kinetics of polypropylene: Part I. Molecular weight distribution. Polymer Degradation and Stability, **57**, 113–125 (1997).
[46] Westerhout R. M. J., Waanders J., Kuipers J. A. M., van Swaaij W. P. M.: Kinetics of the low-temperature pyrolysis of polyethene, polypropene, and polystyrene modeling, experimental, determination, and comparison with literature podels and data. Industrial and Engineering Chemistry Research, **36**, 1955–1964 (1997).
[47] Westerhout R. M. J., Balk R. H. P., Meijer R., Kuipers J. A. M., van Swaaij W. P. M.: Experimentation and evaluation of the use of screen heaters for the measurement of the high temperature pyrolysis kinetics of polyethene and polypropene. Industrial and Engineering Chemistry Research, **36**, 3360–3368 (1997).
[48] Qin H., Zhang S., Zhao C., Yang M.: Zero-order kinetics of the thermal degradation of polypropylene/clay nanocomposites. Journal of Polymer Science: Part B: Polymer Physics, **43**, 3713–3719 (2005).
[49] Contat-Rodrigo L., Ribes-Greus A., Díaz-Calleja R.: Characterization by thermal analysis of PP with enhanced biodegradability. Journal of Applied Polymer Science, **82**, 2174–2184 (2001).
[50] Chan J. H., Balke S. T.: The thermal degradation kinetics of polypropylene: Part II. Time-temperature superposition. Polymer Degradation and Stability, **57**, 127–134 (1997).
[51] Chan J. H., Balke S. T.: The thermal degradation kinetics of polypropylene: Part III. Thermogravimetric analyses. Polymer Degradation and Stability, **57**, 135–149 (1997).
[52] La Mantia F. P., Dintcheva N. T.: Thermomechanical degradation of filled polypropylene. Macromolecular Symposia, **194**, 277–286 (2003).